

UNIVERSITY OF WARSAW

DOCTORAL THESIS

Radiative Recombination in Strong Laser Pulses

Author:
Deeksha Kanti

Supervisor:
Dr. hab. Katarzyna Krajewska

*A thesis submitted in fulfillment of the requirements
for the degree of Physics*

in the

Institute of Theoretical Physics
Faculty of Physics

University of Warsaw

December 3, 2024

Declaration of Authorship

I, Deeksha Kanti, declare that this thesis titled, “Radiative Recombination in Strong Laser Pulses” and the work presented in it are my own. I confirm that:

- This work was done wholly or mainly while in candidature for a research degree at this University.
- Where any part of this thesis has previously been submitted for a degree or any other qualification at this University or any other institution, this has been clearly stated.
- Where I have consulted the published work of others, this is always clearly attributed.
- Where I have quoted from the work of others, the source is always given. With the exception of such quotations, this thesis is entirely my own work.
- I have acknowledged all main sources of help.
- Where the thesis is based on work done by myself jointly with others, I have made clear exactly what was done by others and what I have contributed myself.

Signed:

Date:

“Study hard what interests you the most in the most undisciplined, irreverent and original manner possible.”

Richard P. Feynman

“Dare to be free, dare to go as far as your thought leads, and dare to carry that out in your life.”

Swami Vivekananda

UNIVERSITY OF WARSAW

Abstract

Faculty of Physics

Doctoral Dissertation

Radiative Recombination in Strong Laser Pulses

by Deeksha Kanti

In this dissertation, we investigate laser-assisted radiative recombination (LARR) in strong laser pulses, an important phenomenon in strong-field physics. This process is crucial as it serves as a fundamental step of high-order harmonic generation, which ultimately led to the development of attosecond science.

In our study, we provide a comprehensive treatment of the LARR process, starting with an analysis of laser-assisted electron-atom radiative recombination. We consider an electron recombining with a hydrogen-like atom under the influence of a short-range atomic potential in the presence of a laser pulse, that results in the emission of high-energy photons. Additionally, we treat the laser pulse within the dipole approximation. Unlike previous formalisms, our comprehensive treatment of LARR eliminates the nonphysical oscillations in the energy spectrum of emitted photons. Moreover, we identify the laser-field-free recombination, which manifests as a peak in the energy spectrum of LARR. Together with parameters like the electron energy, the carrier-envelope phase of the pulse, and its shape, we also investigate the impact of a train of identical laser pulses on the LARR energy distribution. Our findings show that the energy distribution coherently enhances, varying in proportion to the square of the number of pulses in the train. Furthermore, we conduct a time-frequency analysis of the energy distribution of LARR, which allows for a laser-pulse diagnostics.

Under certain conditions, the dipole approximation may not be applicable. Therefore, the studies mentioned above serve as a foundation for exploring LARR beyond the dipole approximation. Additionally, we aim to investigate the impact of the Coulomb potential on the energy spectrum of LARR. Hence, we study the recombination of an electron to a hydrogen-like positive ion in the presence of the Coulomb potential and the laser field; the latter varying in space and time. To account for the nondipole corrections in the leading order in $1/c$, we perform a relativistic reduction of the Klein-Gordon equation for the scattering state of the electron. Our studies reveal that nondipole corrections that are arising are of three different origins: gauge transformation correction, retardation, and recoil correction. We observe nondipole effects manifesting as an extension of the plateau and an asymmetry in the energy-angle distribution of LARR, primarily attributed to the recoil effect. In addition, we demonstrate a method to enhance the intensity of specific harmonics on the edges of the LARR plateau by chirping the assisting laser pulse. We conclude our investigation by demonstrating the nodal and vortex structures in the LARR probability amplitude.

UNIwersytet Warszawski

Streszczenie

Wydział Fizyki

Rozprawa Doktorska

Rekombinacja Radiacyjna w Silnych Impulsach Laserowych

Deeksha Kanti

Rozprawa doktorska poświęcona jest rekombinacji radiacyjnej w asyście impulsów laserowych (LARR), które to zjawisko odgrywa znaczącą rolę w fizyce silnych pól laserowych. Proces ten jest kluczowy, gdyż stanowi podstawowy krok w generowaniu harmonicznych wyższego rzędu, co doprowadziło na przestrzeni ostatnich lat do rozwoju fizyki attosekundowej.

W rozprawie przedstawiono kompleksowe omówienie procesu LARR, zaczynając od analizy wspomaganej laserowo rekombinacji radiacyjnej elektron-atom. Rozważono rekombinację elektronu z atomem wodoropodobnym pod wpływem krótko-zasięgowego potencjału atomowego oraz w obecności impulsu laserowego, co skutkuje emisją fotonów o wysokiej energii. Ponadto, potraktowano impuls laserowy w przybliżeniu dipolowym. W przeciwieństwie do poprzednich sformułowań teoretycznych, przedstawione w rozprawie podejście eliminuje niefizyczne oscylacje w widmie energetycznym emitowanych fotonów. Identyfikuje również rekombinację bez pola laserowego, która objawia się jako pik w rozkładzie energetycznym promieniowania. Wraz z parametrami takimi jak energia elektronu, faza obwiedni impulsu laserowego czy jego kształt, zbadaliśmy ponadto wpływ ciągu identycznych impulsów laserowych na rozkład energii promieniowania. Nasze badania pokazały, że rozkład ten spójnie się wzmacnia, zmieniając się proporcjonalnie do kwadratu liczby impulsów w ciągu. Ponadto, przeprowadziliśmy analizę czasowo-częstotliwościową rozkładu energii LARR, co umożliwiło z kolei diagnostykę impulsów laserowych.

W pewnych warunkach przybliżenie dipolowe nie jest spełnione. Dlatego wymienione powyżej wyniki stanowiły wstęp do badań nad procesem LARR poza przybliżeniem dipolowym. Naszym celem było też zbadanie wpływu potencjału kulombowskiego na widmo energetyczne LARR. W związku z powyższym zbadano rekombinację elektronu do dodatniego jonu wodoropodobnego w obecności potencjału kulombowskiego i pola laserowego, gdzie to ostatnie zmieniało się w przestrzeni i w czasie. Aby uwzględnić poprawki pozadipolowe w wiodącym rzędzie $1/c$, przeprowadzono relatywistyczną redukcję równania Kleina-Gordona dla stanu rozproszeniowego elektronu. Nasza analiza pokazała, że poprawki pozadipolowe mogą wywodzić się z transformacji cechowania, opóźnienia bądź z odrzutu. Zaobserwowano efekty pozadipolowe manifestujące się jako poszerzenie zakresu plateau w widmie energetycznym promieniowania LARR i asymetria w rozkładach kąto-energetycznych generowanego promieniowania, przypisywane przede wszystkim efektowi odrzutu elektronu oddziałującego z polem laserowym. Pokazano też zwiększenie intensywności określonych harmonicznych na brzegach plateau LARR spowodowane obecnością impulsów ze świergotem. Na zakończenie zademonstrowano struktury węzłowe i wirowe w amplitudzie prawdopodobieństwa LARR.

Acknowledgements

First, I want to express my gratitude to my parents, Sarveshwari Sati Kanti and GhanaNand Kanti, for recognizing the value of education when I was ignorant of it. Like many others, my mother was my first teacher. Every small achievement I have made is due to her unwavering dedication and perseverance towards my education and well-being. I am also deeply grateful to my father for instilling in me the importance of science and for providing the comfort and support that empowered me to pursue my dreams, ultimately leading me to pursuing a PhD in Physics.

I want to express my heartfelt gratitude to my supervisor, Prof. Katarzyna Krajewska, for providing me with an invaluable opportunity to pursue PhD under her supervision at the Faculty of Physics, University of Warsaw. Her guidance, support, and belief in me have been crucial throughout this journey. I want to thank her for sharing her time and expertise with me during my PhD. I learned critical skills like tackling problems from a theoretical standpoint and recognizing the significance of every notation in theory. One piece of advice that profoundly impacted my perspective came from her: "Deeksha, every single notation has some meaning." This insight changed the way I view mathematical equations. Whenever I felt nervous or doubted my writing, Prof. Krajewska encouraged me to give my best and reassured me of my writing abilities, boosting my confidence. She was always open to discussions, no matter how trivial my questions seemed, which fostered my curiosity. She made sure that I understood the thing.

I sincerely thank Prof. Jerzy Kamiński for his invaluable experience, insights, and assistance throughout my PhD journey. His discussions and support were immensely helpful whenever I needed guidance. His passion for the pursuit of physics at this stage in his career inspires many young researchers and I am one of them.

I would like to acknowledge the help of research group members Felipe, Mateusz, Mihai, and Julia for their kind help with the bureaucracy of the department during my PhD studies. I would like to acknowledge Mateusz Majczak for lasting conferences with me, and it would be fair to say that sometimes our discussions were more insightful. I also want to thank my office mate, Mateusz Homenda, for creating a positive and uplifting environment in the office.

I want to express my gratitude to the friends I made during my five years in Poland for my PhD. My two friends, Asia and Agnieszka, whom I met in the most unexpected place while getting our COVID vaccinations. They are my go-to people whenever I need help with the Polish language, especially when it comes to medical issues. I also want to extend my heartfelt thanks to them and their families for welcoming me into their celebrations and vacations and helping me feel at home in a foreign country. I would like to acknowledge the friends I met in Warsaw: my Indian friends Sanjukta, Bohnishika, Mohnish, Jowita, Iswarya, Priyanka, Arun, Alina, Arka, Sudeep, and Kaustav; my Tunisian friend Rania; and my Iranian friends Saed and Melica, along with their cats. I appreciate their care, love, and affection. I am grateful for their life advice, even though they sometimes struggle to follow it themselves. My special thanks to my dear friends, Sanjukta and Mohnish, for their constant support, time filled with laughter and encouragement. I truly enjoy our discussions from science, civilization, politics, spirituality, yoga, art, music, and culture. Spending time with all my friends made me feel at home during my PhD journey.

I would like to take a moment to acknowledge two wonderful individuals: my brother, Dhruv Kanti, and Leon Beise. They consistently encourage and uplift me, always seeing the

best in me. Their love, care, and support have made my journey through my PhD both meaningful and fulfilling. I also want to extend my heartfelt gratitude to Leon's family for being the kindest and most loving family.

I would also like to acknowledge my theatre school, "Warsztaty Teatralne," where I had the pleasure of meeting wonderful people. We participated in several rehearsals and performed in front of a live audience, and I learned so much about life. I realized how important it is to have a hobby during the lengthy process of pursuing a PhD. I always returned to my research with renewed energy and enthusiasm.

I would like to express my gratitude to my relatives, especially Mr. Rakesh Kanti and Mrs. Renu Kanti, who consistently check in on my well-being, both in terms of health and finances. I also want to acknowledge Mr. Mohan Prasad Nainwal and Mrs. Sangeeta Diyundi Nainwal, who graciously hosted me and helped me to begin my journey in Physics. I am grateful to my grandparents for their forever blessings. I want to acknowledge my Uncle Mr. Prakash Kanti. After being shot and paralyzed from the waist down during a protest in 1994, his strong mental resilience and pursuit of education inspired and motivated me, especially in my PhD journey. Lastly, I want to thank my childhood friends, Anju and Sheetal, back in India, who made an effort to stay in touch despite my unavailability for their weddings without any complaints.

I would like to express my gratitude to all the individuals who have been part of my learning journey. I may unintentionally overlook some names, but I want to acknowledge everyone. Additionally, I would like to extend my special thanks to my master's supervisor, Dr. Hari Varma, for guiding me during my master's program and encouraging me to pursue a PhD, which ultimately led me to my PhD supervisor.

Finally, I acknowledge and I am grateful for the financial support from the National Science Centre, Poland, under Grant No. 2018/30/Q/ST2/00236. Their support allowed me to focus comfortably on my work during my five years of PhD studies.

Contents

| | |
|--|------------|
| Declaration of Authorship | iii |
| Abstract | vii |
| Streszczenie | ix |
| Acknowledgements | xi |
| 1 Introduction | 1 |
| 2 Laser-Assisted Radiative Attachment (LARA) | 7 |
| 2.1 Introduction | 7 |
| 2.2 Theoretical formulation of LARA | 8 |
| 2.2.1 LARA by an impact of a monoenergetic electron wave | 8 |
| 2.2.2 LARA by an impact of an electron wave packet | 13 |
| 2.2.3 Simplified formulation of LARA | 15 |
| 2.2.4 Electron wave packet model | 16 |
| 2.2.5 Laser field model | 18 |
| 2.3 Numerical illustrations | 19 |
| 2.3.1 Energy distributions of LARA radiation | 19 |
| 2.3.2 Frequency combs | 25 |
| 2.3.3 Energy distribution spectrograms | 29 |
| 2.3.4 LARA-based laser field metrology | 31 |
| 2.4 Summary | 32 |
| 3 Laser-Assisted Radiative Recombination (LARR) | 35 |
| 3.1 Introduction | 35 |
| 3.2 Theoretical formulation of LARR | 36 |
| 3.2.1 Coulomb-Volkov scattering state with nondipole corrections | 36 |
| 3.2.2 LARR by an impact of a monoenergetic electron wave | 41 |
| 3.2.3 LARR by an impact of an electron wave packet | 47 |
| 3.2.4 Energy distributions of LARR radiation | 47 |
| 3.3 Numerical illustrations | 48 |
| 3.3.1 Nondipole effects in LARR | 48 |
| 3.3.2 LARR in chirped laser pulses | 55 |
| 3.3.3 Vortex structures | 59 |
| 3.4 Summary | 65 |
| 4 Conclusions | 67 |

| | | |
|----------|--|-----------|
| A | Supplementary materials for Chapter 2 | 69 |
| A.1 | Alternative derivation of $\langle \delta(Q) \rangle$ and $\langle \mathcal{P}(\frac{1}{Q}) \rangle$ | 69 |
| A.2 | Spectrogram | 70 |
| A.2.1 | Definition, properties, and method of calculating the spectrogram | 70 |
| A.2.2 | Numerical examples and their analysis | 75 |
| | | |
| B | Supplementary materials for Chapter 3 | 81 |
| B.1 | Gauge transformation | 81 |
| B.2 | Nordsieck integral | 81 |
| B.3 | Details of calculations using the Nordsieck integral | 83 |
| B.4 | Classical consideration | 89 |
| B.5 | Mathematical model of vortices | 90 |

Dedicated to kindness, love and knowledge

Chapter 1

Introduction

In 2023, the strong-field physics [1,2] received well-deserved recognition as the Nobel Prize in Physics was awarded to Pierre Agostini, Ferenc Krausz, and Anne L’Huillier [3]. They were awarded for their pioneering work in developing experimental methods to generate attosecond pulses, which have become invaluable tools for probing the dynamics of electrons within matter [4,5,6,7,8,9,10,11,12,13,14,15]. Their applications span diverse fields, encompassing nonlinear optics, atomic and molecular physics and nanotechnology (for recent reviews, see Refs. [16,17,18,19]). Within this thesis, we aim at theoretical understanding of the fascinating strong field phenomena, with a particular focus on Laser-Assisted Radiative Recombination (LARR) in the presence of short laser pulses. This focus is essential because LARR represents the third and final step of High-Order Harmonic Generation (HHG) [4,20,21]. This process possesses the capability to generate coherent bursts of light with attosecond duration [22,23,24], opening up an entirely new discipline of scientific inquiry. In HHG [20,21], the intense laser field ionises the atomic target, and when the oscillating field brings back the ionised electron to the parent ion or atom, recombination occurs, followed by the emission of high harmonic photons, often in the extreme ultraviolet (XUV) or soft X-ray range. Hence, investigating LARR is of great importance as it enables us to exert control over the properties of the emitted HHG spectrum, contributing to a deeper understanding of ultrafast physics.

It is worth noting that although LARR represents the final step in the HHG process, there is a fundamental difference between LARR and HHG. In LARR, the initial electron momentum can be arbitrary whereas in HHG it is well defined by the first two steps of HHG mechanism. Also, it is worth stressing that while LARR is a laser-assisted process, the HHG is a laser-induced process which cannot occur in the absence of a laser field.

As highlighted above, this thesis shines a spotlight on the phenomenon of radiative recombination in the presence of an external laser field. However, radiative recombination can occur independent of an external laser field. In this process an electron recombines with an atomic target, resulting in the emission of a high-energy photon. It occurs naturally in various environments such as plasmas, astrophysical conditions, or even in laboratory settings without the presence of a laser field [25,26,27]. In this scenario, as determined by the energy conservation condition, the photon’s energy is an excess of energy necessary to bind an initial electron in a target. However, in the presence of an external laser field, the energy spectrum of emitted photons undergoes significant complexity due to the recombination process potentially incorporating both the absorption and emission of laser photons. This results in a wide-ranging spectrum of LARR radiation.

In the early stages of researching LARR processes, the external laser field was assumed to be weak. Within this setup, the laser was tuned to precisely match the transition energy between the electron’s scattering state and its recombined bound state. The process resulted in the emission of a single photon with a well-defined energy. These experiments were carried out in ion

storage rings and played a crucial role in investigating the electron cooling process and enhancing the production rate of antihydrogen [28]. The merged beam configuration, involving laser photons, electrons, and protons within an ion storage ring, provides a favorable setting for Laser-Induced Recombination (LIR) and LARR [29, 30]. It has been observed that the presence of the laser field not only amplifies the recombination process but also facilitates the generation of a recombined system in a well defined final state [29]. Furthermore, this setup helps to investigate the photorecombination spectrum of LARR/LIR with high resolution, thanks to the narrow bandwidth of the laser. In the early 2000, there were investigations aimed at directly observing LARR [31]. The experiment involved Kr^+ ions in either the ground state or metastable state, subject to a laser field at various intensities. The choice of the target is important such that it should be easily ionised at intensities lower than the ionisation threshold of the ground state. Once the stable product is formed via recombination, it becomes challenging to ionise again at those intensities. In this scenario, direct recombination can be observed using particle detection. Another experiment on LARR was conducted in the presence of a microwave field [32], where the authors demonstrated that the Coulomb potential plays a significant role at low kinetic energy of electron and in a weak to moderate laser field. The experiment was in agreement with Monte Carlo simulations when both the Coulomb potential and laser field were taken into account. The experimental investigation in Ref. [33] focused on the impact of laser field polarisation in LARR or LIR. The observation shows different behaviors in the average differential cross-section of recombination, for parallel and perpendicular polarisations of the laser field with respect to the field propagation. This underscores the significant influence of an external laser field on laser-assisted processes. However, these experiments served as a catalyst for a deeper scientific inquiry. They piqued interest in the generation of high-energy photons, leading to further investigation of radiative recombination in the presence of strong external fields.

Being one of the most important laser-assisted processes, LARR has become an intriguing subject of exploration for physicists in recent years [34, 35, 36, 37, 38, 39, 40, 41, 42, 43, 44, 45]. The plateau of the LARR energy spectrum is a crucial feature for extracting information about the LARR process [35, 39]. It is possible to achieve this through classical considerations of LARR using Bohr's correspondence principle. In particular, the width of the energy spectrum and the probability distribution of the emitted photon are in good agreement with the quantum considerations of LARR [35]. Additionally, in Ref. [39], the authors investigated the origin of the LARR and HHG plateaus. Specifically, it was concluded that the LARR plateau reflects the probability density of the electron in the laser field, whereas, in the case of the HHG spectrum, it reflects the probability density of the electron near the parent ion or nucleus after Above Threshold ionisation (ATI). LARR has also been explored as means to develop a coherent energy source and to gain insights into electron-ion interactions. Substantial work has been conducted in this direction. For instance, in the Ref. [37], the authors conducted an investigation into electron-ion scattering that occurs before eventual recombination in the presence of a laser field. This study aimed to understand how this process impacts the energy spectrum of emitted photons, particularly when compared to direct LARR. Additionally, it aimed to provide further insights into related processes such as HHG. Another method to manipulate the LARR process is by introducing a plasma medium. This approach enables researchers to model a more realistic scenario and gain insights into the behavior of plasma under extreme fields. In Ref. [38], the authors not only investigated LARR and its advantages over laser-field-free recombination but also examined the impact of plasma on LARR. The calculations reveal that the shape of the emitted LARR spectrum undergoes significant modification and enhancement

when the velocity of quiver electrons approaches or exceeds that of plasma electrons. There is also a significant enhancement in the LARR plateau, particularly towards the high energies of the emitted photons when the electron combines with the atom resonantly [42]. The increase in the plateau is by almost two orders of magnitude, and the spectra closely match with HHG spectra of the system. The electron first gains energy in the laser field and subsequently recombines with the atom either resonantly or nonresonantly. During the resonant recombination, the electron also undergoes spontaneous emission, incorporating energy gained both through absorption and stimulated emission due to the laser field.

Note that Refs. [34, 35, 37, 38, 39, 41, 42] investigated LARR in the presence of monochromatic plane waves. The study in Ref. [41], reveals that the angular distribution of emitted photons depends on the field strength, while the polarisation of emitted photons is determined by the geometry between the polarisation of the laser field and the direction of electron momentum. Also, the impact of field strength on the intensity and energy distribution of emitted photons was explored in Ref. [34]. However, besides controlling the enhancement of the LARR spectrum with the help of a monochromatic laser field, it is also possible to manipulate the characteristics of the emitted LARR spectra using multicolor laser fields [36, 40, 43, 44, 45]. For instance, by adjusting the relative phase parameter between different color fields [36, 40], one can shift the position of maxima in the energy spectrum and alter its shape. The relative phase of the two selected frequency fields also enables control over the polar distribution of the differential energy spectrum. In HHG, the bicircular laser field allows for the generation of circularly polarised radiation, which enables the investigation of the chirality of a molecule. Therefore, LARR being the third step of the HHG process, was also studied using bichromatic circularly [43, 45] and elliptically [44] polarised light. It was observed that the ellipticity of the laser field can also alter the cut-off energy of the plateau in the energy spectrum, providing further insights into the HHG process.

The most widely used analytical method for studying LARR is the inverse Keldysh-Faisal-Reiss model, often referred to as the Strong Field Approximation (SFA) [46, 47, 48]. In this approximation, the incident electron interacts exclusively with the external laser field; thus, the effect of the atomic potential on the initial electron scattering state is neglected. In addition, the electron's final bound state is free from the influence of the laser field. It is worth noting that the SFA has been extended to include the effect of the long-range Coulomb potential on the electron's scattering state [49]. This extension reveals some influence of Coulomb effects on the emitted photon spectrum, even when dealing with electrons at higher kinetic energies. Including Coulomb effects results in a decrease in the intensity of LARR distribution. As the kinetic energy of electrons increases, the Coulomb effect on LARR distribution diminishes, although it remains noticeable up to 1 keV. Additionally, some researchers choose to incorporate the effect of the laser on the bound state of the electron. In this case, enhancements in the energy distribution of emitted photons become apparent, particularly at higher laser field intensities [50]. Other than SFA, there are alternative approaches for investigating LARR. One such method is the Feynman path integral approach, as detailed in Ref. [51]. In this approach, the transition amplitude is expanded in the leading order in the atomic potential. The zeroth-order approximation is equivalent to the LARR transition amplitude calculated using SFA. The first and second order terms correspond to scattering followed by recombination in the presence of a laser field. Also, an analytical expression for the cross-section of LARR for hydrogen-like atoms is formulated in Ref [52]. It represents the transition amplitude using Bessel functions, as a summation of an infinite series over laser field harmonics. Subsequently, by applying the Plancherel theorem, the authors further solve the summation, obtaining a closed expression for

the recombination cross-section in the presence of a laser field. In Ref. [53], the authors used effective range theory [54] to study the LARR cross-section for the Xe^+ ion and realized that the interference pattern is sensitive to the form of the atomic potential.

In this thesis, our focus is on investigating LARR in the presence of short laser pulses. The choice of short laser pulses is of particular interest due to their capacity to introduce an additional dimension for controlling and enhancing the LARR energy spectrum. This control is possible by manipulating parameters such as the number of cycles in a pulse, the carrier envelope phase (CEP), the peak intensity, or the duration of the pulse [55, 56, 57, 58, 59, 60, 61]. Although research has been conducted on this topic, our theory distinguishes itself by effectively eliminating the issue of unphysical oscillations or occurrence of secondary plateau structures in the energy spectrum of LARR, recognized as the Gibbs effect [62, 63].

Furthermore, the qualitative behavior of the energy spectrum, including features like maxima and minima, can be interpreted to some extent through classical or semiclassical treatments. However, these methods fall short in illustrating the oscillations in the energy spectrum of LARR. To observe these oscillations, one must delve into a quantum mechanical description of LARR. The reason being that the oscillations arise from the quantum interference of the transition amplitude at different times corresponding to the specific energy of the emitted photon [34, 37, 39, 43, 44]. Note that in these references, the transition amplitude of LARR is calculated using the saddle point approximation. In our theoretical formulation of LARR, however, it is calculated exactly. In our case, the saddle-point approximation serves only as a tool to interpret our numerical results, for instance, the range of the spectrum and the oscillations within it, as discussed in the following chapters.

In Chapter 2, we revisit LARR in the presence of a short laser pulse within dipole approximation. Since it involves electron-atom recombination in the presence of a laser pulse, we refer to it as Laser-Assisted Radiative Attachment (LARA). From our perspective, this Chapter represents an enhancement of the existing LARR theories, as it allows us to pinpoint the contributions from both laser-field-free and laser-field-modified recombination processes in the energy spectrum of LARA. Unlike previously developed theories of LARA [56, 57, 58, 59, 60, 61], our theory approaches the LARA process differently. This approach aims to prevent the Gibbs effect [62, 63] in the energy spectrum of LARA, which arise from forcibly limiting the time integral in the transition amplitude to the duration of the pulse. Our analysis encompasses both the isolated pulse and the pulse train. As an outcome, the respective probability distributions of LARA photons will be coherently enhanced for the train of pulses as compared to the results for a single pulse. Furthermore, we have also investigated their respective spectrograms, as presented in detail in Chapter 2.

In Chapter 3, we investigate the LARR beyond the dipole approximation. We start with the Klein-Gordon equation and solve it for the scattering wave function of an electron up to a leading order in $1/c$, in the presence of both the Coulomb potential and the laser field. This leads to the emergence of nondipole corrections of three different origins. When nondipole effects are taken into account, we observe an extension in the range of the LARR plateau and asymmetry in the energy-angle distribution of emitted photons. Our numerical analysis of the energy distribution of LARR demonstrates that the recoil effect is the most prominent one. Note that Ref. [64] studied LARR beyond the dipole approximation as well, however in a purely relativistic framework. In contrast to Chapter 3, it assumed a plane wave laser field and neglected the Coulomb effect on the electron scattering state. It resulted in the emission of gamma rays and found a shift in angular distributions of emitted photons. Still in Chapter 3, we demonstrate a way to increase the intensity of LARR radiation with the help of chirped laser pulses.

We conclude that the flatter pulse leads to an increased yield of emitted photon yield. The results of our theoretical investigation are put forward in detail in Chapter 3. At the end, we demonstrate vortex structures that occur in the LARR probability amplitude.

In the thesis, we use the atomic units (a.u.) of the momentum $p_0 = \alpha m_e c$, energy $E_0 = \alpha^2 m_e c^2$, length $a_0 = \hbar/p_0$, time $t_0 = \hbar/E_0$, electric field strength $\mathcal{E}_0 = \alpha^3 m_e^2 c^3 / (|e|\hbar)$, and the laser field intensity $I_0 = \epsilon_0 c \mathcal{E}_0^2 \approx 7.02 \times 10^{16} \text{ W/cm}^2$, where m_e and $e = -|e|$ are the electron rest mass and charge, α is the fine-structure constant, and $\epsilon_0 = e^2 / (4\pi\alpha\hbar c)$ is the vacuum permittivity. In analytical formulas, on the other hand, we put $\hbar = 1$ while keeping the remaining fundamental constants explicitly.

This thesis is built upon the publications:

- *Laser-assisted electron-atom radiative recombination in short laser pulses*, D. Kanti, J. Z. Kamiński, Liang-You Peng, and K. Krajewska, Phys. Rev. A **104**, 033112 (2021),
- *Laser-assisted radiative recombination beyond the dipole approximation*, D. Kanti, M. M. Majczak, J. Z. Kamiński, Liang-You Peng, and K. Krajewska, Phys. Rev. A **110**, 043112 (2024),

which have also been presented at the following conferences and workshops:

- *Laser-Assisted Electron-Atom Radiative Recombination in Short Laser Pulses* (Talk), D. Kanti, J. Z. Kamiński, Liang-You Peng, and K. Krajewska, The 29th annual International Laser Physics Workshop (LPHYS'21), 19-23 July, 2021,
- *Laser-assisted electron-atom radiative recombination in short laser pulses* (Poster), D. Kanti, J. Z. Kamiński, Liang-You Peng, and K. Krajewska, Quantum Optics X conference, Toruń (Poland), 5-11 September, 2021,
- *Laser-assisted radiative recombination in short laser pulses* (Talk), D. Kanti, J. Z. Kamiński, Liang-You Peng, and K. Krajewska, DAMCOS-2, IIT Mandi, India, 21-22 June, 2022,
- *Laser-assisted radiative recombination (LARR)* (Talk), D. Kanti, J. Z. Kamiński, Liang-You Peng, and K. Krajewska, DAMCOS-3, IIT Mandi, India, 9-10 May, 2023,
- *Nondipole effects in laser-assisted radiative recombination by ultrashort laser pulses* (Poster), D. Kanti, M. M. Majczak, J. Z. Kamiński, Liang-You Peng, and K. Krajewska, Attochem Tenerife, Univ. La Laguna, Tenerife, Canary Islands, 28 Feb-1 March, 2024,
- *Laser-Assisted radiative recombination (LARR) in short laser pulses* (Talk), D. Kanti, M. M. Majczak, J. Z. Kamiński, Liang-You Peng, and K. Krajewska, Workshop: Atoms in strong laser fields, OsloMet Quantum Hub, Oslo, Norway, 10-12 June, 2024,
- *Nondipole effects in laser-assisted radiative recombination by ultrashort laser pulses* (Poster), D. Kanti, M. M. Majczak, J. Z. Kamiński, Liang-You Peng, and K. Krajewska, ECLIM 2024 - 37th European Conference on Laser Interaction with Matter, Lisbon, Portugal, 16-20 September, 2024.

The thesis was completed within the project financed by the National Science Centre (Poland) under Grant No. 2018/30/Q/ST2/00236.

Chapter 2

Laser-Assisted Radiative Attachment (LARA)

2.1 Introduction

This Chapter is devoted to electron-atom recombination accompanied by a laser field which is also referred to as Laser-Assisted Radiative Attachment (LARA). More specifically, we study the attachment of an electron to a hydrogen-like atom that occurs in the presence of short laser pulses. In such case, it is legitimate to stay in the framework of SFA. As for other quantum processes, the probability amplitude of LARA is represented as a time integral. In contrast, however, to previously formed theory of recombination [56, 57, 58, 59, 60, 61], we do not truncate the time integral to the duration of the laser pulse. In this case, the emergence of an important contribution is on display, i.e., the contribution from the laser-field-free process. Most importantly, our theory prevents the appearance of unphysical oscillations in the energy spectrum of LARA; which is known as the Gibbs effect [62, 63]. Since our approach accounts for an arbitrary laser field, we display the results for isolated pulses and pulse trains. As we show, there is a mark of coherent enhancement of the LARA spectra for the latter. More precisely, the comb-like structures in the spectra occur for the number of identical pulses, with a yield that scales quadratically with the number of pulses in a train. Another element of our studies is associated with the time-frequency analysis of LARA spectra, which turns out to be valuable for a temporal reconstruction of the laser field.

This Chapter is structured as follows. In Section 2.2, we develop the theoretical background of laser-assisted radiative attachment. We consider LARA by the impact of a monochromatic electron wave (Section 2.2.1), which leads to a singularity in the probability amplitude. To deal with it, in Section 2.2.2, we consider an electron wave packet instead of a monochromatic electron wave. For comparison, in Section 2.2.3, there are simplified formulas for the bandwidth-limited probability amplitude similar to Refs. [56, 57, 58, 59, 60, 61]. It provides a way to compare the previous theory with our comprehensive treatment of LARA. The illustration of the electron wave packet model and the laser field model used in this Chapter are in Sections 2.2.4 and 2.2.5, respectively. The energy distributions of LARA radiation and comparison between our comprehensive approach and the simplified one are shown in Section 2.3.1. The results presented in Section 2.3.1 are for isolated laser pulses, yet we demonstrate the LARA energy spectra for pulse trains in Section 2.3.2. Consequently, in Section 2.3.3, we conduct the time-frequency analysis of our numerical results. The proposition to use such analyses as a tool to retrieve the complete characteristics of the laser field is set in Section 2.3.4. We recapitulate our results and give possibilities for further research in Section 2.4.

2.2 Theoretical formulation of LARA

2.2.1 LARA by an impact of a monoenergetic electron wave

Consider the recombination of an electron by a short-range atomic potential $V(\hat{\mathbf{r}})$ in the presence of a laser field with the emission of a photon. We assume that the latter carries the energy $\omega_{\mathbf{K}}$, the wave vector \mathbf{K} , and polarisation $\boldsymbol{\varepsilon}_{\mathbf{K}}$. In this Chapter, the laser field is described as a time-dependent electric field $\boldsymbol{\mathcal{E}}(t)$; meaning that we use the dipole approximation. For this approximation to be valid, one has to neglect the spatial dependence and so the magnetic field component of the laser field, which is a typical situation encountered in strong-field physics.

The Hamiltonian written in the length gauge describing the process takes the form

$$\hat{H}(\hat{\mathbf{r}}, t) = \hat{H}_0(\hat{\mathbf{r}}, t) + \hat{H}'(\hat{\mathbf{r}}, t), \quad (2.1)$$

where $\hat{H}_0(\hat{\mathbf{r}}, t)$ is the unperturbed Hamiltonian of the electron in the presence of the atomic potential and the laser field $\boldsymbol{\mathcal{E}}(t)$,

$$\hat{H}_0(\hat{\mathbf{r}}, t) = \frac{\hat{\mathbf{p}}^2}{2m_e} + V(\hat{\mathbf{r}}) - e\boldsymbol{\mathcal{E}}(t) \cdot \hat{\mathbf{r}}, \quad (2.2)$$

whereas $\hat{H}'(\hat{\mathbf{r}}, t)$ represents its interaction with a quantised electric field $\hat{\boldsymbol{\mathcal{E}}}_{\mathbf{K}}(\hat{\mathbf{r}}, t)$,

$$\hat{H}'(\hat{\mathbf{r}}, t) = -e\hat{\boldsymbol{\mathcal{E}}}_{\mathbf{K}}(\hat{\mathbf{r}}, t) \cdot \hat{\mathbf{r}}. \quad (2.3)$$

More specifically,

$$\hat{\boldsymbol{\mathcal{E}}}_{\mathbf{K}}(\hat{\mathbf{r}}, t) = \hat{\boldsymbol{\mathcal{E}}}_{\mathbf{K}}^{(+)}(\hat{\mathbf{r}}, t) + \hat{\boldsymbol{\mathcal{E}}}_{\mathbf{K}}^{(-)}(\hat{\mathbf{r}}, t), \quad (2.4)$$

where

$$\begin{aligned} \hat{\boldsymbol{\mathcal{E}}}_{\mathbf{K}}^{(+)}(\hat{\mathbf{r}}, t) &= i\boldsymbol{\varepsilon}_{\mathbf{K}}^* \sqrt{\frac{\omega_{\mathbf{K}}}{2\epsilon_0\mathcal{V}}} \hat{a}_{\mathbf{K}} e^{-i(\omega_{\mathbf{K}}t - \mathbf{K} \cdot \hat{\mathbf{r}})}, \\ \hat{\boldsymbol{\mathcal{E}}}_{\mathbf{K}}^{(-)}(\hat{\mathbf{r}}, t) &= -i\boldsymbol{\varepsilon}_{\mathbf{K}} \sqrt{\frac{\omega_{\mathbf{K}}}{2\epsilon_0\mathcal{V}}} \hat{a}_{\mathbf{K}}^\dagger e^{i(\omega_{\mathbf{K}}t - \mathbf{K} \cdot \hat{\mathbf{r}})}. \end{aligned} \quad (2.5)$$

In those formulas, \mathcal{V} is the quantization volume, whereas $\hat{a}_{\mathbf{K}}$ and $\hat{a}_{\mathbf{K}}^\dagger$ are the annihilation and creation operators of a photon with energy $\omega_{\mathbf{K}}$, the wave vector \mathbf{K} , and the polarisation $\boldsymbol{\varepsilon}_{\mathbf{K}}$ ($\mathbf{K} \cdot \boldsymbol{\varepsilon}_{\mathbf{K}} = 0$). Now, we need the probability amplitude to obtain information about the transition between the unperturbed initial and final states of the system governed by the Hamiltonian (2.2).

The probability amplitude of LARA in the length gauge takes the form

$$\mathcal{A}(\mathbf{p}) = -i \int_{-\infty}^{\infty} dt \langle \psi_B(t); 1_{\mathbf{K}} | -e\hat{\boldsymbol{\mathcal{E}}}_{\mathbf{K}}(\hat{\mathbf{r}}, t) \cdot \hat{\mathbf{r}} | \psi_p^{(+)}(t); 0_{\mathbf{K}} \rangle, \quad (2.6)$$

where the initial state of the system $|\psi_p^{(+)}(t); 0_{\mathbf{K}}\rangle = |\psi_p^{(+)}(t)\rangle \otimes |0_{\mathbf{K}}\rangle$ is expressed by the scattering state of electron $\psi_p^{(+)}(\mathbf{r}, t)$ having momentum \mathbf{p} and no photons, and the final state of the system $|\psi_B(t); 1_{\mathbf{K}}\rangle = |\psi_B(t)\rangle \otimes |1_{\mathbf{K}}\rangle$ which defines the electron in the bound state $\psi_B(\mathbf{r}, t)$ of energy E_B and an emitted photon with momentum \mathbf{K} . Using Eqs. (2.4) and (2.5) as well as

relations $\langle 1_{\mathbf{K}} | \hat{a}_{\mathbf{K}}^+ | 0_{\mathbf{K}} \rangle = 1$ and $\langle 1_{\mathbf{K}} | \hat{a}_{\mathbf{K}} | 0_{\mathbf{K}} \rangle = 0$, we get from Eq. (2.6),

$$\mathcal{A}(\mathbf{p}) = e \sqrt{\frac{\omega_{\mathbf{K}}}{2\epsilon_0 \mathcal{V}}} \int_{-\infty}^{\infty} dt \langle \psi_B(t) | (\boldsymbol{\epsilon}_{\mathbf{K}} \cdot \hat{\mathbf{r}}) e^{i\omega_{\mathbf{K}}t - i\mathbf{K} \cdot \hat{\mathbf{r}}} | \psi_{\mathbf{p}}^{(+)}(t) \rangle. \quad (2.7)$$

Introducing the continuous set of basis vectors $|\mathbf{r}\rangle$, satisfying the completeness and orthonormality conditions,

$$\int d^3\mathbf{r} |\mathbf{r}\rangle \langle \mathbf{r}| = 1 \quad (2.8)$$

and

$$\langle \mathbf{r} | \mathbf{r}' \rangle = \delta(\mathbf{r} - \mathbf{r}'), \quad (2.9)$$

respectively, we can rewrite the probability amplitude (2.7) as

$$\mathcal{A}(\mathbf{p}) = e \sqrt{\frac{\omega_{\mathbf{K}}}{2\epsilon_0 \mathcal{V}}} \int_{-\infty}^{\infty} dt \int d^3\mathbf{r} \psi_B^*(\mathbf{r}, t) (\boldsymbol{\epsilon}_{\mathbf{K}} \cdot \mathbf{r}) \psi_{\mathbf{p}}^{(+)}(\mathbf{r}, t) e^{i(\omega_{\mathbf{K}}t - \mathbf{K} \cdot \mathbf{r})}. \quad (2.10)$$

In principle, $\psi_B(\mathbf{r}, t)$ and $\psi_{\mathbf{p}}^{(+)}(\mathbf{r}, t)$ are explicit solutions of the Schrödinger equation with the Hamiltonian $\hat{H}_0(\mathbf{r}, t)$, i.e., for the electron's bound state and the scattering state in the presence of a laser field and an atomic potential. Since they are not known in analytical form, we shall approximate them such that

$$\psi_B(\mathbf{r}, t) = e^{-iE_B t} \psi_B(\mathbf{r}) \quad (2.11)$$

and

$$\psi_{\mathbf{p}}^{(+)}(\mathbf{r}, t) = \frac{1}{\sqrt{\mathcal{V}}} \exp \left[-i \frac{\mathbf{p}^2}{2m_e} t + i(\mathbf{p} - e\mathbf{A}(t)) \cdot \mathbf{r} + \frac{i}{2m_e} \int_0^t d\tau (2e\mathbf{A}(\tau) \cdot \mathbf{p} - e^2 \mathbf{A}^2(\tau)) \right]. \quad (2.12)$$

As we are dealing with the attachment accompanied by short laser pulses, the pulse influence on atomic bound state can be neglected. For this reason, Eq. (2.11) represents the stationary time-evolution of the atomic bound state in the absence of the laser field. On the other hand, Eq. (2.12) describes the electron propagating exclusively in the laser field and having an initial asymptotic momentum \mathbf{p} ; it is known as the Volkov state [65]. Thus, we neglect the influence of the atomic potential in the electron scattering state, which is the essence of SFA. Note that in Eq. (2.12), the laser field is represented by the vector potential $\mathbf{A}(t)$ such that $\boldsymbol{\mathcal{E}}(t) = -\partial_t \mathbf{A}(t)$. Substituting Eqs. (2.11) and (2.12) into Eq. (2.10), we obtain

$$\begin{aligned} \mathcal{A}(\mathbf{p}) &= e \sqrt{\frac{\omega_{\mathbf{K}}}{2\epsilon_0 \mathcal{V}}} \int_{-\infty}^{\infty} dt \exp \left[i(E_B + \omega_{\mathbf{K}} - \frac{\mathbf{p}^2}{2m_e})t + \frac{i}{2m_e} \int_0^t d\tau (2e\mathbf{A}(\tau) \cdot \mathbf{p} - e^2 \mathbf{A}^2(\tau)) \right] \\ &\times \int d^3\mathbf{r} \psi_B^*(\mathbf{r}) (\boldsymbol{\epsilon}_{\mathbf{K}} \cdot \mathbf{r}) \exp \left[i(\mathbf{p} - e\mathbf{A}(t) - \mathbf{K}) \cdot \mathbf{r} \right]. \end{aligned} \quad (2.13)$$

Introducing,

$$\boldsymbol{\pi}(t) = \mathbf{p} - e\mathbf{A}(t) - \mathbf{K}, \quad (2.14)$$

the second line in Eq. (2.13) takes the form,

$$\tilde{\Phi}_B[\boldsymbol{\pi}(t)] = \int d^3\mathbf{r} \psi_B^*(\mathbf{r})(\boldsymbol{\varepsilon}_K \cdot \mathbf{r}) e^{i\boldsymbol{\pi}(t) \cdot \mathbf{r}} = -i(\boldsymbol{\varepsilon}_K \cdot \nabla_{\boldsymbol{\pi}}) \tilde{\psi}_B^*[\boldsymbol{\pi}(t)], \quad (2.15)$$

where $\tilde{\psi}_B[\boldsymbol{\pi}(t)]$ represents the Fourier transform of $\psi_B(\mathbf{r})$, whereas $\nabla_{\boldsymbol{\pi}}$ is the gradient with respect to $\boldsymbol{\pi}$. Now the probability amplitude of radiative attachment (2.13) can be written as

$$\mathcal{A}(\mathbf{p}) = \frac{e}{\mathcal{V}} \sqrt{\frac{\omega_K}{2\varepsilon_0}} \int_{-\infty}^{\infty} dt \tilde{\Phi}_B[\boldsymbol{\pi}(t)] e^{iQt+iH(t)}, \quad (2.16)$$

where

$$Q = E_B + \omega_K - \frac{\mathbf{p}^2}{2m_e}, \quad (2.17)$$

$$H(t) = \int_0^t d\tau h(\tau), \quad (2.18)$$

and

$$h(t) = \frac{e}{m_e} \mathbf{p} \cdot \mathbf{A}(t) - \frac{e^2}{2m_e} \mathbf{A}^2(t). \quad (2.19)$$

Suppose an electron recombines with a hydrogen atom to form an H^- ion in the presence of a laser field. Following the work of Gribakin and Kuchiev [66], we take for the ground state wave function of H^- ,

$$\psi_B(\mathbf{r}) = \frac{A}{\sqrt{4\pi}} \frac{e^{-\kappa r}}{r}, \quad (2.20)$$

where $\kappa = \sqrt{2m_e|E_B|} = 0.2354p_0$ and $A = 0.75\sqrt{p_0}$. In this case,

$$\tilde{\Phi}_B[\boldsymbol{\pi}(t)] = -i(\boldsymbol{\varepsilon}_K \cdot \nabla_{\boldsymbol{\pi}}) \int d^3\mathbf{r} \frac{A}{\sqrt{4\pi}} \frac{e^{-\kappa r}}{r} e^{i\boldsymbol{\pi}(t) \cdot \mathbf{r}}. \quad (2.21)$$

Performing the position integral in spherical coordinates, we arrive at

$$\tilde{\Phi}_B[\boldsymbol{\pi}(t)] = -2\sqrt{\pi}iA(\boldsymbol{\varepsilon}_K \cdot \nabla_{\boldsymbol{\pi}}) \frac{1}{\kappa^2 + \boldsymbol{\pi}^2(t)}, \quad (2.22)$$

which after calculating the gradient leads to

$$\tilde{\Phi}_B[\boldsymbol{\pi}(t)] = 4i\sqrt{\pi}A \frac{\boldsymbol{\varepsilon}_K \cdot \boldsymbol{\pi}(t)}{[\kappa^2 + \boldsymbol{\pi}^2(t)]^2}. \quad (2.23)$$

Putting the function $\tilde{\Phi}_B[\boldsymbol{\pi}(t)]$ into the definition of the probability amplitude (2.16) and recalling that $\boldsymbol{\varepsilon}_K \cdot \mathbf{K} = 0$, we come up with the following expression for the probability amplitude of LARA within the SFA,

$$\mathcal{A}(\mathbf{p}) = 4iA \sqrt{\frac{\pi\omega_K}{2\varepsilon_0}} \frac{e}{\mathcal{V}} \int_{-\infty}^{\infty} dt \frac{\boldsymbol{\varepsilon}_K \cdot [\mathbf{p} - e\mathbf{A}(t)]}{[\kappa^2 + \boldsymbol{\pi}^2(t)]^2} e^{iQt+iH(t)}. \quad (2.24)$$

Next, the goal is to show that the above integral incorporates the contribution from the laser-field-free process.

Since we consider the recombination process assisted by a laser field, which lasts from 0 to T_p , its corresponding vector potential is zero except for $t \in [0, T_p]$. Because of that, the integral in Eq. (2.24) splits into two integrals,

$$\mathcal{A}(\mathbf{p}) = 4iA \sqrt{\frac{\pi\omega_{\mathbf{K}}}{2\epsilon_0}} \frac{e}{\mathcal{V}} \left[\boldsymbol{\varepsilon}_{\mathbf{K}} \cdot \mathbf{p} \int_{-\infty}^{\infty} dt \frac{e^{iQt+iH(t)}}{[\kappa^2 + \pi^2(t)]^2} - \int_0^{T_p} dt \frac{\boldsymbol{\varepsilon}_{\mathbf{K}} \cdot e\mathbf{A}(t)}{[\kappa^2 + \pi^2(t)]^2} e^{iQt+iH(t)} \right], \quad (2.25)$$

where the first one needs special treatment. Below we shall demonstrate how to regularise this integral by means of the Boca-Florescu transformation [67].

Consider the following integral,

$$I(\epsilon) = \int_{-\infty}^{\infty} dt \frac{e^{iQt+iH(t)-\epsilon|t|}}{[\kappa^2 + \pi^2(t)]^2}, \quad (2.26)$$

where the parameter ϵ is chosen such that this integral is convergent; namely, $\epsilon > 0$. As one can see, the regularised integral (2.26) reproduces the divergent integral in Eq. (2.25) in the limit when $\epsilon \rightarrow 0^+$. Now, dividing the integral $I(\epsilon)$ into two intervals $[-\infty, 0]$ and $[0, \infty]$, we obtain

$$I(\epsilon) = \int_{-\infty}^0 dt \frac{e^{i(Q-i\epsilon)t+iH(t)}}{[\kappa^2 + \pi^2(t)]^2} + \int_0^{\infty} dt \frac{e^{i(Q+i\epsilon)t+iH(t)}}{[\kappa^2 + \pi^2(t)]^2}. \quad (2.27)$$

Calculating both integrals by parts, we arrive at

$$\begin{aligned} I(\epsilon) &= \frac{e^{iH(0)}}{[\kappa^2 + \pi^2(0)]^2} \left[\frac{1}{i(Q-i\epsilon)} - \frac{1}{i(Q+i\epsilon)} \right] - \frac{1}{i(Q-i\epsilon)} \int_{-\infty}^0 dt e^{i(Q-i\epsilon)t} \left(\frac{e^{iH(t)}}{[\kappa^2 + \pi^2(t)]^2} \right)' \\ &\quad - \frac{1}{i(Q+i\epsilon)} \int_0^{\infty} dt e^{i(Q+i\epsilon)t} \left(\frac{e^{iH(t)}}{[\kappa^2 + \pi^2(t)]^2} \right)', \end{aligned} \quad (2.28)$$

where the prime denotes the time derivative. The values of functions $H(t)$ and $\pi(t)$ at $t = 0$ can be calculated from Eqs. (2.14) and (2.19),

$$H(0) = 1, \quad \pi(0) = \mathbf{p} - \mathbf{K} \equiv \boldsymbol{\pi}_0. \quad (2.29)$$

In addition, the derivative in Eq. (2.28) takes the form

$$\left(\frac{e^{iH(t)}}{[\kappa^2 + \pi^2(t)]^2} \right)' = \frac{iF(t)}{[\kappa^2 + \pi^2(t)]^2} e^{iH(t)}, \quad (2.30)$$

where the function $F(t)$ is

$$F(t) = h(t) + 4i \frac{e\boldsymbol{\mathcal{E}}(t) \cdot \boldsymbol{\pi}(t)}{\kappa^2 + \pi^2(t)}, \quad (2.31)$$

with $h(t)$ given by Eq. (2.19). Note that $F(t)$ is zero beyond the interval $[0, T_p]$ and so the derivative defined in Eq. (2.30). Taking this into account, we conclude that Eq. (2.28) becomes

$$I(\epsilon) = \frac{1}{(\kappa^2 + \pi_0^2)^2} \frac{2\epsilon}{Q^2 + \epsilon^2} - \frac{1}{Q + i\epsilon} \int_0^{T_p} dt \frac{F(t)}{[\kappa^2 + \pi^2(t)]^2} e^{i(Q+i\epsilon)t+iH(t)}. \quad (2.32)$$

One needs to look for the limit of the above expression as $\epsilon \rightarrow 0^+$. Knowing that [68]

$$\delta(Q) = \frac{1}{\pi} \lim_{\epsilon \rightarrow 0^+} \frac{\epsilon}{Q^2 + \epsilon^2}, \quad (2.33)$$

Eq. (2.32) takes the form,

$$\lim_{\epsilon \rightarrow 0^+} I(\epsilon) = \int_{-\infty}^{\infty} dt \frac{e^{iQt+iH(t)}}{[\kappa^2 + \pi^2(t)]^2} = \frac{2\pi}{(\kappa^2 + \pi_0^2)^2} \delta(Q) - \frac{1}{Q + i\epsilon} \int_0^{T_p} dt \frac{F(t)}{[\kappa^2 + \pi^2(t)]^2} e^{iQt+iH(t)}. \quad (2.34)$$

The latter defines the first integral in Eq. (2.25) and was obtained following Boca and Florescu treatment [67].

After Boca-Florescu transformation (2.34), the probability amplitude of LARA to form H^- ion equals

$$\begin{aligned} \mathcal{A}(\mathbf{p}) = 4iA \sqrt{\frac{\pi\omega_{\mathbf{K}}}{2\epsilon_0}} \frac{e}{\mathcal{V}} \left[2\pi\delta(Q) \frac{\boldsymbol{\varepsilon}_{\mathbf{K}} \cdot \mathbf{p}}{(\kappa^2 + \pi_0^2)^2} - \frac{\boldsymbol{\varepsilon}_{\mathbf{K}} \cdot \mathbf{p}}{Q + i\epsilon} \int_0^{T_p} dt \frac{F(t)}{[\kappa^2 + \pi^2(t)]^2} e^{iQt+iH(t)} \right. \\ \left. - \int_0^{T_p} dt \frac{\boldsymbol{\varepsilon}_{\mathbf{K}} \cdot e\mathbf{A}(t)}{[\kappa^2 + \pi^2(t)]^2} e^{iQt+iH(t)} \right], \end{aligned} \quad (2.35)$$

where the prescription $i\epsilon$ ($\epsilon > 0$) allows to avoid the singularity at $Q = 0$.

In principle, the emitted LARA radiation can be elliptically polarised, meaning that

$$\boldsymbol{\varepsilon}_{\mathbf{K}} = \cos \delta \boldsymbol{\varepsilon}_{\mathbf{K}1} + i \sin \delta \boldsymbol{\varepsilon}_{\mathbf{K}2}, \quad (2.36)$$

where $\boldsymbol{\varepsilon}_{\mathbf{K}1}$ and $\boldsymbol{\varepsilon}_{\mathbf{K}2}$ are linearly polarised vectors such that they satisfy orthonormality condition $\boldsymbol{\varepsilon}_{\mathbf{K}i} \cdot \boldsymbol{\varepsilon}_{\mathbf{K}j} = \delta_{ij}$ for $i, j \in \{1, 2\}$ and δ is the ellipticity parameter. Taking Eq. (2.35) into consideration, we define the partial probability amplitude for each linear polarisation $\boldsymbol{\varepsilon}_{\mathbf{K}j}$ ($j = 1, 2$),

$$\mathcal{R}_j^{(0)} = A(\mathbf{n}_{\mathbf{p}} \cdot \boldsymbol{\varepsilon}_{\mathbf{K}j}) \frac{1}{(\kappa^2 + \pi_0^2)^2}, \quad (2.37)$$

$$\mathcal{R}_j^{(1)} = A(\mathbf{n}_{\mathbf{p}} \cdot \boldsymbol{\varepsilon}_{\mathbf{K}j}) \int_0^{T_p} dt \frac{F(t)}{[\kappa^2 + \pi^2(t)]^2} e^{iQt+iH(t)}, \quad (2.38)$$

$$\mathcal{R}_j^{(2)} = -A \int_0^{T_p} dt \frac{\boldsymbol{\varepsilon}_{\mathbf{K}j} \cdot e\mathbf{A}(t)}{[\kappa^2 + \pi^2(t)]^2} e^{iQt+iH(t)}, \quad (2.39)$$

where $\mathbf{n}_{\mathbf{p}} = \mathbf{p}/|\mathbf{p}|$ stands for the direction of the electron's initial momentum. Introducing the following abbreviation,

$$\mathcal{R}_\delta^{(\ell)} = \cos \delta \mathcal{R}_1^{(\ell)} + i \sin \delta \mathcal{R}_2^{(\ell)} \quad (2.40)$$

for $\ell = 0, 1, 2$, and a constant

$$\mathcal{N} = 4i\sqrt{\frac{\pi\omega_{\mathbf{K}}}{2\epsilon_0}} \frac{e}{\mathcal{V}} = -\frac{4\pi i}{\mathcal{V}} \sqrt{2\alpha c\omega_{\mathbf{K}}}, \quad (2.41)$$

we rewrite Eq. (2.35) as

$$\mathcal{A}(\mathbf{p}) = \mathcal{N} \left[2\pi|\mathbf{p}|\delta(Q)\mathcal{R}_{\delta}^{(0)} - \frac{|\mathbf{p}|}{Q+i\epsilon}\mathcal{R}_{\delta}^{(1)} + \mathcal{R}_{\delta}^{(2)} \right]. \quad (2.42)$$

It follows from Eqs. (2.31), (2.38), (2.39), and (2.40) that $\mathcal{R}_{\delta}^{(1)}$ and $\mathcal{R}_{\delta}^{(2)}$ are laser-field-dependent terms whereas $\mathcal{R}_{\delta}^{(0)}$ is a laser-field-independent term. It implies that in the absence of the laser field, $\mathcal{R}_{\delta}^{(1)} = \mathcal{R}_{\delta}^{(2)} = 0$. Nevertheless, the probability amplitude of radiative attachment is nonzero. Namely, for the laser-field-free process, the probability amplitude equals [27]

$$\mathcal{A}_{\text{FF}}(\mathbf{p}) = 2\pi\mathcal{N}|\mathbf{p}|\delta(Q)\mathcal{R}_{\delta}^{(0)}. \quad (2.43)$$

As it is well-known, the Dirac delta function in (2.43) conveys the energy conservation condition. Hence, in the absence of the laser field, we observe monochromatic radiation with energy,

$$\omega_{\mathbf{K}} = \frac{\mathbf{p}^2}{2m_e} + |E_B|. \quad (2.44)$$

As we will see later on, this spectral line (while modified) is embedded in a more complicated spectral pattern associated with the presence of a laser field.

In closing this Section, we note that in the presence of a monochromatic electron wave, the probability amplitude of LARA [Eq. (2.42)] has a laser-field-free singularity at $Q = 0$. As shown next, this singularity can be smeared out by considering an electron wave packet instead.

2.2.2 LARA by an impact of an electron wave packet

Now, we consider an impact of a coherent electron wave packet $\psi_{\mathbf{p}}^{(+)}[\mathbf{r}, t|f_{\mathbf{p}}]$ on a hydrogen atom in the presence of a laser field. We assume that the profile of the wave packet $f_{\mathbf{p}}(\mathbf{q})$ is peaked around the momentum \mathbf{p} such that

$$f_{\mathbf{p}}(\mathbf{q}) \approx \delta^{(3)}(\mathbf{q} - \mathbf{p}). \quad (2.45)$$

Thus, it describes the nearly monochromatic electron beam. Defining the initial wave packet of the electron,

$$\psi_{\mathbf{p}}^{(+)}[\mathbf{r}, t|f_{\mathbf{p}}] = \int d^3\mathbf{q} \psi_{\mathbf{q}}^{(+)}(\mathbf{r}, t) f_{\mathbf{p}}(\mathbf{q}), \quad (2.46)$$

we learn that the probability amplitude of LARA [Eq. (2.10)] integrated over the initial electron momentum profile equals

$$\langle \mathcal{A}(\mathbf{p}) \rangle = \int d^3\mathbf{q} \mathcal{A}(\mathbf{q}) f_{\mathbf{p}}(\mathbf{q}). \quad (2.47)$$

This means that we account coherently for all contributions from different electron scattering waves which contribute to Eq. (2.46). Now, taking into account the formula (2.42), we derive

that

$$\langle \mathcal{A}(\mathbf{p}) \rangle = \mathcal{N} \langle \mathcal{R}_\delta(\mathbf{p}) \rangle, \quad (2.48)$$

where

$$\langle \mathcal{R}_\delta(\mathbf{p}) \rangle = 2\pi |\mathbf{p}| \mathcal{R}_\delta^{(0)} \langle \delta(Q) \rangle - |\mathbf{p}| \left\langle \frac{1}{Q + i\epsilon} \right\rangle \mathcal{R}_\delta^{(1)} + \mathcal{R}_\delta^{(2)}. \quad (2.49)$$

Here, the amplitudes $\mathcal{R}_\delta^{(0)}$, $\mathcal{R}_\delta^{(1)}$, and $\mathcal{R}_\delta^{(2)}$ are slowly varying functions of their arguments. Besides that,

$$\langle \delta(Q) \rangle = \int d^3 \mathbf{q} \delta(Q_q) f_p(\mathbf{q}), \quad (2.50)$$

$$\left\langle \frac{1}{Q + i\epsilon} \right\rangle = \int d^3 \mathbf{q} \frac{f_p(\mathbf{q})}{Q_q + i\epsilon}, \quad (2.51)$$

and

$$Q_q = E_B + \omega_{\mathbf{K}} - \frac{\mathbf{q}^2}{2m_e}. \quad (2.52)$$

The total energy illuminated (per initial electron flux) in LARA is obtained when integrating over the density of final radiation states, $V d^3 \mathbf{K} / (2\pi)^3$,

$$E_{\mathbf{K}}(\mathbf{p}) = \frac{1}{j_e(\mathbf{p})} \int \frac{V d^3 \mathbf{K}}{(2\pi)^3} \omega_{\mathbf{K}} |\langle \mathcal{A}(\mathbf{p}) \rangle|^2. \quad (2.53)$$

Since the wave vector and angular frequency of the emitted photons are related to each other such that $|\mathbf{K}| = \omega_{\mathbf{K}}/c$, we derive that $d^3 \mathbf{K} = \omega_{\mathbf{K}}^2 d\omega_{\mathbf{K}} d^2 \Omega_{\mathbf{K}} / c^3$, where $d^2 \Omega_{\mathbf{K}}$ is the solid angle of emitted photons. Moreover, the initial electron flux per the quantisation volume is

$$j_e(\mathbf{p}) = \frac{|\mathbf{p}|}{m_e} \frac{1}{\mathcal{V}}. \quad (2.54)$$

Substituting Eqs. (2.41), (2.48), and (2.54) into Eq. (2.53) we obtain

$$E_{\mathbf{K}}(\mathbf{p}) = \frac{4\alpha}{\pi c^2} \frac{m_e}{|\mathbf{p}|} \int d^2 \Omega_{\mathbf{K}} \int d\omega_{\mathbf{K}} \omega_{\mathbf{K}}^4 |\langle \mathcal{R}_\delta(\mathbf{p}) \rangle|^2. \quad (2.55)$$

The last expression can be written as

$$E_{\mathbf{K}}(\mathbf{p}) = \int d^2 \Omega_{\mathbf{K}} \int d\omega_{\mathbf{K}} \frac{d^3 E_{\mathbf{K}}(\mathbf{p})}{d\omega_{\mathbf{K}} d^2 \Omega_{\mathbf{K}}}, \quad (2.56)$$

from where we deduce that the triply differential energy distribution (per the initial electron flux) of photons emitted in the solid angle $d^2 \Omega_{\mathbf{K}}$ and having energy within the interval $(\omega_{\mathbf{K}}, \omega_{\mathbf{K}} + d\omega_{\mathbf{K}})$ is

$$\frac{d^3 E_{\mathbf{K}}(\mathbf{p})}{d\omega_{\mathbf{K}} d^2 \Omega_{\mathbf{K}}} = \frac{4\alpha}{\pi c^2} \frac{m_e}{|\mathbf{p}|} \omega_{\mathbf{K}}^4 |\langle \mathcal{R}_\delta(\mathbf{p}) \rangle|^2. \quad (2.57)$$

Here, $\langle \mathcal{R}_\delta(\mathbf{p}) \rangle$ has been given by Eq. (2.49). Based on this result, we will compare the previously formed theory [56, 57, 58, 59, 60, 61] with our complete theory in Section 2.3. For now, let us briefly introduce the previously formed theory of LARA, which we refer to as the simplified one.

2.2.3 Simplified formulation of LARA

Let us go back to the definition of transition amplitude (2.24) defined in the beginning of this Chapter. Instead of keeping the time integral from $-\infty$ to $+\infty$, we will forcefully reduce it to the duration of the laser field, $[0, T_p]$, similar to Refs. [56, 57, 58, 59, 60, 61]. Hence, the transition amplitude takes the form,

$$\mathcal{A}(\mathbf{p}) = 4iA \sqrt{\frac{\pi\omega_{\mathbf{K}}}{2\epsilon_0}} \frac{e}{\mathcal{V}} \int_0^{T_p} dt \frac{\boldsymbol{\varepsilon}_{\mathbf{K}} \cdot [\mathbf{p} - e\mathbf{A}(t)]}{[\kappa^2 + \pi^2(t)]^2} e^{iQt+iH(t)}. \quad (2.58)$$

It is equivalent to replacing the function $G(t) = \frac{\boldsymbol{\varepsilon}_{\mathbf{K}} \cdot [\mathbf{p} - e\mathbf{A}(t)]}{[\kappa^2 + \pi^2(t)]^2}$ by $G(t)\theta(t)\theta(T_p - t)$, where $\theta(\cdot)$ is the step function. By doing that, we artificially force the integrand to be zero at times $t = 0$ and $t = T_p$, and beyond. It also means that there is discontinuity in the integrand at $t = 0$ and $t = T_p$. This sharp cutoff of the integration limits may lead to some false effects in the energy distribution of LARA, which will be shown in Section 2.3. We also bring into focus that the above formula overlaps with Eq. (2.24) only if $\boldsymbol{\varepsilon}_{\mathbf{K}} \cdot \mathbf{p} = 0$, i.e., when the polarisation of LARA photons and electron initial momentum are perpendicular to each other. This is, however, the least favorable setup for LARA, when the LARA photons are generated in the direction of initial electron (see, Section 2.3.1 for numerical illustration). Introducing here $\boldsymbol{\varepsilon}_{\mathbf{K}}$ in the most general form (2.36), we can rewrite Eq. (2.58) as $\mathcal{A}(\mathbf{p}) = \mathcal{N} \tilde{\mathcal{R}}_\delta$ where \mathcal{N} is defined by Eq. (2.41),

$$\tilde{\mathcal{R}}_\delta = \cos \delta \tilde{\mathcal{R}}_1 + i \sin \delta \tilde{\mathcal{R}}_2, \quad (2.59)$$

and

$$\tilde{\mathcal{R}}_j = A \int_0^{T_p} dt \frac{\boldsymbol{\varepsilon}_{\mathbf{K}j} \cdot [\mathbf{p} - e\mathbf{A}(t)]}{[\kappa^2 + \pi^2(t)]^2} e^{iQt+iH(t)}. \quad (2.60)$$

Since we want to show the comparison between the results of the current theory and our complete theory, we average Eq. (2.58) with respect to the initial electron momentum distribution $f_{\mathbf{p}}(\mathbf{q})$ [Eq. (2.47)]. Since $\tilde{\mathcal{R}}_\delta$ is a regular function of the electron momentum, such averaging provides

$$\langle \mathcal{A}(\mathbf{p}) \rangle = \mathcal{N} \tilde{\mathcal{R}}_\delta(\mathbf{p}). \quad (2.61)$$

In order to define the energy distribution of the emitted radiation per the initial electron flux (per quantisation volume), we follow the same approach as demonstrated in Section 2.2.2. It turns out that

$$\frac{d^3 E_{\mathbf{K}}(\mathbf{p})}{d\omega_{\mathbf{K}} d^2 \Omega_{\mathbf{K}}} = \frac{4\alpha}{\pi c^2} \frac{m_e}{|\mathbf{p}|} \omega_{\mathbf{K}}^4 |\langle \tilde{\mathcal{R}}_\delta(\mathbf{p}) \rangle|^2. \quad (2.62)$$

Thus, in Section 2.3 we shall calculate (2.57) and (2.62) numerically and compare both formulations.

2.2.4 Electron wave packet model

In order to proceed with numerical calculations, it is necessary to set the profile $f_{\mathbf{p}}(\mathbf{q})$ of the electron wave packet that satisfies (2.45). For a well-collimated beam, we choose cylindrical coordinate system to define the momentum profile of the electron wave packet. The cylindrical coordinates are considered with respect to the direction of the central momentum of the electron wave packet, $\mathbf{n}_{\mathbf{p}} = \mathbf{p}/|\mathbf{p}|$. Thus, the longitudinal and the transverse components of electron momenta are defined as $q_{\parallel} = \mathbf{q} \cdot \mathbf{n}_{\mathbf{p}}$ and $\mathbf{q}_{\perp} = \mathbf{q} - q_{\parallel} \mathbf{n}_{\mathbf{p}}$, respectively. While we assume that the spread of the electron wave packet in the direction perpendicular to \mathbf{p} is negligible, the profile of the wave packet for contributing longitudinal momentum components is of a Lorentzian type. The contributing longitudinal momentum distribution is peaked at $|\mathbf{p}|$ and has a half-width at half-maximum (HWHM) equal to $\Delta|\mathbf{p}|$. Hence, we assume that

$$f_{\mathbf{p}}(\mathbf{q}) = \frac{1}{\pi} \frac{\Delta|\mathbf{p}|}{(q_{\parallel} - |\mathbf{p}|)^2 + (\Delta|\mathbf{p}|)^2} \delta^{(2)}(\mathbf{q}_{\perp}), \quad (2.63)$$

where

$$\lim_{\Delta|\mathbf{p}| \rightarrow 0} \frac{1}{\pi} \frac{\Delta|\mathbf{p}|}{(q_{\parallel} - |\mathbf{p}|)^2 + (\Delta|\mathbf{p}|)^2} = \delta^{(1)}(q_{\parallel} - |\mathbf{p}|). \quad (2.64)$$

With this model of the wave packet profile (2.45), it is possible to estimate the averages given by Eqs. (2.50) and (2.51). It follows from Eq. (2.50) that

$$\langle \delta(Q) \rangle = \int d^3\mathbf{q} f_{\mathbf{p}}(\mathbf{q}) \delta(Q_{\mathbf{q}}) = \frac{1}{\pi} \int d^3\mathbf{q} \frac{\Delta|\mathbf{p}|}{(q_{\parallel} - |\mathbf{p}|)^2 + (\Delta|\mathbf{p}|)^2} \delta^{(2)}(\mathbf{q}_{\perp}) \delta(Q_{\mathbf{q}}), \quad (2.65)$$

where $Q_{\mathbf{q}}$ is given by Eq. (2.52). Performing the integral over \mathbf{q}_{\perp} , we obtain

$$\langle \delta(Q) \rangle = \frac{1}{\pi} \int_{-\infty}^{+\infty} dq_{\parallel} \frac{\Delta|\mathbf{p}|}{(q_{\parallel} - |\mathbf{p}|)^2 + (\Delta|\mathbf{p}|)^2} \delta(Q_{q_{\parallel}}), \quad (2.66)$$

where $Q_{q_{\parallel}} = E_B + \omega_{\mathbf{K}} - \frac{q_{\parallel}^2}{2m_e}$. Using property of a delta function, $\delta(f(x)) = \sum_i \frac{1}{|f'(x_i)|} \delta(x - x_i)$ where $f(x_i) = 0$, we find that

$$\langle \delta(Q) \rangle = \frac{m_e}{\pi q_0} \int_{-\infty}^{+\infty} dq_{\parallel} \frac{\Delta|\mathbf{p}|}{(q_{\parallel} - |\mathbf{p}|)^2 + (\Delta|\mathbf{p}|)^2} [\delta(q_{\parallel} - q_0) + \delta(q_{\parallel} + q_0)], \quad (2.67)$$

where $q_0 = \sqrt{2m_e(E_B + \omega_{\mathbf{K}})}$ is the magnitude of the initial electron momentum which results in the laser-field-free peak. Taking into account that $f_{\mathbf{p}}(\mathbf{q})$ is peaked around a positive value of q_{\parallel} , we conclude that the second term in this integral does not contribute. Hence,

$$\langle \delta(Q) \rangle = \frac{m_e}{\pi q_0} \frac{\Delta|\mathbf{p}|}{(q_0 - |\mathbf{p}|)^2 + (\Delta|\mathbf{p}|)^2}. \quad (2.68)$$

Similarly, taking Eq. (2.51), we obtain

$$\left\langle \frac{1}{Q + i\epsilon} \right\rangle = \int d^3\mathbf{q} \frac{f_{\mathbf{p}}(\mathbf{q})}{Q_{\mathbf{q}} + i\epsilon} = \frac{1}{\pi} \int d^3\mathbf{q} \frac{1}{Q_{\mathbf{q}} + i\epsilon} \frac{\Delta|\mathbf{p}|}{(q_{\parallel} - |\mathbf{p}|)^2 + (\Delta|\mathbf{p}|)^2} \delta^{(2)}(\mathbf{q}_{\perp}). \quad (2.69)$$

Again, the integral over the transverse components of electron momentum \mathbf{q}_\perp can be easily performed. This leads to

$$\left\langle \frac{1}{Q + i\epsilon} \right\rangle = \frac{1}{\pi} \int_{-\infty}^{+\infty} dq_\parallel \frac{1}{Q_{q_\parallel} + i\epsilon} \frac{\Delta|\mathbf{p}|}{(q_\parallel - |\mathbf{p}|)^2 + (\Delta|\mathbf{p}|)^2}, \quad (2.70)$$

or, writing Q_{q_\parallel} explicitly,

$$\left\langle \frac{1}{Q + i\epsilon} \right\rangle = \frac{2m_e}{\pi} \int_{-\infty}^{+\infty} dq_\parallel \frac{1}{q_0^2 - q_\parallel^2 + i\epsilon} \frac{\Delta|\mathbf{p}|}{(q_\parallel - |\mathbf{p}|)^2 + (\Delta|\mathbf{p}|)^2}. \quad (2.71)$$

The integrand in Eq. (2.71) has four complex poles at $q_\parallel = |\mathbf{p}| \pm i\Delta|\mathbf{p}|$ and $q_\parallel^2 = q_0^2 + i\epsilon$. For the latter, we find that $q_\parallel = \pm q_0 \sqrt{1 + \frac{i\epsilon}{q_0^2}} \approx \pm q_0 \left(1 + \frac{i\epsilon}{2q_0^2}\right)$. Using the Cauchy's residue theorem, we calculate the integral in (2.71) over the contour that is closed by the upper semicircle. In this case, only poles from the upper quadrant of the complex plane will contribute to the integral. Hence, we obtain

$$\begin{aligned} \left\langle \frac{1}{Q + i\epsilon} \right\rangle &= 4im_e \Delta|\mathbf{p}| \left[\frac{q_\parallel - q_0 - \frac{i\epsilon}{2q_0}}{q_0^2 - q_\parallel^2 + i\epsilon} \frac{1}{(q_\parallel - |\mathbf{p}|)^2 + (\Delta|\mathbf{p}|)^2} \Bigg|_{q_\parallel = q_0 + \frac{i\epsilon}{2q_0}} + \right. \\ &\quad \left. + \frac{1}{q_0^2 - q_\parallel^2 + i\epsilon} \frac{q_\parallel - |\mathbf{p}| - i\Delta|\mathbf{p}|}{(q_\parallel - |\mathbf{p}|)^2 + (\Delta|\mathbf{p}|)^2} \Bigg|_{q_\parallel = |\mathbf{p}| + i\Delta|\mathbf{p}|} \right]. \end{aligned} \quad (2.72)$$

For ϵ going to 0 and in the leading order of $\Delta|\mathbf{p}|$, we obtain from Eq. (2.72),

$$\left\langle \frac{1}{Q + i\epsilon} \right\rangle = -\frac{2im_e}{q_0} \frac{\Delta|\mathbf{p}|}{(q_0 - |\mathbf{p}|)^2 + (\Delta|\mathbf{p}|)^2} + \frac{2m_e}{q_0^2 - \mathbf{p}^2 - 2i|\mathbf{p}|\Delta|\mathbf{p}|}. \quad (2.73)$$

Note that we can write the first term in the above expressions in terms of $\langle \delta(Q) \rangle$. Hence, we have

$$\left\langle \frac{1}{Q + i\epsilon} \right\rangle = -2i\pi \langle \delta(Q) \rangle + \frac{2m_e}{q_0^2 - \mathbf{p}^2 - 2i|\mathbf{p}|\Delta|\mathbf{p}|}. \quad (2.74)$$

In addition, as it follows from the Sokhotski-Plemelj formula [68], $\left\langle \frac{1}{Q + i\epsilon} \right\rangle = \langle \mathcal{P}\left(\frac{1}{Q}\right) \rangle - i\pi \langle \delta(Q) \rangle$. Combining it with Eq. (2.73), we obtain that

$$\left\langle \mathcal{P}\left(\frac{1}{Q}\right) \right\rangle = \frac{2m_e}{q_0^2 - \mathbf{p}^2 - 2i|\mathbf{p}|\Delta|\mathbf{p}|} - i\pi \langle \delta(Q) \rangle. \quad (2.75)$$

These formulas permit us to calculate $\langle \mathcal{R}_\delta(\mathbf{p}) \rangle$ according to Eq. (2.49) and, consequently, the energy distribution defined by Eq. (2.57). In closing this Section, we would like to note that the same results can be derived by closing the contour in Eq. (2.69) with the lower semicircle. A somewhat different approach can be also developed (see, Appendix A.1) which agrees with the current formulas.

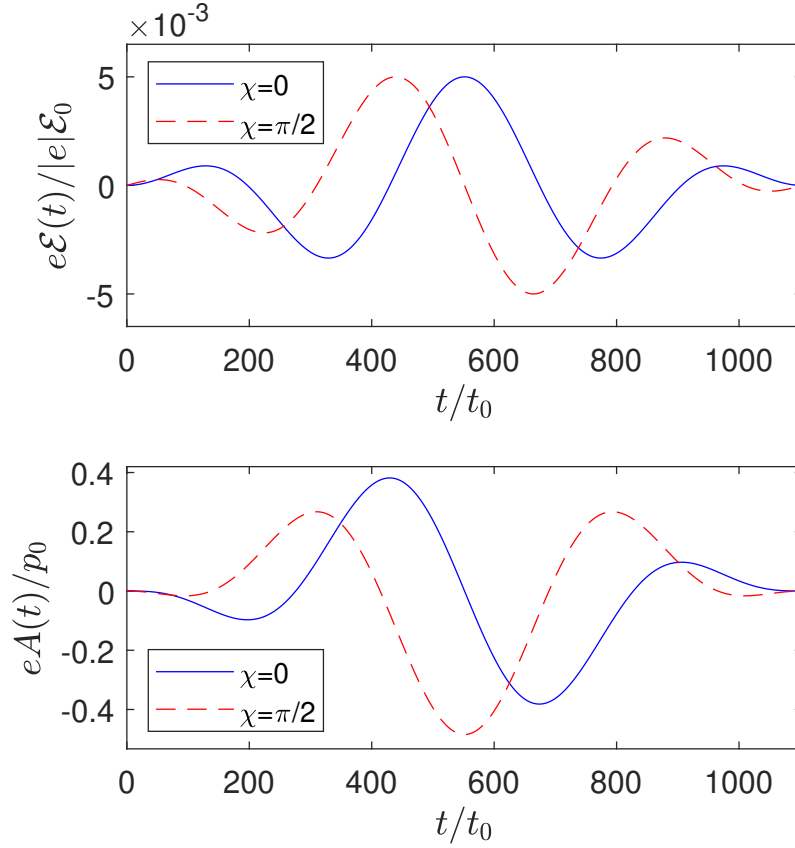


FIGURE 2.1: Temporal profiles of the electric field $\mathcal{E}(t)$ and the vector potential $A(t)$ of a 4000 nm ($\omega = 0.31$ eV) two-cycle ($N_{\text{osc}} = 2$) laser pulse ($N_{\text{rep}} = 1$) with a sine-squared envelope ($M = 1$); see, Eq. (2.76). The intensity parameter is set to $\eta = 0.005$, so the laser peak intensity equals $I_{\text{max}} = 1.76 \times 10^{12}$ W/cm², and the carrier-envelope phase χ is indicated in each panel.

2.2.5 Laser field model

In our numerical illustrations, we shall use a linearly polarised laser field that is given by a vector potential $\mathbf{A}(t) = A(t)\boldsymbol{\varepsilon}$ such that

$$A(t) = \begin{cases} A_0 \sin^{2M} \left(\frac{\omega t}{2N_{\text{osc}}} \right) \sin(\omega t + \chi) & \text{if } 0 \leq t \leq T_p; \\ 0 & \text{otherwise.} \end{cases} \quad (2.76)$$

In principle, it represents the train of identical N_{rep} laser pulses having minimum (zero) delay to guarantee the temporal separation between them. The individual pulse lasts for $\tau_p = 2\pi N_{\text{osc}}/\omega$, meaning that the time duration of the entire train of pulses equals $T_p = N_{\text{rep}}\tau_p$. Here, ω means the carrier frequency, N_{osc} represents the number of cycles in an individual pulse, χ stands for its carrier-envelope phase (CEP), and the parameter M for shaping a pulse envelope. We specify the constant A_0 such that the corresponding electric field $\boldsymbol{\mathcal{E}}(t) = \mathcal{E}(t)\boldsymbol{\varepsilon}$, where $\mathcal{E}(t) = -\partial A(t)/\partial t$, meets the condition,

$$\max_{0 \leq t \leq T_p} |\mathcal{E}(t)| = \eta \mathcal{E}_0. \quad (2.77)$$

Hence, the maximum field intensity is

$$I_{\max} = \epsilon_0 c \eta^2 \mathcal{E}_0^2 = \eta^2 I_0, \quad (2.78)$$

where η is an arbitrary constant. As an illustration, for a two-cycle laser pulse ($N_{\text{rep}} = 1$, $N_{\text{osc}} = 2$), in Fig. 2.1 we plot the time-dependence of the electric field $\mathcal{E}(t)$ and the vector potential $A(t)$ having wavelength $\lambda = 2\pi c/\omega = 4000$ nm (hence, $\omega = 0.31$ eV) and the sine-squared envelope ($M = 1$). In addition, the peak intensity of the pulse is defined by the parameter $\eta = 0.005$ which corresponds to the peak intensity $I_{\max} = 1.76 \times 10^{12}$ W/cm². While the solid blue line represents field for $\chi = 0$, the dashed red line is for $\chi = \pi/2$.

Having specified the laser field for our numerical analysis, we shall proceed now with presenting the directional energy distributions of emitted LARA radiation.

2.3 Numerical illustrations

2.3.1 Energy distributions of LARA radiation

Fig. 2.2 demonstrates the energy distributions of photons emitted in the interaction of a hydrogen atom with a coherent electron wave packet under the action of a laser pulse. We use a two-cycle, sine-squared laser pulse, that is presented in Fig. 2.1 as a solid blue line. The pulse is linearly polarised along the x -axis, $\varepsilon = e_x$. The kinetic energy corresponding to the central momentum of the electron wave packet in Eq. (2.63) is $E_p = \frac{p^2}{2m_e} = 1$ eV. Examining the change in kinetic energy with respect to the electron's central momentum allows us to write that $\Delta E_p = \frac{|p|}{m_e} \Delta|p|$. This relation is useful in evaluating the half-width at half maximum (HWHM) in the electron momentum distribution described in Eq. (2.63). When the electron wave packet interacts with a laser pulse for time τ_p , it is important to minimize the spread of the wave packet. This is achieved when $\Delta E_p \tau_p \ll 1$. For some large value of $\zeta \gg 1$, we can write $\zeta = (\Delta E_p \tau_p)^{-1}$. Consequently, the HWHM of the momentum distribution in Eq. (2.63) is given by $\Delta|p| = m_e / (\zeta |p| \tau_p)$. For our purposes, we choose $\zeta = 10^4$ and set the geometry such that $\mathbf{n}_p = \varepsilon_{\mathbf{K}} = e_x$ and $\mathbf{n}_{\mathbf{K}} = c\mathbf{K}/\omega_{\mathbf{K}} = e_z$. This means that the direction of the central momentum of the electron wave packet and emitted photons in the LARA process are perpendicular ($\mathbf{p} \cdot \mathbf{K} = 0$). This configuration maximizes the emission of LARA photons.

For the given geometry, we calculate the energy distribution of emitted photons using either Eq. (2.57) (blue line) or a simplified theorem based on Eq. (2.62) (red line). The upper panel of Fig. 2.2 displays the energy distribution of LARA in a logarithmic scale, and the lower panel displays it in a linear scale. Each panel shows the difference between the energy spectra of emitted radiation of the simplified theorem (2.62) and the complete formalism (2.57). The difference is noticeable in the high-energy portion of the distribution in the upper panel, where the simplified theory shows an extended plateau, while the complete theory shows a clear cut-off of the energy distribution. The extended unphysical plateau in the energy distribution of the simplified theory is an artifact stemming from the Gibbs effect that occurs in band-limited Fourier analysis [62, 63]. The lower panel displays the enlarged portion of the energy distribution where, again, the Gibbs phenomenon is responsible for the artificial oscillations. Another notable difference between our complete theory, as described by Eq. (2.57), and the simplified

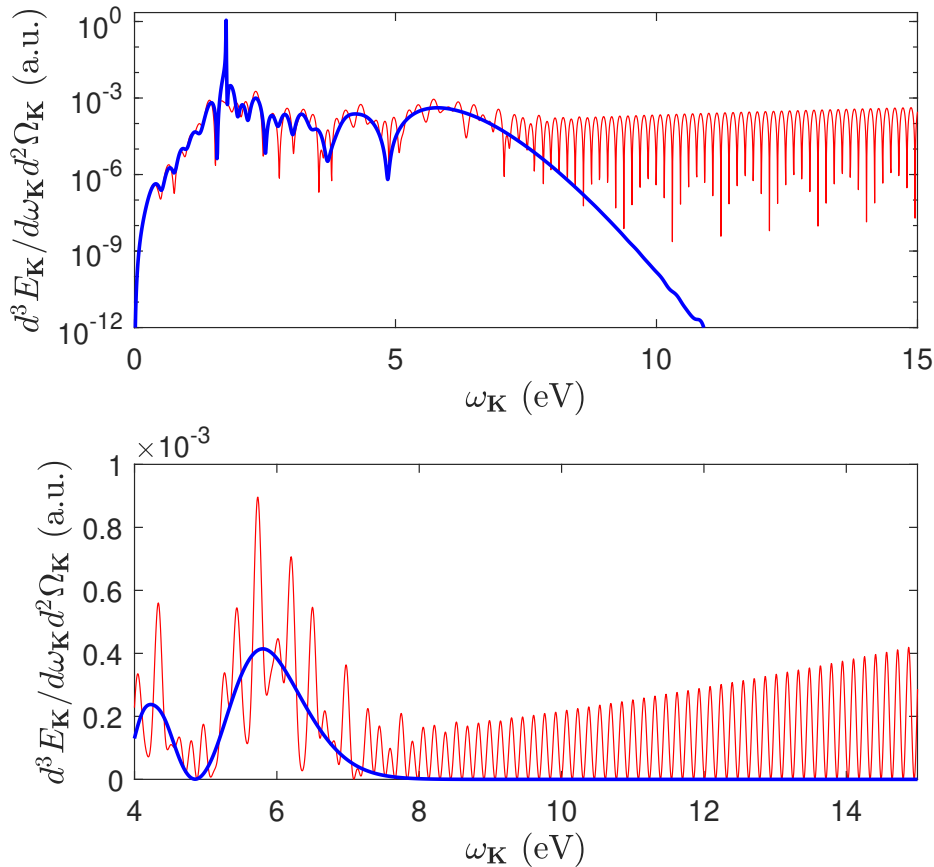


FIGURE 2.2: The energy spectra of emitted photons by recombination of an electron and a hydrogen atom in the presence of a laser field. The laser pulse is used ($N_{\text{rep}} = 1$, $N_{\text{osc}} = 2$) with $\lambda = 4000$ nm ($\omega = 0.31$ eV) and the sine-squared envelope ($M = 1$) having $\eta = 0.005$ ($I_{\text{max}} = 1.76 \times 10^{12}$ W/cm²), as illustrated in Fig. 2.1 for $\chi = 0$. It is linearly polarised along the x -axis, $\varepsilon = e_x$. The kinetic energy associated with the central momentum of the electron wave packet is $E_p = \frac{p^2}{2m_e} = 1$ eV. The wave packet's well-collimated momentum profile, given by Eq. (2.63), has a longitudinal spread $\Delta|p| = m_e / (\zeta|\mathbf{p}|\tau_p)$, where $\zeta = 10^4$. We assume that the LARA radiation propagates in the z -direction, $\mathbf{n}_K = e_z$, whereas the initial electron in the x -direction, $\mathbf{n}_p = e_x$. Moreover, $\varepsilon_K = e_x$. Hence, $\mathbf{p} \cdot \mathbf{K} = 0$ but $\varepsilon_K \cdot \mathbf{p} \neq 0$. The thick blue curve corresponds to Eq. (2.57), and the thin red curve corresponds to the simplified LARA theory introduced in Section 2.2.3. The upper panel displays the data in the logarithmic scale, while the lower panel shows the high-energy portion of the spectra in the linear scale.

theory presented in Section 2.2.3 is the presence of a characteristic peak in the energy distribution at the laser-field-free energy, as given by Eq. (2.44). Despite these discrepancies, the overall behavior of both distributions is similar.

In Fig. 2.3, we present the results for $E_p = 30$ eV, with the remaining parameters being the same as in Fig. 2.2. The upper panel shows the energy spectra of emitted photons in the LARA process according to both the simplified theory, as described by Eq. (2.61) (red curve), and the complete theory, as described by Eq. (2.57) (blue curve). Similar to the results shown in Fig. 2.2, the radiation spectrum (red curve) in Fig. 2.3 exhibit artificial wiggles followed by high-energy oscillations that extend far beyond the actual range of emitted photons. On the other hand, the radiation spectrum (blue curve) has sharp cutoffs on both ends, in addition to the laser-field-free peak at roughly 30 eV.

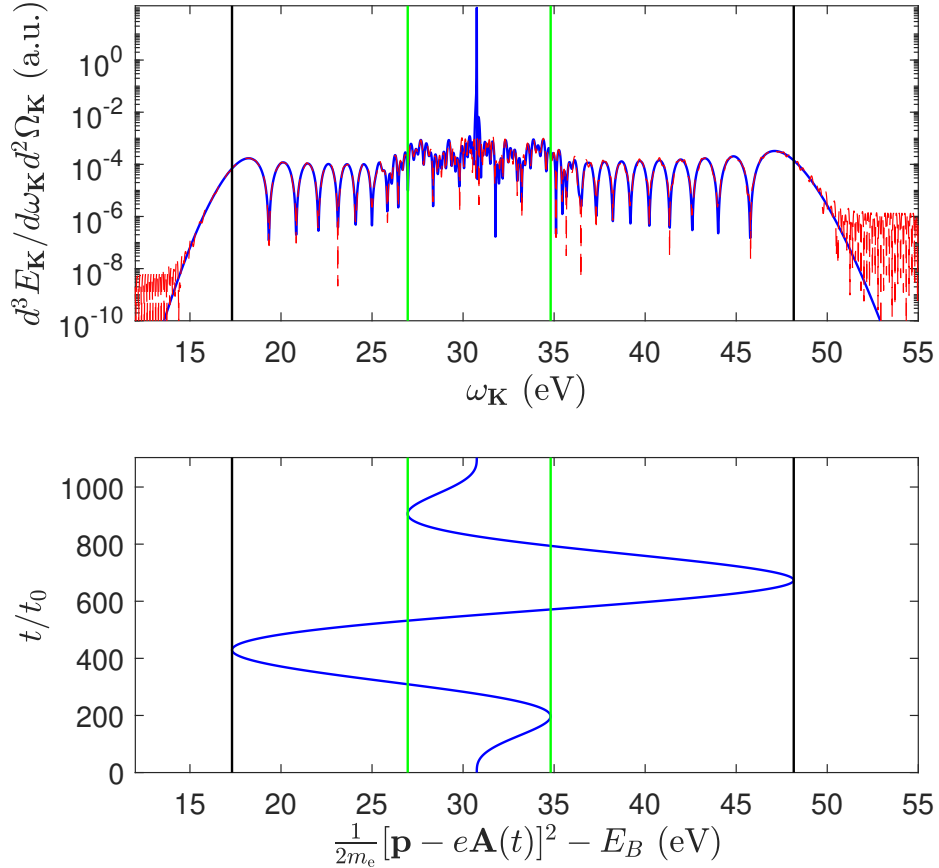


FIGURE 2.3: The upper panel shows the energy spectra of the emitted radiation for the laser field parameters: $N_{\text{rep}} = 1$, $N_{\text{osc}} = 2$, with $\lambda = 4000$ nm ($\omega = 0.31$ eV), $M = 1$ and $\eta = 0.005$ ($I_{\text{max}} = 1.76 \times 10^{12}$ W/cm²), as illustrated in Fig. 2.1 for $\chi = 0$. The laser pulse polarisation vector equals $\varepsilon = e_x$. Here, the kinetic energy associated with the central momentum of the electron wave packet is $E_p = \frac{p^2}{2m_e} = 30$ eV with $\Delta|p| = m_e/(\zeta|p|\tau_p)$, where $\zeta = 10^4$. We assume that the LARA radiation propagates in the z -direction, $\mathbf{n}_K = e_z$, whereas the initial electron in the x -direction, $\mathbf{n}_p = e_x$. Moreover, $\varepsilon_K = e_x$. Hence, $\mathbf{p} \cdot \mathbf{K} = 0$ but $\varepsilon_K \cdot \mathbf{p} \neq 0$. The thick blue curve here corresponds to Eq. (2.57) and the thin red curve corresponds to simplified LARA theory, as introduced in Section 2.2.3. The vertical black lines mark the irradiated energy cutoffs. Moreover, the vertical green lines divide the regions of regular and irregular oscillations. The nature of oscillations in the upper panel can be explained with the help of the lower panel, which shows the time-dependence of the temporal energy irradiated by a moving electron in a laser field, that is captured by the atom, Eq. (2.81).

To describe the oscillations in the energy spectrum of emitted photons, we need to revisit the expression for transition amplitude, given by Eq. (2.35). The second and third term of Eq. (2.35) involve an integral, which can be written as

$$\mathcal{I} = \int_0^{T_p} dt G(t) e^{iS(t)}, \quad (2.79)$$

where $S(t) = Qt + H(t)$ is a rapidly varying function of time. Writing this phase explicitly, we

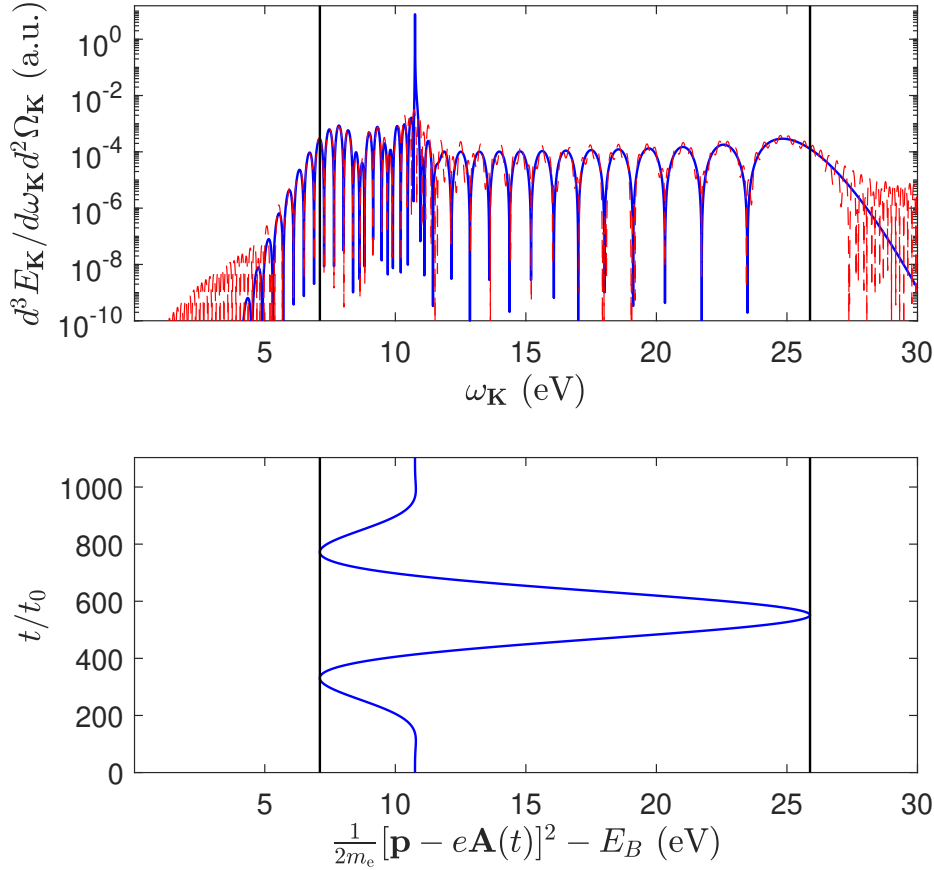


FIGURE 2.4: The same as in Fig. 2.3 but for $\chi = \frac{\pi}{2}$ and $M = 2$. In addition, the central kinetic energy of the electron wave packet equals $E_p = 10$ eV.

have

$$\begin{aligned}
 S(t) &= (E_B + \omega_K - \frac{\mathbf{p}^2}{2m_e})t + \int_0^t dt \left[\frac{e}{m_e} \mathbf{p} \cdot \mathbf{A}(\tau) - \frac{e^2}{2m_e} \mathbf{A}^2(\tau) \right] \\
 &= (E_B + \omega_K)t - \frac{1}{2m_e} \int_0^t dt [\mathbf{p} - e\mathbf{A}(\tau)]^2.
 \end{aligned} \tag{2.80}$$

As it follows from the stationary phase method, the biggest contribution to the integral (2.79) comes from the stationary points defined such that $\partial_t S(t) = 0$. This condition leads to

$$\omega_K(t) = \frac{1}{2m_e} [\mathbf{p} - e\mathbf{A}(t)]^2 - E_B, \tag{2.81}$$

which represents the most probable energy emitted in the process. At the same time, it turns out to be the classical electron energy radiated by a moving electron with momentum \mathbf{p} in the presence of a laser pulse, when it is captured by the atom at time t [36, 57, 58]. Notably, the range of the emitted radiation spectra in Fig. 2.3 coincides well with the range of $\omega_K(t)$ marked by the black vertical lines in both panels. As one can see in the lower panel, the radiation of same energy can be emitted at different times. This will reflect as an interference pattern in the energy spectrum. In the upper panel of Fig. 2.3, the vertical green lines set apart the regions of regular and irregular oscillations in the energy spectrum. The difference in the pattern of

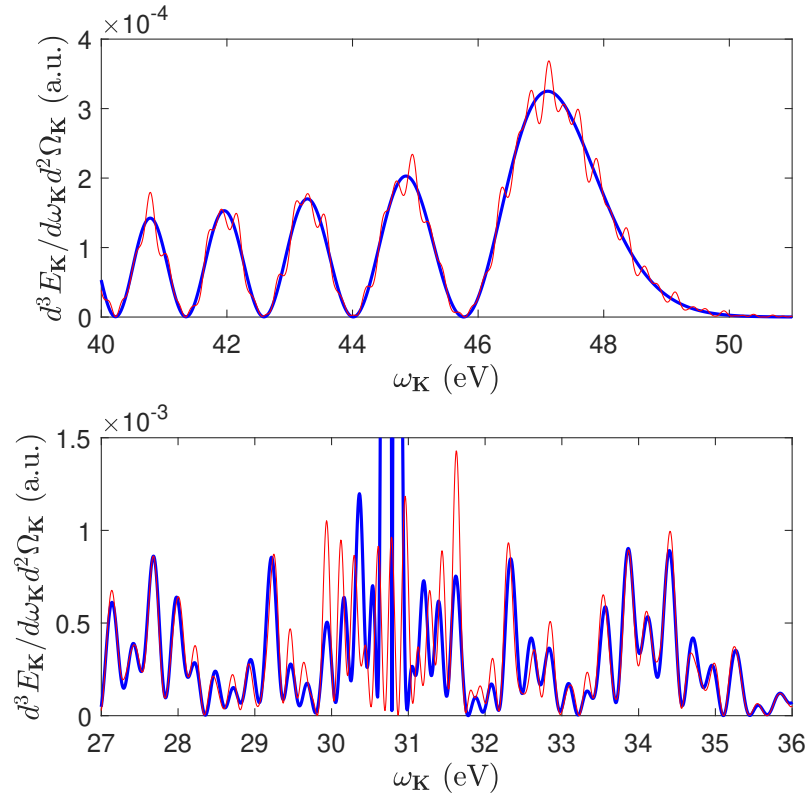


FIGURE 2.5: The enlarged portions of the spectra shown in Fig. 2.3 in the linear scale.

oscillations is a direct manifestation of interference between multiple LARA probability amplitudes having same photon energy emitted at different times. In Fig. 2.3, the first and third regions in the upper panel exhibit very steady oscillations as a result of interference between only two probability amplitudes. In this case, the given photon energy is taking the same value at two different times as shown in lower panel. The relatively erratic behavior of the radiation spectrum is due to the interference of four probability amplitudes at energies corresponding to the central region in the lower panel. We observe the same qualitative behavior in the energy spectra of LARR for other parameters, as presented in Fig. 2.4. In Fig. 2.5, we show the portions of the spectrum presented in the upper panel of Fig. 2.3 (in the linear scale) to emphasize that the additional oscillations arising from the simplified theory are absent in our complete theory.

In order to emphasize a universal character of our results, in Fig. 2.6 we show the energy distributions of LARA radiation arising from the interaction of a coherent electron wave packet with a hydrogen atom assisted by a CO₂ laser pulse ($N_{\text{rep}} = 1$). More specifically, we consider a two-cycle CO₂ laser field ($\lambda \approx 10.6 \mu\text{m}$, $\omega = 0.117 \text{ eV}$) with the sine-squared envelope such that the intensity parameter equals $\eta = 0.0008$ ($I_{\text{max}} = 4.5 \times 10^{10} \text{ W/cm}^2$). We choose the geometry such that $\boldsymbol{\varepsilon} = \boldsymbol{\varepsilon}_{\mathbf{K}} = \mathbf{n}_p = \mathbf{e}_x$ whereas $\mathbf{n}_{\mathbf{K}} = \mathbf{e}_z$. Panels (a) and (c) of Fig. 2.6 compare the energy distributions of emitted radiation according to the complete theory [Eq. (2.57)] (blue line) and the simplified one based on Eq. (2.61) (red line) for $\chi = 0$ and $\chi = \pi/2$, respectively. The red line exhibits unphysical wiggles that exceed the existing range of emitted radiation. These artifacts stem from the Gibbs effect, as discussed previously for the 4000 nm laser field. The energy distribution calculated based on Eq. (2.57), however, exhibits a characteristic peak at the laser-field-free energy given by Eq. (2.44). Moreover, the pattern and oscillations in the energy spectrum are also affected by the CEP in both theories. This demonstrates that

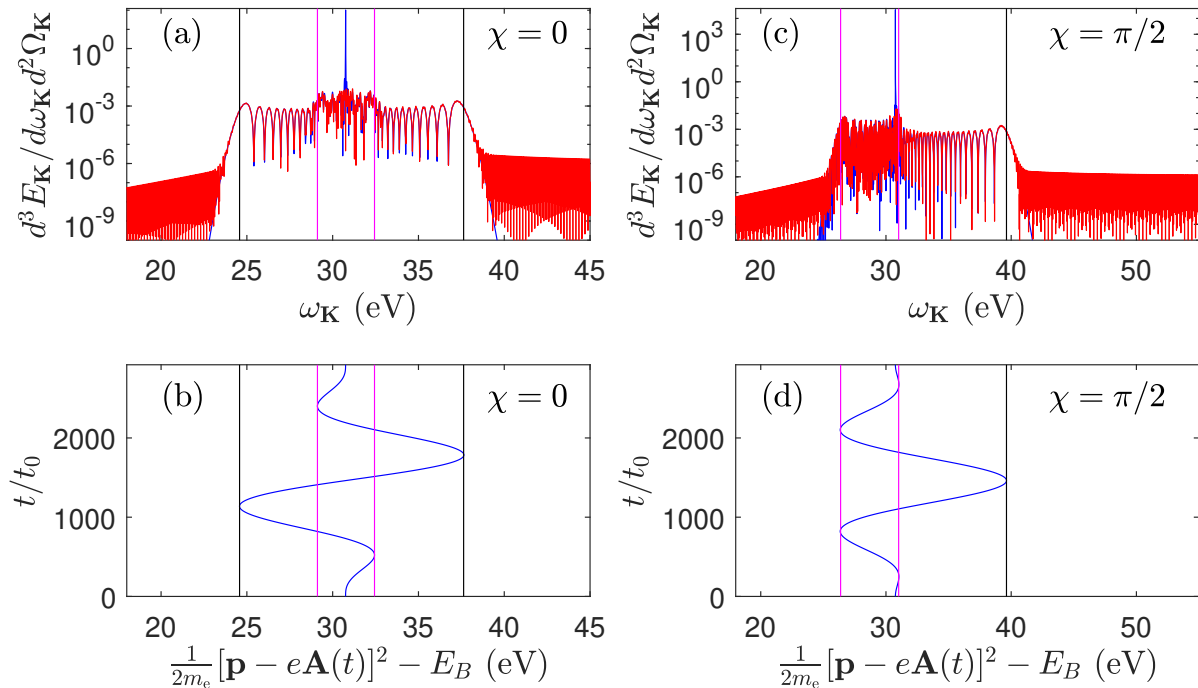


FIGURE 2.6: The upper panels show the energy spectra of LARA radiation ejected by an electron evolving in a two-cycle ($N_{\text{osc}} = 2$) linearly polarised CO_2 laser pulse and being captured by a hydrogen atom. The laser pulse is having wavelength $\lambda \approx 10.6 \mu\text{m}$ ($\omega = 0.117 \text{ eV}$), a sine-squared envelope ($M = 1$), and the peak intensity $I_{\text{max}} = 4.5 \times 10^{10} \text{ W/cm}^2$ ($\eta = 0.0008$). The wave packet centred at momentum \mathbf{p} describes the electron wave packet such that $E_p = \frac{p^2}{2m_e} = 30 \text{ eV}$. The momentum profile of the wave packet (2.63) is well collimated, with the longitudinal spread $\Delta|\mathbf{p}| = m_e / (\zeta|\mathbf{p}|\tau_p)$, where $\zeta = 10^4$. The geometry is such that $\mathbf{p} \cdot \mathbf{K} = 0$ and $\boldsymbol{\varepsilon}_{\mathbf{K}} \cdot \mathbf{p} \neq 0$. The blue line in panels (a) and (c) corresponds to the complete LARA theory [Eq. (2.57)], whereas the thin red line follows from the simplified LARA theory, introduced in Section 2.2.3. The oscillations in the central regions of panels (a) and (c) can be explained by the corresponding lower panels (b) and (d), where we plot the time-dependence of $\omega_{\mathbf{K}}(t)$ [Eq. (2.81)]. Each panel also indicates the corresponding carrier-envelope phase.

the CEP can be used to control the plateau of the LARA radiation spectrum. The temporal energy of emitted radiation, Eq. (2.81), plotted in the lower panel of Fig. 2.6 helps to interpret the radiation spectrum of LARA. Similar to the explanation provided for the 4000 nm laser pulse, a very comparable explanation applies here. Specifically, the energy distributions in panel (a) and (c) have region of regular (the area between the pink and black vertical lines) and irregular oscillations (the area between the vertical pink lines), which originate from the interference of number of LARA probability amplitudes in corresponding regions of panels (b) and (d). Next in Fig. 2.7, we plot the energy spectra of emitted photons in the LARA process, keeping all parameters the same as in Fig. 2.6 for $\chi = 0$, except that now $\boldsymbol{\varepsilon}_{\mathbf{K}} \cdot \mathbf{p} = 0$, i.e., the polarisation direction of LARA photons is perpendicular to the central momentum of electron wave packet. More specifically, we keep $\boldsymbol{\varepsilon} = \boldsymbol{\varepsilon}_{\mathbf{K}} = \mathbf{e}_x$, $\mathbf{n}_{\mathbf{p}} = \mathbf{e}_y$ and $\mathbf{n}_{\mathbf{K}} = \mathbf{e}_z$. We observe that there is no laser-field-free peak in the energy spectrum of the emitted radiation, in agreement with Eq. (2.35). Moreover, the plateau of the energy spectrum is much narrower as compared to Fig. 2.6. Also, the magnitude of the energy spectrum in Fig. 2.7 is smaller by an order of magnitude than in Fig. 2.6. This, in fact, is the least promising configuration for LARA generation when assisted by laser pulses. Also, for this specific geometry, the energy spectra of LARA corresponding to both formulations discussed in Section 2.2.2 and Section 2.2.3 coincide

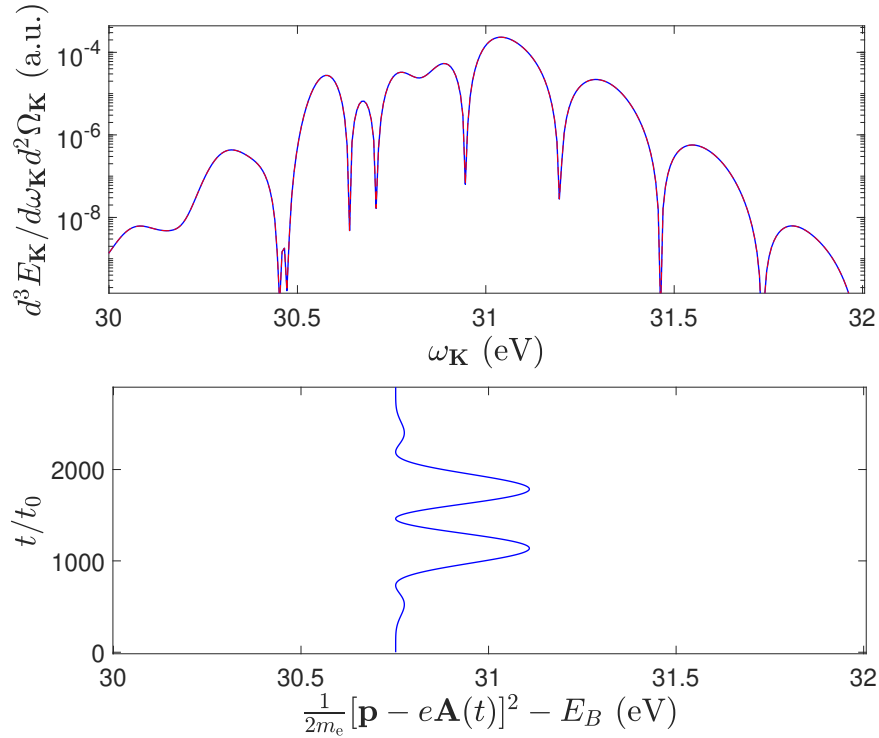


FIGURE 2.7: The same as in Fig. 2.6 for $\chi = 0$, except that now $\varepsilon_{\mathbf{K}} \cdot \mathbf{p} = 0$. In this case, the blue and red lines in the upper panel are identical. Note also the lack of the laser-field-free peak. Both features follow from the formulas; see, for instance, Eq. (2.35) for $\varepsilon_{\mathbf{K}} \cdot \mathbf{p} = 0$.

with each other as seen in Fig. 2.7.

In this Section, we demonstrated the results for LARA assisted by an isolated laser pulse. We also noticed that similar characteristics are visible in the results obtained for different laser parameters; thus showing their universal character. In the following Section, it will be interesting to see how the train of laser pulses affects the energy spectrum of emitted photons.

2.3.2 Frequency combs

In this Section, we will explore the impact of a train of pulses on the LARA energy spectrum. Specifically, we will compare the energy spectra resulting from the impact of one, two, and three identical laser pulses, each of them demonstrated in Fig. 2.1 for $\chi = 0$. We assume that the LARA radiation propagates in the z -direction, $\mathbf{n}_{\mathbf{K}} = \mathbf{e}_z$, whereas the initial electron in the x -direction, $\mathbf{n}_{\mathbf{p}} = \mathbf{e}_x$. Moreover, the polarisation of the laser field and the radiation photon are the same, $\varepsilon = \varepsilon_{\mathbf{K}} = \mathbf{e}_x$. Hence, $\mathbf{p} \cdot \mathbf{K} = 0$ but $\varepsilon_{\mathbf{K}} \cdot \mathbf{p} \neq 0$. The energy spectrum of LARA induced by a pulse train exhibits an elongated plateau with sharp cutoffs, similar to that shown in Fig. 2.3. Additionally, a delta-like peak is present in the spectrum, similar to the case of an isolated pulse. To highlight the differences between the energy spectra calculated for different pulse trains, in Fig. 2.8 we plot magnified portions of the scaled energy distributions [Eq. (2.57)], divided by N_{rep}^2 . The energy distribution for an isolated pulse ($N_{\text{rep}} = 1$) is represented by the black line and serves as an envelope for the other two distributions. The dashed blue line represents the energy spectrum resulting from two pulses ($N_{\text{rep}} = 2$), while the solid red line corresponds to three pulses ($N_{\text{rep}} = 3$). Notably, when the LARA process is accompanied by a train of pulses ($N_{\text{rep}} > 1$), the energy distributions of radiated

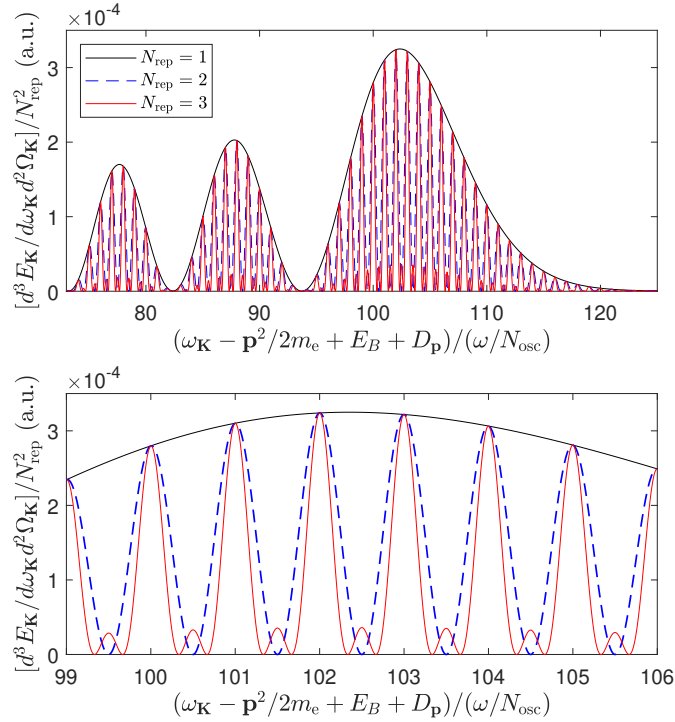


FIGURE 2.8: Energy spectrum of the LARA radiation emitted in the presence of an isolated pulse ($N_{\text{rep}} = 1$, solid black curve) that is represented in Fig 2.1 for $\chi = 0$, and compared to a train of two ($N_{\text{rep}} = 2$, dashed blue curve) and three ($N_{\text{rep}} = 3$, solid red curve) such pulses. The remaining parameters are the same as in Fig. 2.3. The spectra have been divided by N_{rep}^2 . The bottom panel shows the magnified portions of the scaled energy distributions. While for a single pulse there is no frequency comb, they appear for LARA accompanied by a train of pulses.

photons display comb-like structures, with characteristic N_{rep}^2 scaling. Our second example concerns the CO_2 laser field with parameters $10.6 \mu\text{m}$ ($\omega = 0.117 \text{ eV}$), $M = 1$ and $\eta = 0.0008$ ($I_{\text{max}} = 4.5 \times 10^{10} \text{ W/cm}^2$), and the same electron and laser field configuration. Hence, we observe the exact same behaviour of energy spectrum with increasing N_{rep} , as demonstrated in Fig. 2.9. This general behavior can be explained by the following derivation, where we neglect the contribution from the laser-field-free process.

Consider the probability amplitude of a recombination process assisted by the train of N_{rep} identical laser pulses of duration τ_p each. Omitting the laser-field-free contribution in Eq. (2.35) that is represented there by the delta function, the probability amplitude can be written as

$$\mathcal{A}_{N_{\text{rep}}}(\mathbf{p}) = \int_0^{N_{\text{rep}}\tau_p} dt G(t) e^{iQt + iH(t)}, \quad (2.82)$$

where Q and $H(t)$ are defined by Eqs. (2.17) and (2.18), respectively, whereas

$$G(t) = \frac{F(t)}{[\kappa^2 + \pi^2(t)]^2} - \frac{\boldsymbol{\varepsilon}_{\mathbf{K}} \cdot e\mathbf{A}(t)}{[\kappa^2 + \pi^2(t)]^2}, \quad (2.83)$$

which follows from Eq. (2.35). Note that in our model of the laser field, it holds that $\int_{-\infty}^{\infty} dt \mathcal{E}(t) = 0$, as $A(0) = A(\tau_p) = 0$. The same condition retains for identical pulse train [Eq. (2.76)], as $A(\ell\tau_p) = 0$ for $\ell = 0, 1, \dots, N_{\text{rep}}$. Keeping this in mind, we conclude that $G(0) = G(\tau_p) = 0$.

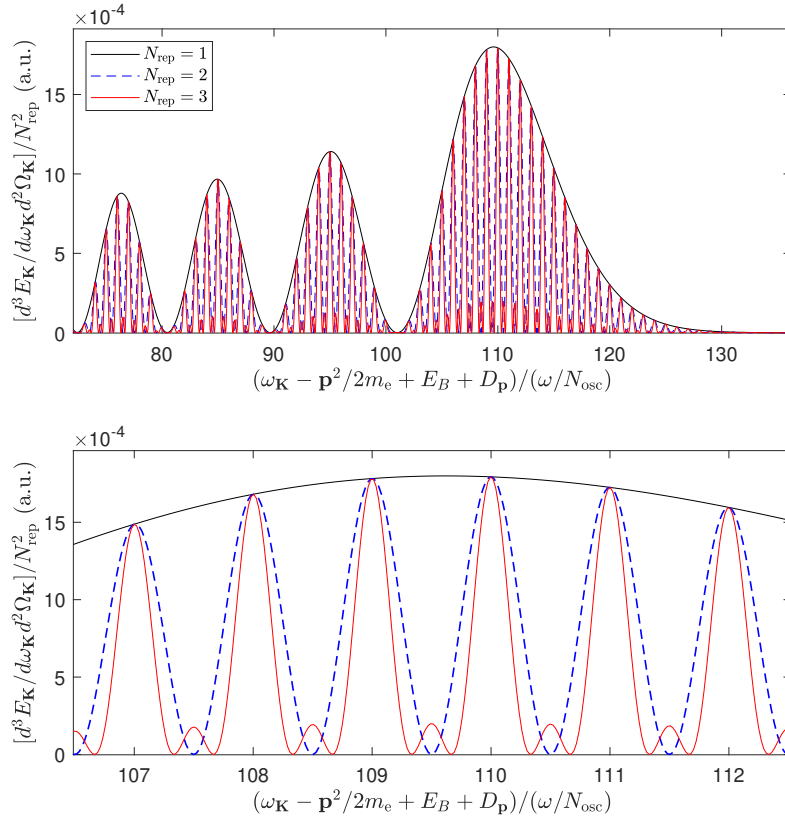


FIGURE 2.9: Same as in Fig. 2.8 but for CO₂ laser. The parameters are specified in Fig. 2.6, with $\chi = 0$.

Moreover, the function $G(t)$ and the integrand defining $H(t)$, i.e., $h(t)$ given by Eq. (2.19), are periodic within the time duration of a train $N_{\text{rep}}\tau_p$. On the contrary, $H(t)$ does not change repeatedly over the duration of the train. What is changing repeatedly is in turn,

$$H_{\text{osc}}(t) = \int_0^t d\tau [h(\tau) - D_{\mathbf{p}}], \quad (2.84)$$

where

$$D_{\mathbf{p}} = \frac{1}{\tau_p} \int_0^{\tau_p} d\tau h(\tau) = \frac{H(\tau_p)}{\tau_p}. \quad (2.85)$$

It also fulfills the condition,

$$H_{\text{osc}}(0) = H_{\text{osc}}(\tau_p) = 0. \quad (2.86)$$

Taking these facts into account, we rewrite Eq. (2.82) such that

$$\mathcal{A}_{N_{\text{rep}}}(\mathbf{p}) = \int_0^{N_{\text{rep}}\tau_p} dt G(t) e^{i(Q+D_{\mathbf{p}})t + iH_{\text{osc}}(t)}. \quad (2.87)$$

Next, we split this integral into the sum of integrals over the time duration of a single pulse from the train,

$$\mathcal{A}_{N_{\text{rep}}}(\mathbf{p}) = \sum_{K=1}^{N_{\text{rep}}} \int_{(K-1)\tau_p}^{K\tau_p} dt G(t) e^{i(Q+D_{\mathbf{p}})t + iH_{\text{osc}}(t)}. \quad (2.88)$$

By changing the integration variable in each of those integrals to $t' = t - (K - 1)\tau_p$, we obtain

$$\mathcal{A}_{N_{\text{rep}}}(\mathbf{p}) = \sum_{K=1}^{N_{\text{rep}}} \int_0^{\tau_p} dt' G(t') e^{i(Q+D_{\mathbf{p}})(t'+(K-1)\tau_p)+iH_{\text{osc}}(t')}. \quad (2.89)$$

Recognizing here the probability amplitude of LARA by a single pulse $\mathcal{A}_1(\mathbf{p})$ [see, Eq. (2.87) for $N_{\text{rep}}=1$], we rewrite Eq. (2.89) as

$$\mathcal{A}_{N_{\text{rep}}}(\mathbf{p}) = \mathcal{A}_1(\mathbf{p}) \sum_{K=1}^{N_{\text{rep}}} e^{i(K-1)(Q+D_{\mathbf{p}})\tau_p}. \quad (2.90)$$

Summing up the above geometric series leads to

$$\mathcal{A}_{N_{\text{rep}}}(\mathbf{p}) = e^{\frac{i}{2}(Q+D_{\mathbf{p}})(N_{\text{rep}}-1)\tau_p} \mathcal{A}_1(\mathbf{p}) \frac{\sin[\frac{1}{2}(Q+D_{\mathbf{p}})N_{\text{rep}}\tau_p]}{\sin[\frac{1}{2}(Q+D_{\mathbf{p}})\tau_p]}. \quad (2.91)$$

It follows from this formula that the probability amplitude of radiative attachment in the presence of a train of pulses is proportional to the one for a single pulse. As one can see, it is modulated by an interference term that is expressed by sine functions. Here, $e^{\frac{i}{2}(Q+D_{\mathbf{p}})(N_{\text{rep}}-1)\tau_p}$ is an overall phase factor. One sees from Eq. (2.91) that the probability amplitude $\mathcal{A}_{N_{\text{rep}}}(\mathbf{p})$ has the maximum values when the sine function in the denominator is zero, which happens when

$$\frac{1}{2}(Q+D_{\mathbf{p}})\tau_p = \pi N, \quad N \in \mathbb{Z}. \quad (2.92)$$

Plugging here the expression for Q [Eq. (2.17)] and for $\tau_p = \frac{2\pi}{\omega} N_{\text{osc}}$, we obtain

$$\left(\omega_K - \frac{\mathbf{p}^2}{2m_e} + E_B + D_{\mathbf{p}}\right) \frac{N_{\text{osc}}}{\omega} = N, \quad N \in \mathbb{Z}. \quad (2.93)$$

The above equation can be solved for the values of ω_K . At those ω_K , the interference factor defined by the sine functions equals N_{rep} . Hence, the energy distribution gets enhanced by a factor of N_{rep}^2 as compared to the one for a single pulse. This can be attributed to constructive interference of probability amplitudes of LARA accompanied by each pulse from the train. There is also $(N_{\text{rep}} - 2)$ of secondary maxima for $N_{\text{rep}} \geq 2$ and $(N_{\text{rep}} - 1)$ of zeros of the energy distribution between two subsequent major peaks, as shown in Figs. 2.8 and 2.9. One can also examine that those major peaks become narrower with increasing N_{rep} , by a factor of N_{rep} . Hence, the total energy of the emitted radiation scales like N_{rep} , whereas the LARA spectrum becomes similar to the Dirac comb with increasing N_{rep} .

In this Section, we have shown that the coherent frequency combs can be generated in radiative attachment when accompanied by a train of identical laser pulses. For the parameters considered, we have demonstrated the frequency comb in extreme ultraviolet regime. While the plateau in the energy spectrum of LARA can be extended by increasing the energy of the initial electron wave packet, this would also facilitate the generation of more energetic frequency combs.

2.3.3 Energy distribution spectrograms

In this Section, we shall perform a time-frequency analysis of energy distributions of LARA radiation. This will be done by means of a spectrogram, $S(t, \omega_{\mathbf{K}})$, that is closely related to the short-time Fourier transform [69]. In Appendix A.2 we present general definitions and properties of spectrograms. Here, we adapt this tool to visualize when in time the given LARA radiation is emitted. Since the respective energy distributions will be analyzed, in what follows we refer to them as signals.

In general, for a given signal $\mathcal{A}(\omega)$ that is defined for frequencies ω within the range $\omega_1 \leq \omega \leq \omega_2$, we truncate it first with the cutoff function,

$$f_T(x, \Delta x) = \begin{cases} 0 & \text{for } x \leq 0 \\ \sin^2\left(\frac{\pi x}{2\Delta x}\right) & \text{for } 0 < x < \Delta x \\ 1 & \text{for } \Delta x \leq x \leq 1 - \Delta x \\ \sin^2\left(\frac{\pi(1-x)}{2\Delta x}\right) & \text{for } 1 - \Delta x < x < 1 \\ 0 & \text{for } x \geq 1, \end{cases} \quad (2.94)$$

such that

$$\mathcal{A}_T(\omega) = \mathcal{A}(\omega) f_T\left(\frac{\omega - \omega_1}{\omega_2 - \omega_1}, \xi_T(\omega_2 - \omega_1)\right) \quad (2.95)$$

is a truncated signal. Here ξ_T is a small parameter. Then, the short-time Fourier transform of the truncated signal is [69]

$$\mathcal{A}_{ST}(t, \omega_{\mathbf{K}}) = \int_{\omega_1}^{\omega_2} d\omega \mathcal{A}_T(\omega) W(\omega - \omega_{\mathbf{K}}, \xi_W(\omega_2 - \omega_1)) e^{-i\omega t}, \quad (2.96)$$

where a parameter ξ_W specifies the width of the window function $W(x, \Delta x)$. Now, choosing the Gaussian window,

$$W(x, \Delta x) = \frac{e^{-(x/\Delta x)^2}}{\sqrt{\pi}\Delta x}, \quad (2.97)$$

with

$$\int_{-\infty}^{\infty} dx W(x, \Delta x) = 1, \quad (2.98)$$

we define the time-frequency spectrogram as

$$S(t, \omega_{\mathbf{K}}) = |\mathcal{A}_{ST}(t, \omega_{\mathbf{K}})|^2. \quad (2.99)$$

Here, we need to comment on calculating the Fourier transform in Eq. (2.96). In order to avoid Gibbs effect, the integrand in Eq. (2.96) has to be continuous and take the same values at the boundaries. For this reason, we have truncated the original signal $\mathcal{A}(\omega)$. Another point worth mentioning is that for a truncated signal that is peaked around ω_0 , i.e., $\mathcal{A}_T(\omega) \approx \delta(\omega - \omega_0)$, the spectrogram equals $S(t, \omega_{\mathbf{K}}) \approx |W(\omega_0 - \omega_{\mathbf{K}}, \xi_W(\omega_2 - \omega_1))|^2$. It is, therefore, constant in time which we will use to interpret our results.

In Fig. 2.10, we demonstrate the energy spectra (upper row) and their related spectrograms (lower row). The results demonstrated in the left column are calculated based on the complete theory (Section 2.2.2), while in the right column they correspond to the simplified theory (Section 2.2.3). We consider a two-cycle ($N_{\text{osc}} = 2$), sine-squared ($M = 1$) laser pulse ($N_{\text{rep}} = 1$)

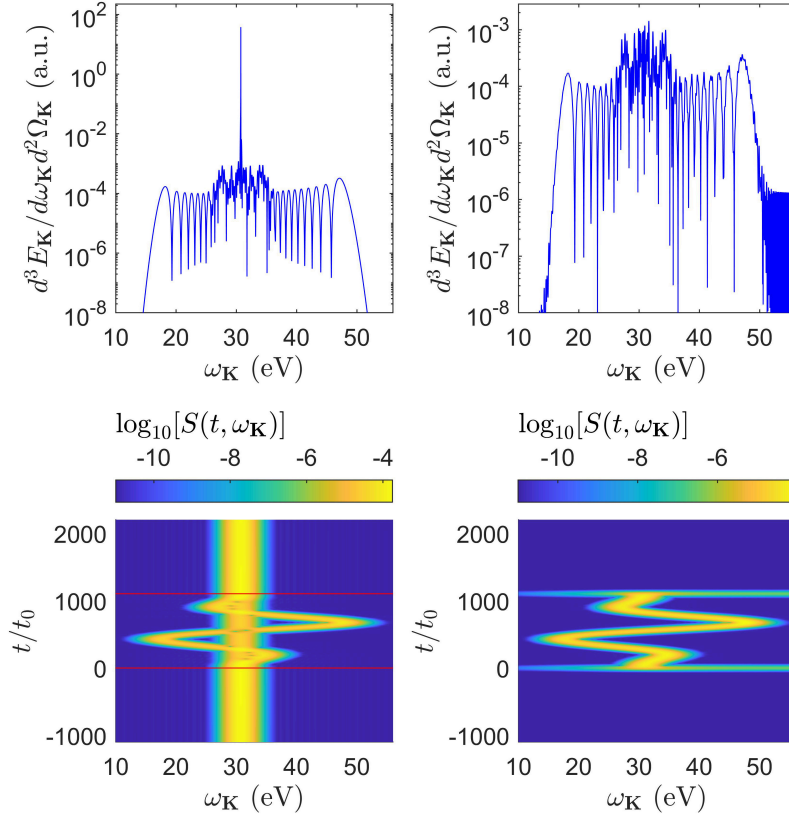


FIGURE 2.10: While the left column shows the energy spectrum and its corresponding spectrogram calculated within the complete theory (Section 2.2.2), the right column is for the simplified theory (Section 2.2.3). The parameters for energy spectra are same as in Fig. 2.3. For spectrograms, we use the Gaussian window (2.97) and the cutoff function (2.94), with the parameters: $\zeta_T = 0.1$, $\zeta_W = 0.03$, $\omega_1 = 1$ eV, and $\omega_2 = 65$ eV. The zigzag yellow line is seen in both spectrograms and it extends for the duration of the laser pulse. The straight vertical yellow line in bottom left panel at roughly 30 eV corresponds to the laser-field-free peak in the spectrum. In the bottom left panel, the red horizontal lines mark the beginning and the end of the laser pulse. In the bottom right panel, the horizontal blue lines are reminiscence of the Gibbs effect.

with parameters $\lambda = 4000$ nm, $\eta = 0.005$ and $\chi = 0$, as defined in Eq. (2.76). The kinetic energy corresponding to the central momentum of the electron wave packet (2.63) is $E_p = \frac{p^2}{2m_e} = 30$ eV and the HWHM is $\Delta|p| = m_e / (\zeta|p|\tau_p)$, where $\zeta = 10^4$. We choose the LARA geometry such that $\varepsilon = \varepsilon_K = n_p = e_x$ and $n_K = c\mathbf{K}/\omega_K = e_z$. We use the cutoff function and the window function with parameters $\zeta_T = 0.1$, $\zeta_W = 0.03$, $\omega_1 = 1$ eV, and $\omega_2 = 65$ eV. In the bottom panel of Fig. 2.10, the two distinct patterns can be observed in the spectrograms corresponding to the respective energy spectrum. At roughly 30 eV, the straight vertical line in the bottom left panel extends beyond the pulse duration $[0, \tau_p]$ and indicates the laser-field-free recombination. This vertical line is absent in the spectrogram in the bottom right panel, as the simplified theory neglects the contribution from the laser-field-free process. Additionally, both spectrograms display a zigzag pattern that lasts for the entire duration of the pulse, signifying recombination in the presence of the laser pulse in both cases. For convenience, the two horizontal red lines mark the pulse duration in the spectrogram at the bottom left panel. Furthermore, the two unphysical blue stripes can be observed in the bottom right panel when the laser field is

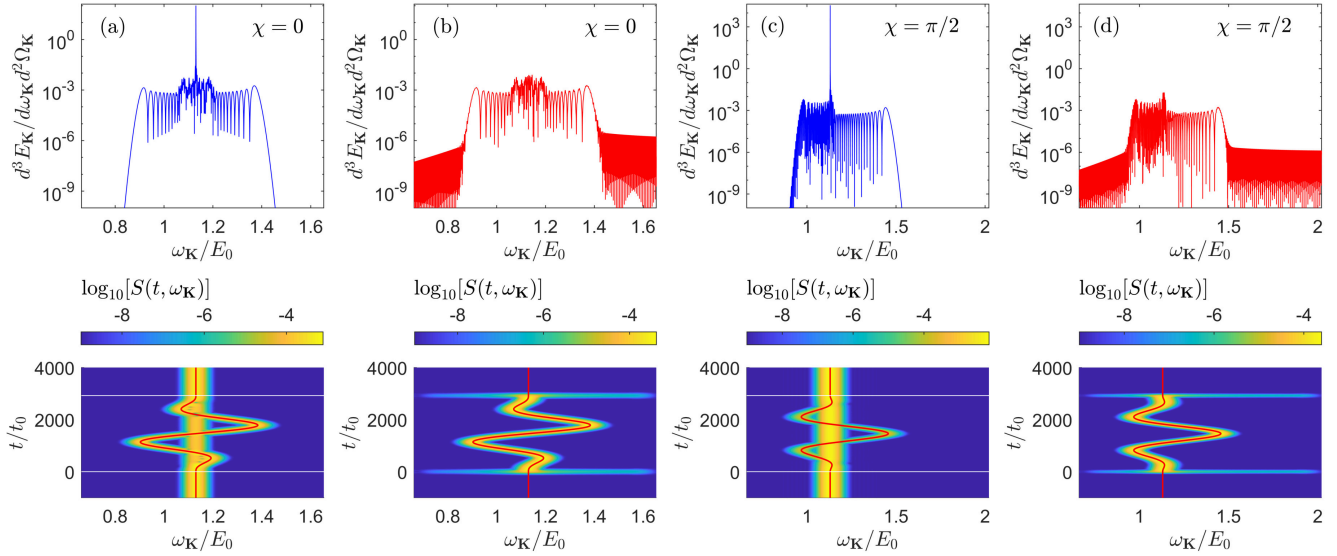


FIGURE 2.11: In the upper row, we demonstrate the energy distributions of emitted radiation presented in Fig. 2.6. The blue curve corresponds to complete theory (2.39), whereas the red curve follows from the simplified LARA theory as introduced in Section 2.2.3. Below we demonstrate their corresponding spectrograms. They have been calculated using the cutoff function and Gaussian window as specified by Eqs. (2.95), (2.94) and (2.96), with the parameters: $\zeta_T = 0.1$, $\zeta_W = 0.03$, $\omega_1 = 1$ eV, and $\omega_2 = 65$ eV. In the spectrogram corresponding to energy spectra (a) and (c), the yellow horizontal lines mark the beginning and the end of the laser pulse. In the spectrogram corresponding to energy spectra (b) and (d), the blue horizontal lines are artifacts originating from the Gibbs effect in the case of the simplified theory. The red line overlapping the zigzag yellow pattern in the spectrograms represents Eq. (2.81).

turned on and off. These are marks of the Gibbs effect in the case of simplified theory (Section 2.2.3). The same is not observed in the bottom left panel that refers to the complete LARA formulation (Section 2.2.2).

A similar time-frequency analysis of the LARA spectrum can be applied to other fields, such as a CO₂ laser field, with the same laser and electron wave packet parameters as shown in Fig. 2.6. Fig. 2.11 presents the energy spectra and their corresponding spectrograms for the cases where $\chi = 0$ and $\chi = \frac{\pi}{2}$, calculated using both the complete theory introduced in Section 2.2.2 (blue line) and the simplified theory from Section 2.2.3 (red line). As with the previous analysis, the spectrogram resulting from the complete theory [panels (a) and (c)] display a vertical yellow line that extends beyond the pulse duration $[0, \tau_p]$ and is roughly at $\omega_K = 1.2$ a.u. (30 eV) for both $\chi = 0$ and $\chi = \frac{\pi}{2}$. This line corresponds to the laser-field-free peak in the energy radiation spectra. In each spectrogram, a characteristic zigzag pattern lasts over the duration of the pulse and it varies with CEP. Interestingly, it overlaps the red line representing the temporal energy emitted by the electron in a laser field, $\omega_K(t)$, given by Eq. (2.81). The latter can be used in laser field metrology, which is discussed next.

2.3.4 LARA-based laser field metrology

In this Section, we propose a method of temporal reconstruction of the laser field which follows from analyzing the spectrogram of LARA radiation. In Fig. 2.12, we present the spectrogram of the energy distribution of LARA radiation generated by the interaction of an electron with a hydrogen atom and an isolated pulse. While the upper panel of Fig. 2.12 is for $\chi = 0$, lower

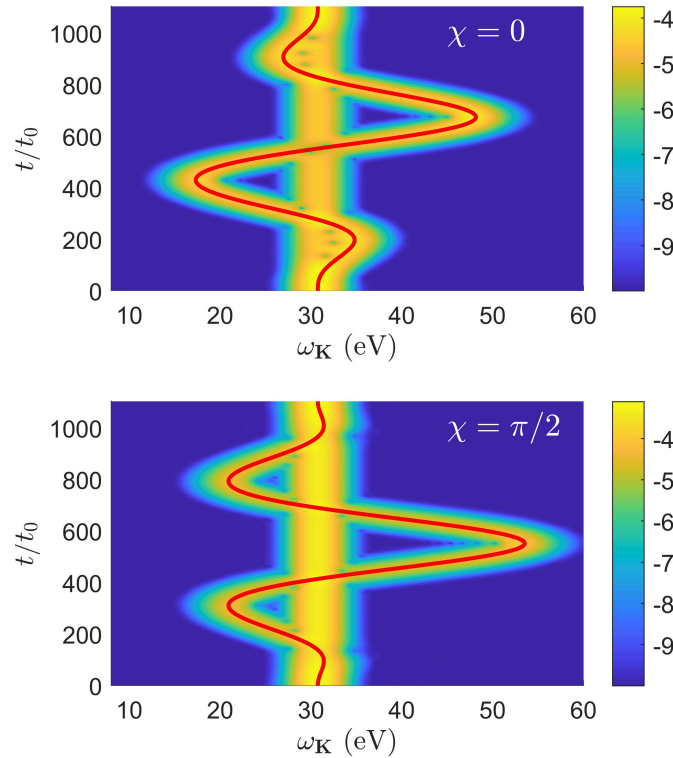


FIGURE 2.12: Spectrograms of the energy distribution (2.57) of LARA radiation generated by the interaction of an electron with a hydrogen atom and an isolated pulse represented in Fig. 2.1, either for $\chi = 0$ (upper panel) or for $\chi = \frac{\pi}{2}$ (lower panel). The remaining parameters are the same as in Fig. 2.10. Again, the straight vertical yellow line in both panels, at roughly 30 eV, corresponds to the laser-field-free peak in the spectrum. Red lines represent the time-dependence of $\omega_K(t)$ given by Eq. (2.81).

panel is for $\chi = \frac{\pi}{2}$. The parameters used for calculations are the same as in Fig. 2.10. Again, one can notice the zigzag pattern lasting for the entire pulse duration. Importantly, it is sensitive to the pulse parameters such as CEP (see, also Fig. 2.11). For this reason, it opens an idea to use this sensitivity for field reconstruction. Specifically, the red line in the spectrograms marks the quantity $\omega_K(t)$ [Eq. (2.81)] which represents the energy emitted by the recombining electron throughout the pulse duration. It is defined in terms of the vector potential of the laser field, the kinetic and the binding energies of the electron. Therefore, by providing the binding energy of the target and the central kinetic energy of the initial electron wave packet, it is possible to reconstruct $\mathbf{A}(t)$ from the spectrogram.

This method can also be applicable for characterisation of a pulse train, in addition to an isolated pulse. In Fig. 2.13, we present the spectrogram of the energy spectrum of LARA radiation with the impact of a train of two laser pulses ($N_{\text{rep}} = 2$). The remaining parameters are the same as in Fig. 2.12 with $\chi = 0$. Similar to the case of an isolated pulse, the laser field is imprinted in the spectrogram. By comparing the zigzag line against the analytic form of $\omega_K(t)$, one can deduce what the temporal characteristics of the pulse train are.

2.4 Summary

In this Chapter, we have formulated a complete theoretical description of laser-assisted electron-atom radiative attachment, which goes beyond the previously established one (see, e.g., Refs. [56,

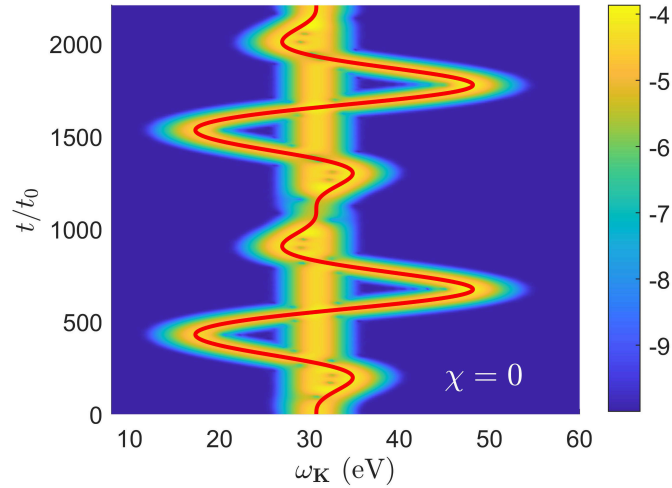


FIGURE 2.13: The same as in Fig. 2.12 but for the pulse train ($N_{\text{rep}} = 2$) and $\chi = 0$.

57, 58, 59, 60, 61]). We have shown various differences between both treatments. Specifically, our approach contains a contribution from a laser-field-free process which manifests as a pronounced peak in the energy distribution of LARA radiation. This is missing in the simplified theory of LARA (Section 2.2.3). In addition, we do not observe unphysical oscillations in the energy spectra of LARA radiation leading to appearance of secondary plateaux, or artificial patterns in the spectrograms; both originating from the forcefully limiting the range of time integral defining the probability amplitude of LARA in Refs. [56, 57, 58, 59, 60, 61]. All these discrepancies have been illustrated by various examples and different sets of parameters, proving a very general character of our results.

We have studied electron attachment in the presence of a single pulse and a train of identical pulses. While in both cases, we have observed an extended plateau region of radiation with an aforementioned δ peak, for a pulse train the LARA spectra exhibit an additional pattern. Namely, a comb-like structure that scales like the number of pulse repetitions squared (N_{rep}^2). This coherent enhancement of energy distributions was attributed to a constructive interference of probability amplitudes of LARA by each pulse from the train. Interestingly, such clear combs have been observed despite a spread of momenta in the initial electron wave packet.

Finally, we have demonstrated a time-frequency analysis of the emitted radiation and its sensitivity to temporal properties of the laser field. Hence, an idea of using LARA spectrogram towards laser-field metrology has been put forward.

In closing this Chapter, we note that by developing a new theoretical framework of treating LARA, we have also established foundation for our further investigation, involving the Coulomb potential as well as nondipole corrections. This is presented next.

Chapter 3

Laser-Assisted Radiative Recombination (LARR)

3.1 Introduction

This Chapter is devoted to laser-assisted radiative recombination beyond the dipole approximation. In other words, we study the recombination of electrons with hydrogen-like positive ions described by the long-range Coulomb potential [36, 38, 41, 49, 50, 55, 59] in the presence of an external laser field which will lead to the emission of high-energy photons. Note that the above references treat the laser field within the dipole approximation. Our theoretical framework extends beyond the dipole approximation such that the external laser field depends on both space and time.

Specifically, due to the recent development of laser technology, a lot of attention is given to nondipole effects in ionisation [81, 82, 83, 84, 86, 87, 88, 89, 90, 91, 92, 93, 94, 95]. However, going beyond the dipole approximation not only applies to ionisation but can also occur wherever there are electron-laser-field interactions, resulting in a radiation pressure effect. The radiation pressure effect occurs when the laser field imparts momentum to the electron. This effect arises from the magnetic component of the electromagnetic field under certain conditions, namely, for high-frequency or low-frequency but high intensity laser fields [96, 97]. Therefore, it is necessary to go beyond the dipole approximation to comprehend the non-linearity that emerges in atomic and molecular processes beyond a certain range of field parameters. Since LARR is a time-reversed process to ionisation and an underlying process in HHG, it is important to study the influence of nondipole corrections on the properties of the LARR spectrum.

The experimental investigations, such as the one referenced in [98, 99], were among the first to identify the presence of nondipole effects in strong-field ionisation. Many theoretical investigations were inspired by these experiments, focusing mainly on ionisation and laser-assisted electron scattering [81, 82, 83, 84, 86, 87, 88, 89, 90, 91, 92, 93, 94, 95, 100] within the strong-field regime. We are not aware, however, of any work, prior to ours [101], that would study nondipole effect in laser-assisted radiative recombination. We came across only one paper [64] that explored LARR beyond the dipole approximation, which was within the relativistic framework. In this study, the external laser field was represented as a circularly polarised plane wave dependent on space and time. Also, the initial state of the highly energetic electron in the presence of a high-intensity and low-frequency field was approximated by the Volkov solution, neglecting the Coulomb effects. This interaction resulted in the emission of gamma rays and introduced a shift in the angular distribution of emitted photons. In our investigation of LARR, along with the nondipole effect, we are considering Coulomb effects on LARR. Additionally, the laser field is assumed to be a short laser pulse rather than a plane wave.

In this Chapter, we develop a systematic study leading to the inclusion of nondipole corrections to the LARR theory. As it will be clear, by comparing different contributions, the recoil effect seems to be most relevant. On top of studying nondipole corrections, which lead to an extension of the LARR plateau, we also investigate the possibility of enhancing particular harmonics. This is done by chirping the assisting laser pulse. It was investigated for HHG [102, 103] but not for LARR. This is a way to control LARR.

This Chapter is structured as follows. In Section 3.2.1, we derive the scattering state of the electron in the presence of an external laser field and a Coulomb interaction using relativistic reduction of the Klein-Gordon equation. In Section 3.2.2, we consider LARR by the impact of the electron wave packet and derive the expression for the probability amplitude of LARR beyond the dipole approximation. Following that, in Section 3.2.3, we derive the expression for the energy distribution of emitted photons resulting from the impact of a coherent electron wave packet. We keep the profile of the electron wave packet as Lorentzian (Section 2.2.4), consistent with Chapter 2. In Section 3.3.1, we first illustrate the laser field model that we use. Henceforth, we demonstrate the nondipole effects in the energy distribution of LARR along with its spectrogram. Subsequently, we demonstrate the nondipole effects in the angular distribution of LARR radiation. In Section 3.3.2, we propose a method to enhance a specific harmonic in the energy distribution by chirping the laser pulse. Additionally, in Section 3.3.3, we demonstrate the vortex structures in LARR. We provide a short summary of this Chapter in Section 3.4.

3.2 Theoretical formulation of LARR

3.2.1 Coulomb-Volkov scattering state with nondipole corrections

In this Section, we present a systematic development of the Coulomb-Volkov scattering state that includes nondipole corrections. We start with the relativistic Klein-Gordon equation describing the electron in a Coulomb potential and a laser field; thus treating electron as a spinless particle. The solution of the Klein-Gordon equation is then expanded in powers of $1/c$ to track the leading nondipole corrections to the Coulomb-Volkov scattering state. This is subsequently used in derivations of the LARR probability amplitude in Section 3.2.2.

Consider an electron that moves with momentum \mathbf{p} in an external laser field and an atomic potential. If treated as spin-0 particle, the electron wave function $\psi_{\mathbf{p}}(\mathbf{r}, t)$ satisfies the so-called Klein-Gordon equation,

$$\left[\frac{1}{c^2} (i\partial_t - V(\mathbf{r}, t))^2 - (\hat{\mathbf{p}} - e\mathbf{A}(\mathbf{r}, t))^2 - (m_e c)^2 \right] \psi_{\mathbf{p}}(\mathbf{r}, t) = 0. \quad (3.1)$$

Here, $\mathbf{A}(\mathbf{r}, t) = \mathbf{A}(t - \frac{\mathbf{n} \cdot \mathbf{r}}{c})$ is the vector potential describing the laser field propagating in the direction \mathbf{n} . Hence, it depends on the retarded time,

$$t_R = t - \frac{\mathbf{n} \cdot \mathbf{r}}{c}. \quad (3.2)$$

Moreover, $V(\mathbf{r}, t)$ represents the scalar potential which, in principle, can depend on time. In what follows, we assume however that $V(\mathbf{r}, t) = V(\mathbf{r}) = -\frac{Ze^2}{4\pi\epsilon_0|\mathbf{r}|}$, as it corresponds to the atomic Coulomb interaction.

We search for solutions of the Klein-Gordon equation (3.1) such that

$$\psi_p(\mathbf{r}, t) = \frac{1}{\sqrt{\mathcal{V}}} e^{iF(\mathbf{r}, t)} \phi_p(\mathbf{r}, t), \quad (3.3)$$

where the phase factor $F(\mathbf{r}, t)$ reflects the dependence on the retarded time, similar to the vector potential $\mathbf{A}(\mathbf{r}, t)$. Here \mathcal{V} is the quantisation volume. Keeping this in mind, one can derive that

$$(i\partial_t - V(\mathbf{r}))^2 \psi_p(\mathbf{r}, t) = e^{iF(\mathbf{r}, t)} (i\partial_t - V(\mathbf{r}) - F'(\mathbf{r}, t))^2 \phi_p(\mathbf{r}, t), \quad (3.4)$$

$$(\hat{\mathbf{p}} - e\mathbf{A}(\mathbf{r}, t))^2 \psi_p(\mathbf{r}, t) = e^{iF(\mathbf{r}, t)} (\hat{\mathbf{p}} - e\mathbf{A}(\mathbf{r}, t) - \frac{1}{c}F'(\mathbf{r}, t)\mathbf{n})^2 \phi_p(\mathbf{r}, t), \quad (3.5)$$

where the prime denotes the derivative with respect to the retarded time. Now, expanding the square bracket of the operators on the right-hand sides of the Eqs. (3.4) and (3.5), we get

$$(i\partial_t - V(\mathbf{r}) - F'(\mathbf{r}, t))^2 = (i\partial_t - V(\mathbf{r}))^2 - 2F'(\mathbf{r}, t)(i\partial_t - V(\mathbf{r})) + F'^2(\mathbf{r}, t) - iF''(\mathbf{r}, t), \quad (3.6)$$

$$\begin{aligned} (\hat{\mathbf{p}} - e\mathbf{A}(\mathbf{r}, t) - \frac{1}{c}F'(\mathbf{r}, t)\mathbf{n})^2 &= \hat{\mathbf{p}}^2 - 2(e\mathbf{A}(\mathbf{r}, t) + \frac{1}{c}F'(\mathbf{r}, t)\mathbf{n}) \cdot \hat{\mathbf{p}} + (e\mathbf{A}(\mathbf{r}, t) + \frac{1}{c}F'(\mathbf{r}, t)\mathbf{n})^2 \\ &\quad - \frac{i}{c^2}F''(\mathbf{r}, t), \end{aligned} \quad (3.7)$$

where the Coulomb gauge for the vector potential has been chosen such that $\nabla \cdot \mathbf{A}(\mathbf{r}, t) = 0$. After plugging Eqs. (3.4), (3.5), (3.6) and (3.7) into the Klein-Gordon equation (3.1), we arrive at

$$\begin{aligned} &\left[\frac{1}{c^2} (i\partial_t - V(\mathbf{r}))^2 - \hat{\mathbf{p}}^2 - (m_e c)^2 - \frac{2}{c^2} F'(\mathbf{r}, t) (i\partial_t - V(\mathbf{r})) + 2(e\mathbf{A}(\mathbf{r}, t) + \frac{1}{c} F'(\mathbf{r}, t)\mathbf{n}) \cdot \hat{\mathbf{p}} \right. \\ &\quad \left. - e^2 \mathbf{A}^2(\mathbf{r}, t) \right] \phi_p(\mathbf{r}, t) = 0. \end{aligned} \quad (3.8)$$

In the following, we assume that

$$\frac{2}{c} \left(\frac{E_p}{c} - \mathbf{n} \cdot \mathbf{p} \right) F'(\mathbf{r}, t) = 2e\mathbf{A}(\mathbf{r}, t) \cdot \mathbf{p} + e^2 \mathbf{A}^2(\mathbf{r}, t), \quad (3.9)$$

where E_p is the electron energy. Note that the above condition can be written in a compact form by introducing the four-vector notation. Namely, the four-vectors $x = (ct, \mathbf{r})$, $p = \left(\frac{E_p}{c}, \mathbf{p} \right)$ and $n = (1, \mathbf{n})$, as well as the scalar product defined as $a \cdot b = a^0 \cdot b^0 - \mathbf{a} \cdot \mathbf{b}$, for any two four-vectors $a = (a^0, \mathbf{a})$ and $b = (b^0, \mathbf{b})$. Specifically, the four-vector potential equals $A\left(\frac{n \cdot x}{c}\right) = (0, \mathbf{A}\left(\frac{n \cdot x}{c}\right))$, where $t_R = \frac{n \cdot x}{c}$. Using this notation, Eq. (3.9) becomes

$$F'\left(\frac{n \cdot x}{c}\right) = -c \frac{e\mathbf{A}\left(\frac{n \cdot x}{c}\right) \cdot \mathbf{p}}{n \cdot \mathbf{p}} + c \frac{e^2 \mathbf{A}^2\left(\frac{n \cdot x}{c}\right)}{2n \cdot \mathbf{p}}, \quad (3.10)$$

which leads to

$$F\left(\frac{n \cdot x}{c}\right) = \int^{\frac{n \cdot x}{c}} d\phi \left[-c \frac{e\mathbf{A}(\phi) \cdot \mathbf{p}}{n \cdot \mathbf{p}} + c \frac{e^2 \mathbf{A}^2(\phi)}{2n \cdot \mathbf{p}} \right]. \quad (3.11)$$

With this in mind, Eq. (3.8) can be simplified such that

$$\left[\frac{1}{c^2} (\mathbf{i}\partial_t - V(\mathbf{r}))^2 - \hat{\mathbf{p}}^2 - (m_e c)^2 - \frac{2}{c^2} F'(\mathbf{r}, t) (\mathbf{i}\partial_t - V(\mathbf{r}) - E_p) + 2(e\mathbf{A}(\mathbf{r}, t) + \frac{1}{c} F'(\mathbf{r}, t) \mathbf{n}) \cdot (\hat{\mathbf{p}} - \mathbf{p}) \right] \phi_p(\mathbf{r}, t) = 0. \quad (3.12)$$

Next, we take care of rest-mass oscillations by replacing $\phi_p(\mathbf{r}, t)$ by

$$\phi_p(\mathbf{r}, t) = e^{-im_e c^2 t} \bar{\phi}_p(\mathbf{r}, t). \quad (3.13)$$

This leads us to the following equation,

$$\left[\mathbf{i}\partial_t - V(\mathbf{r}) - \frac{\hat{\mathbf{p}}^2}{2m_e} + \frac{1}{2m_e c^2} (\mathbf{i}\partial_t - V(\mathbf{r}))^2 - \frac{1}{m_e c^2} F'(\mathbf{r}, t) (\mathbf{i}\partial_t - V(\mathbf{r}) + m_e c^2 - E_p) + \frac{1}{m_e} (e\mathbf{A}(\mathbf{r}, t) + \frac{1}{c} F'(\mathbf{r}, t) \mathbf{n}) \cdot (\hat{\mathbf{p}} - \mathbf{p}) \right] \bar{\phi}_p(\mathbf{r}, t) = 0. \quad (3.14)$$

Let us rewrite this equation such that

$$\left[\mathbf{i}\partial_t - V(\mathbf{r}) - \frac{\hat{\mathbf{p}}^2}{2m_e} + \hat{h} \right] \bar{\phi}_p(\mathbf{r}, t) = 0, \quad (3.15)$$

where

$$\hat{h} = \frac{1}{2m_e} (e\mathbf{A}(\mathbf{r}, t) + \frac{1}{c} F'(\mathbf{r}, t) \mathbf{n}) \cdot (\hat{\mathbf{p}} - \mathbf{p}) + \frac{1}{2m_e c^2} \left[(\mathbf{i}\partial_t - V(\mathbf{r}))^2 - 2F'(\mathbf{r}, t) (\mathbf{i}\partial_t - V(\mathbf{r}) + m_e c^2 - E_p) \right]. \quad (3.16)$$

The reason being that \hat{h} can be treated as perturbation to the nonrelativistic atomic problem. For highly energetic electrons, the first term in Eq. (3.16) represents the correction of the order $(\hat{\mathbf{p}} - \mathbf{p})$ [104] whereas the second term represents the correction of the order of $1/c^2$. It is, therefore, justified to represent $\bar{\phi}_p(\mathbf{r}, t)$ as a series

$$\bar{\phi}_p(\mathbf{r}, t) = \bar{\phi}_p^{(0)}(\mathbf{r}, t) + \bar{\phi}_p^{(1)}(\mathbf{r}, t) + \dots, \quad (3.17)$$

where, $\bar{\phi}_p^{(0)}(\mathbf{r}, t)$ is the solution of the unperturbed problem, whereas $\bar{\phi}_p^{(i)}$ ($i = 1, 2, \dots$) are the corrections to the electronic state due to perturbation \hat{h} . By substituting Eq. (3.17) into Eq. (3.15), we obtain the hierarchy of differential equations, where the lowest order equations are

$$\left[\mathbf{i}\partial_t - \frac{\hat{\mathbf{p}}^2}{2m_e} - V(\mathbf{r}) \right] \bar{\phi}_p^{(0)}(\mathbf{r}, t) = 0, \quad (3.18)$$

$$\left[\mathbf{i}\partial_t - \frac{\hat{\mathbf{p}}^2}{2m_e} - V(\mathbf{r}) \right] \bar{\phi}_p^{(1)}(\mathbf{r}, t) = -\hat{h} \bar{\phi}_p^{(0)}(\mathbf{r}, t), \dots \quad (3.19)$$

Clearly, if the perturbation is small, the higher-order corrections are insignificant. Therefore, in the zeroth order of approximation, we are left with nonrelativistic Schrödinger equation (3.18)

for the Coulomb scattering state. For our further purposes, we choose the state with the outgoing boundary conditions, meaning that

$$\bar{\phi}_{\mathbf{p}}^{(0)}(\mathbf{r}, t) = e^{-i\frac{\mathbf{p}^2 t}{2m_e}} e^{i\mathbf{p} \cdot \mathbf{r}} \mathcal{C}_{\mathbf{p}}(\mathbf{r}), \quad (3.20)$$

where

$$\mathcal{C}_{\mathbf{p}}(\mathbf{r}) = \exp\left(\frac{\pi\nu}{2}\right) \Gamma(1 - i\nu) {}_1F_1(i\nu, 1, i(|\mathbf{p}||\mathbf{r}| - \mathbf{p} \cdot \mathbf{r})). \quad (3.21)$$

Here, $\nu = \frac{\mathcal{Z}}{a_0|\mathbf{p}|}$, $\Gamma(\cdot)$ is the Gamma function whereas ${}_1F_1(i\nu, 1, i(|\mathbf{p}||\mathbf{r}| - \mathbf{p} \cdot \mathbf{r}))$ is a confluent hypergeometric function of the first kind. This along with Eqs. (3.3) and (3.13) allows us to write

$$\psi_{\mathbf{p}}(\mathbf{r}, t) = \frac{1}{\sqrt{\mathcal{V}}} e^{-im_e c^2 t + iF(\mathbf{r}, t)} \bar{\phi}_{\mathbf{p}}^{(0)}(\mathbf{r}, t) \quad (3.22)$$

for the scattering state with an outgoing boundary conditions that describes an energetic electron in a Coulomb potential and a laser field. It is known as the Coulomb-Volkov state, where the Volkov phase $F(\mathbf{r}, t)$ in its relativistic form is given by Eq. (3.11).

For our further purpose, let us consider the Coulomb-Volkov state (3.22) in the length gauge, since now on denoted as $\psi_{\mathbf{p}}^{(+)}(\mathbf{r}, t)$. As we will argue later, it takes the following form,

$$\psi_{\mathbf{p}}^{(+)}(\mathbf{r}, t) = e^{-ie\mathbf{A}(\mathbf{r}, t) \cdot \mathbf{r}} \psi_{\mathbf{p}}(\mathbf{r}, t) = \frac{1}{\sqrt{\mathcal{V}}} e^{-im_e c^2 t - ie\mathbf{A}(\mathbf{r}, t) \cdot \mathbf{r} + iF(\mathbf{r}, t)} \bar{\phi}_{\mathbf{p}}^{(0)}(\mathbf{r}, t), \quad (3.23)$$

and is the starting point in deriving the leading order nondipole corrections. They are of different origin:

1. Gauge transformation correction

Since the laser field depends on the retarded time $t_R = t - \frac{\mathbf{n} \cdot \mathbf{r}}{c}$, we can expand the corresponding vector potential in the leading order in $1/c$ such that

$$\mathbf{A}\left(t - \frac{\mathbf{n} \cdot \mathbf{r}}{c}\right) \approx \mathbf{A}(t) + \frac{\mathbf{n} \cdot \mathbf{r}}{c} \mathcal{E}(t) + \dots, \quad (3.24)$$

where $\mathcal{E}(t) = -\frac{\partial \mathbf{A}(t)}{\partial t}$ is the electric field describing the laser light in the dipole approximation. Hence, the gauge transformation phase factor in Eq. (3.23) becomes

$$e^{-ie\mathbf{A}(\mathbf{r}, t) \cdot \mathbf{r}} \approx e^{-ie\mathbf{A}(t) \cdot \mathbf{r}} \left[1 - \frac{ie}{c} (\mathcal{E}(t) \cdot \mathbf{r})(\mathbf{n} \cdot \mathbf{r}) \right]. \quad (3.25)$$

Thus, we will refer to the second term of this expression as the gauge transformation correction.

2. Retardation correction

The Volkov phase (3.11) depends on the retarded time via the upper integration limit.

Hence, expanding Eq. (3.11) in that limit, gives

$$\begin{aligned} F(\mathbf{r}, t) &= \frac{c}{n \cdot \mathbf{p}} \int_0^{t - \frac{n \cdot \mathbf{r}}{c}} d\phi \left[e\mathbf{A}(\phi) \cdot \mathbf{p} - \frac{e^2 \mathbf{A}^2(\phi)}{2} \right] \\ &\approx \frac{c}{n \cdot \mathbf{p}} \int_0^t d\phi \left[e\mathbf{A}(\phi) \cdot \mathbf{p} - \frac{e^2 \mathbf{A}^2(\phi)}{2} \right] - \frac{\mathbf{n} \cdot \mathbf{r}}{n \cdot \mathbf{p}} \left[e\mathbf{A}(t) \cdot \mathbf{p} - \frac{e^2 \mathbf{A}^2(t)}{2} \right], \end{aligned} \quad (3.26)$$

where

$$n \cdot p = \frac{E_{\mathbf{p}}}{c} - \mathbf{n} \cdot \mathbf{p} = \sqrt{(m_e c)^2 + \mathbf{p}^2} - \mathbf{n} \cdot \mathbf{p}. \quad (3.27)$$

3. Recoil correction

As one can see in Eq. (3.26), the Volkov phase contains the coefficient $\frac{1}{n \cdot p}$. It follows from Eq. (3.27) that in the leading order in $1/c$ we have

$$\frac{1}{n \cdot p} \approx \frac{1}{m_e c} \left(1 + \frac{\mathbf{n} \cdot \mathbf{p}}{m_e c} \right), \quad (3.28)$$

which is known as the Nordsieck correction [105]. As it was argued in Ref. [85] in the context of ionisation, this term is responsible for the electron recoil when interacting with the laser field. For this reason, we shall also refer to it as the recoil correction.

Since the retardation (3.26) and recoil (3.28) corrections refer to the Volkov phase, combining them we obtain that, in the leading order in $1/c$, the relativistic Volkov phase can be approximated by

$$F(\mathbf{r}, t) \approx \frac{1}{m_e} \left(1 + \frac{\mathbf{n} \cdot \mathbf{p}}{m_e c} \right) \int_0^t d\phi \left[e\mathbf{A}(\phi) \cdot \mathbf{p} - \frac{e^2 \mathbf{A}^2(\phi)}{2} \right] - \frac{\mathbf{n} \cdot \mathbf{r}}{m_e c} \left[e\mathbf{A}(t) \cdot \mathbf{p} - \frac{e^2 \mathbf{A}^2(t)}{2} \right]. \quad (3.29)$$

Let us compare this expression with the Volkov phase in the dipole approximation, denoted in Chapter 2 as $H(t)$ and given by Eqs. (2.18) and (2.19). The first term in Eq. (3.29) corresponds to $H(t)$ except that it is multiplied by $\left(1 + \frac{\mathbf{n} \cdot \mathbf{p}}{m_e c} \right)$. Note that this is equivalent to introducing into the nonrelativistic theorem that is based on the dipole approximation the effective mass of the electron m_{eff} equal to

$$m_{\text{eff}} = m_e - \frac{\mathbf{n} \cdot \mathbf{p}}{c}. \quad (3.30)$$

The same conclusion has been reached in Ref. [85] regarding nondipole effects in ionisation. Once the radiation pressure of the laser field is accounted for the electron moving in the direction of the field propagation appears to be "lighter"; in contrast to the electron moving in the opposite direction. Hence, the concept of momentum-dependent electron mass arises. On the other hand, the second term in Eq. (3.29) is absent in the dipole approximation and, as it follows from our derivation, it originates from the retardation of a laser wave.

To summarize, by accounting for leading nondipole corrections we have derived that the Coulomb-Volkov scattering state with outgoing boundary conditions, written in the length

gauge, takes the form

$$\psi_{\mathbf{p}}^{(+)}(\mathbf{r}, t) = \frac{1}{\sqrt{\mathcal{V}}} e^{-im_e c^2 t - ie\mathbf{A}(t) \cdot \mathbf{r} + iF(\mathbf{r}, t)} \left[1 - \frac{ie}{c} (\boldsymbol{\mathcal{E}}(t) \cdot \mathbf{r})(\mathbf{n} \cdot \mathbf{r}) \right] \bar{\phi}_{\mathbf{p}}^{(0)}(\mathbf{r}, t), \quad (3.31)$$

where $F(\mathbf{r}, t)$ is given by Eq. (3.29), whereas $\bar{\phi}_{\mathbf{p}}^{(0)}(\mathbf{r}, t)$ is defined by Eqs. (3.20) and (3.21). It has been derived assuming large electron momenta. In this case, the state resembles the state corresponding to the instantaneous electron momentum, $\boldsymbol{\pi}(t) = \mathbf{p} - e\mathbf{A}(t) - \frac{n}{m_e c} \left[e\mathbf{A}(t) \cdot \mathbf{p} - \frac{e^2}{2} \mathbf{A}^2(t) \right]$. While in the dipole approximation, the corresponding momentum is $\boldsymbol{\pi}^{(\text{dip})}(t) = \mathbf{p} - e\mathbf{A}(t)$, as it follows from Eq. (2.12), here we have an additional term. This additional momentum is in the direction of the laser field propagation. Thus showing that the electron is exposed to radiation pressure, that is absent in the dipole approximation. The state (3.31) will be used next when deriving the LARR probability amplitude.

3.2.2 LARR by an impact of a monoenergetic electron wave

Consider the recombination of an electron by atomic potential $V(\hat{\mathbf{r}})$ in the presence of a laser field with the emission of a photon. We assume that the emitted photon carries the energy $\omega_{\mathbf{K}}$, the wave vector \mathbf{K} , and polarisation $\boldsymbol{\varepsilon}_{\mathbf{K}}$. The external laser field and emitted photon field depend on both space and time.

The Hamiltonian describing the process takes the form

$$\hat{H}(\hat{\mathbf{r}}, t) = \frac{1}{2m_e} (\hat{\mathbf{p}} - e\mathbf{A}(\hat{\mathbf{r}}, t) - e\hat{\mathbf{A}}_{\mathbf{K}}(\hat{\mathbf{r}}, t))^2 + V(\hat{\mathbf{r}}). \quad (3.32)$$

Here, $\mathbf{A}(\hat{\mathbf{r}}, t) = \mathbf{A}(t - \frac{\mathbf{n} \cdot \hat{\mathbf{r}}}{c})$ represents vector potential corresponding to the classical laser field propagating in the \mathbf{n} -direction, whereas $\hat{\mathbf{A}}_{\mathbf{K}}(\hat{\mathbf{r}}, t) = \hat{\mathbf{A}}_{\mathbf{K}}(t - \frac{\mathbf{n}_{\mathbf{K}} \cdot \hat{\mathbf{r}}}{c})$ represents the vector potential corresponding to the quantized electromagnetic field propagating in the direction $\mathbf{n}_{\mathbf{K}}$. We assume that these fields are transverse, meaning that $\mathbf{n} \cdot \mathbf{A}(\hat{\mathbf{r}}, t) = \mathbf{n}_{\mathbf{K}} \cdot \hat{\mathbf{A}}_{\mathbf{K}}(\hat{\mathbf{r}}, t) = 0$, and we define the corresponding electric fields $\boldsymbol{\mathcal{E}}(\hat{\mathbf{r}}, t) = -\frac{\partial \mathbf{A}(\hat{\mathbf{r}}, t)}{\partial t}$ and $\hat{\boldsymbol{\mathcal{E}}}_{\mathbf{K}}(\hat{\mathbf{r}}, t) = -\frac{\partial \hat{\mathbf{A}}_{\mathbf{K}}(\hat{\mathbf{r}}, t)}{\partial t}$.

The Hamiltonian within the length gauge can be obtained by applying a unitary transformation

$$\hat{U}(\hat{\mathbf{r}}, t) = \exp[-ie\mathbf{A}(\hat{\mathbf{r}}, t) \cdot \hat{\mathbf{r}} - ie\hat{\mathbf{A}}_{\mathbf{K}}(\hat{\mathbf{r}}, t) \cdot \hat{\mathbf{r}}] \quad (3.33)$$

to Eq. (3.32). This is done according to Eq. (B.4) [see Appendix B.1, for more details],

$$\begin{aligned} \hat{H}'(\hat{\mathbf{r}}, t) &= [i\partial_t \hat{U}(\hat{\mathbf{r}}, t)] \hat{U}^\dagger(\hat{\mathbf{r}}, t) + \hat{U}(\hat{\mathbf{r}}, t) \hat{H}(\hat{\mathbf{r}}, t) \hat{U}^\dagger(\hat{\mathbf{r}}, t) \\ &= -e\boldsymbol{\mathcal{E}}(\hat{\mathbf{r}}, t) \cdot \hat{\mathbf{r}} - e\hat{\boldsymbol{\mathcal{E}}}_{\mathbf{K}}(\hat{\mathbf{r}}, t) \cdot \hat{\mathbf{r}} + \hat{U}^\dagger(\hat{\mathbf{r}}, t) \hat{H}(\hat{\mathbf{r}}, t) \hat{U}(\hat{\mathbf{r}}, t). \end{aligned} \quad (3.34)$$

In order to find an explicit form of the third term of the above equation, we use Baker-Campbell-Hausdorff formula, $e^{\lambda G} A e^{-\lambda G} = A + \lambda[G, A] + \frac{\lambda^2}{2}[G, [G, A]] + \dots$ [106]. As a result, we obtain

$$\hat{U}^\dagger(\hat{\mathbf{r}}, t) (\hat{\mathbf{p}} - e\mathbf{A}(\hat{\mathbf{r}}, t) - e\hat{\mathbf{A}}_{\mathbf{K}}(\hat{\mathbf{r}}, t)) \hat{U}(\hat{\mathbf{r}}, t) = \hat{\mathbf{p}} + \frac{n}{c} (e\boldsymbol{\mathcal{E}}(\hat{\mathbf{r}}, t) \cdot \hat{\mathbf{r}}) + \frac{\mathbf{n}_{\mathbf{K}}}{c} (e\hat{\boldsymbol{\mathcal{E}}}_{\mathbf{K}}(\hat{\mathbf{r}}, t) \cdot \hat{\mathbf{r}}), \quad (3.35)$$

and

$$\hat{U}^\dagger(\hat{\mathbf{r}}, t) (\hat{\mathbf{p}} - e\mathbf{A}(\hat{\mathbf{r}}, t) - e\hat{\mathbf{A}}_{\mathbf{K}}(\hat{\mathbf{r}}, t))^2 \hat{U}(\hat{\mathbf{r}}, t) = \left[\hat{\mathbf{p}} + \frac{\mathbf{n}}{c} (e\mathcal{E}(\hat{\mathbf{r}}, t) \cdot \hat{\mathbf{r}}) + \frac{\mathbf{n}_{\mathbf{K}}}{c} (e\hat{\mathcal{E}}_{\mathbf{K}}(\hat{\mathbf{r}}, t) \cdot \hat{\mathbf{r}}) \right]^2. \quad (3.36)$$

Hence, the new Hamiltonian (3.34) takes the form

$$\begin{aligned} \hat{H}'(\hat{\mathbf{r}}, t) &= -e\mathcal{E}(\hat{\mathbf{r}}, t) \cdot \hat{\mathbf{r}} - e\hat{\mathcal{E}}_{\mathbf{K}}(\hat{\mathbf{r}}, t) \cdot \hat{\mathbf{r}} \\ &+ \frac{1}{2m_e} \left[\hat{\mathbf{p}} + \frac{\mathbf{n}}{c} (e\mathcal{E}(\hat{\mathbf{r}}, t) \cdot \hat{\mathbf{r}}) + \frac{\mathbf{n}_{\mathbf{K}}}{c} (e\hat{\mathcal{E}}_{\mathbf{K}}(\hat{\mathbf{r}}, t) \cdot \hat{\mathbf{r}}) \right]^2 + V(\hat{\mathbf{r}}). \end{aligned} \quad (3.37)$$

Neglecting the terms of the order $1/c^2$ and higher, we obtain

$$\hat{H}'(\hat{\mathbf{r}}, t) = \hat{H}_0(\hat{\mathbf{r}}, t) + \hat{H}''(\hat{\mathbf{r}}, t), \quad (3.38)$$

where

$$\hat{H}_0(\hat{\mathbf{r}}, t) = \frac{\hat{\mathbf{p}}^2}{2m_e} + V(\hat{\mathbf{r}}) - e\mathcal{E}(\hat{\mathbf{r}}, t) \cdot \hat{\mathbf{r}} \left(1 - \frac{\mathbf{n} \cdot \hat{\mathbf{p}}}{m_e c} \right) \quad (3.39)$$

describes an electron in the atomic potential and the laser field, whereas

$$\hat{H}''(\hat{\mathbf{r}}, t) = -e\hat{\mathcal{E}}_{\mathbf{K}}(\hat{\mathbf{r}}, t) \cdot \hat{\mathbf{r}} \left(1 - \frac{\mathbf{n}_{\mathbf{K}} \cdot \hat{\mathbf{p}}}{m_e c} \right) \quad (3.40)$$

represents the electron interaction with the quantized field $\hat{\mathcal{E}}_{\mathbf{K}}(\hat{\mathbf{r}}, t)$, which is given by Eqs. (2.4) and (2.5).

Let us define the probability amplitude of LARR governed by the perturbation $\hat{H}''(\hat{\mathbf{r}}, t)$ in the length gauge such that

$$\mathcal{A}(\mathbf{p}) = -i \int_{-\infty}^{\infty} dt \langle \psi_B(t); 1_{\mathbf{K}} | \hat{H}''(\hat{\mathbf{r}}, t) | \psi_p^{(+)}(t); 0_{\mathbf{K}} \rangle, \quad (3.41)$$

where the initial electron scattering state $\psi_p^{(+)}(\mathbf{r}, t)$ is defined by Eq. (3.31) whereas the final electron bound state $\psi_B(\mathbf{r}, t)$ is given by the following formulas

$$\psi_B(\mathbf{r}, t) = e^{-iE_B t} e^{-im_e c^2 t} \psi_B(\mathbf{r}), \quad (3.42)$$

with

$$\psi_B(\mathbf{r}) = \frac{1}{\sqrt{\pi}} \left(\frac{\mathcal{Z}}{a_0} \right)^{3/2} e^{-\mathcal{Z}r/a_0}, \quad (3.43)$$

and the binding energy equal to $E_B = -\frac{\mathcal{Z}^2 E_0}{2}$. Both $\psi_B(\mathbf{r}, t)$ and $\psi_p^{(+)}(\mathbf{r}, t)$ should be in principle the exact eigenstates of $\hat{H}_0(\mathbf{r}, t)$. However, they are not known, thus need to be approximated. Here, it is done using the relativistic reduction of Klein-Gordon equation in the leading order in $1/c$. Note the appearance of the free mass oscillations in Eq. (3.42). They appear when we derive the electron bound state from the Klein-Gordon equation as well.

Substituting Eq. (3.40) together with Eqs. (2.4) and (2.5) into Eq. (3.41), the probability amplitude of LARR [Eq. (3.41)] in the position representation takes the form

$$\mathcal{A}(\mathbf{p}) = e \sqrt{\frac{\omega_{\mathbf{K}}}{2\epsilon_0 \mathcal{V}}} \int_{-\infty}^{\infty} dt \int d^3 \mathbf{r} e^{i(\omega_{\mathbf{K}} t - \mathbf{K} \cdot \mathbf{r})} \psi_{\mathbf{B}}^*(\mathbf{r}, t) (\boldsymbol{\varepsilon}_{\mathbf{K}} \cdot \mathbf{r}) \left(1 - \frac{\mathbf{n}_{\mathbf{K}} \cdot \hat{\mathbf{p}}}{m_e c}\right) \psi_{\mathbf{p}}^{(+)}(\mathbf{r}, t). \quad (3.44)$$

Following the discussion of Eq. (3.31) we can figure out that for large momenta, $\hat{\mathbf{p}} \psi_{\mathbf{p}}^{(+)}(\mathbf{r}, t) \approx \left(\mathbf{p} - e\mathbf{A}(t) - \frac{\mathbf{n}}{m_e c} \left[e\mathbf{A}(t) \cdot \mathbf{p} - \frac{e^2}{2} \mathbf{A}^2(t)\right]\right) \psi_{\mathbf{p}}^{(+)}(\mathbf{r}, t)$. Since this term is divided in Eq. (3.44) by c , it is justified in the leading order in $1/c$ to approximate that $\frac{\hat{\mathbf{p}}}{m_e c} \psi_{\mathbf{p}}^{(+)}(\mathbf{r}, t) \approx \frac{\mathbf{p} - e\mathbf{A}(t)}{m_e c} \psi_{\mathbf{p}}^{(+)}(\mathbf{r}, t)$. Hence, Eq. (3.44) takes the form

$$\mathcal{A}(\mathbf{p}) = e \sqrt{\frac{\omega_{\mathbf{K}}}{2\epsilon_0 \mathcal{V}}} \int_{-\infty}^{\infty} dt \int d^3 \mathbf{r} e^{i(\omega_{\mathbf{K}} t - \mathbf{K} \cdot \mathbf{r})} \psi_{\mathbf{B}}^*(\mathbf{r}, t) (\boldsymbol{\varepsilon}_{\mathbf{K}} \cdot \mathbf{r}) G_{\mathbf{p}}(t) \psi_{\mathbf{p}}^{(+)}(\mathbf{r}, t), \quad (3.45)$$

where

$$G_{\mathbf{p}}(t) = 1 - \frac{\mathbf{n}_{\mathbf{K}} \cdot (\mathbf{p} - e\mathbf{A}(t))}{m_e c}. \quad (3.46)$$

Furthermore, substituting the scattering electron states (3.31) and bound state [Eq. (3.42) and (3.43)] in Eq. (3.45) we arrive at the following expression describing the LARR probability amplitude up to the leading nondipole corrections,

$$\begin{aligned} \mathcal{A}(\mathbf{p}) &= \frac{Z e}{a_0 \mathcal{V}} \sqrt{\frac{Z \omega_{\mathbf{K}}}{2\pi \epsilon_0 a_0}} e^{\frac{\pi \nu}{2}} \Gamma(1 - i\nu) \int_{-\infty}^{\infty} dt e^{iQt + iH_{\text{eff}}(t)} \int d^3 \mathbf{r} (\boldsymbol{\varepsilon}_{\mathbf{K}} \cdot \mathbf{r}) \\ &\times \left[G_{\mathbf{p}}(t) - ie\boldsymbol{\mathcal{E}}(t) \cdot \mathbf{r} \frac{\mathbf{n} \cdot \mathbf{r}}{c} \right] {}_1F_1(i\nu, 1, i(|\mathbf{p}||\mathbf{r}| - \mathbf{p} \cdot \mathbf{r})) e^{-Zr/a_0 + i\mathbf{q}(t) \cdot \mathbf{r}}. \end{aligned} \quad (3.47)$$

Here, we have introduced Q defined by Eq. (2.17) along with

$$H_{\text{eff}}(t) = \frac{1}{m_e} \left(1 + \frac{\mathbf{n} \cdot \mathbf{p}}{m_e c}\right) \int_0^t d\phi \left[e\mathbf{A}(\phi) \cdot \mathbf{p} - \frac{e^2}{2} \mathbf{A}^2(\phi) \right], \quad (3.48)$$

$$\mathbf{q}(t) = \mathbf{p} - e\mathbf{A}(t) - \mathbf{K} - \frac{\mathbf{n}}{m_e c} \left[e\mathbf{A}(t) \cdot \mathbf{p} - \frac{e^2}{2} \mathbf{A}^2(t) \right]. \quad (3.49)$$

Note that $H_{\text{eff}}(t)$ accounts for recoil correction (3.28) while $\mathbf{q}(t)$ contains retardation correction coming from Eq. (3.26). In addition, $G_{\mathbf{p}}(t)$ [Eq. (3.46)] arises from the electron-photon interaction Hamiltonian (3.40) while performing the length gauge transformation.

The LARR probability amplitude (3.47) has the following structure

$$\mathcal{A}(\mathbf{p}) = \mathcal{N} \int_{-\infty}^{\infty} dt e^{iQt + iH_{\text{eff}}(t)} \left[G_{\mathbf{p}}(t) \mathcal{B}(t) - \frac{1}{c} \mathcal{D}(t) \right], \quad (3.50)$$

where

$$\mathcal{N} = \frac{Z e}{a_0 \mathcal{V}} \sqrt{\frac{Z \omega_{\mathbf{K}}}{2\pi \epsilon_0 a_0}} \Gamma(1 - i\nu) e^{\frac{\pi \nu}{2}}, \quad (3.51)$$

whereas

$$\mathcal{B}(t) = \int d^3\mathbf{r} (\boldsymbol{\varepsilon}_K \cdot \mathbf{r}) e^{-Zr/a_0 + i\mathbf{q}(t) \cdot \mathbf{r}} {}_1F_1(i\nu, 1, i(|\mathbf{p}||\mathbf{r}| - \mathbf{p} \cdot \mathbf{r})) \quad (3.52)$$

and

$$\mathcal{D}(t) = i \int d^3\mathbf{r} (\boldsymbol{\varepsilon}_K \cdot \mathbf{r})(\mathbf{n} \cdot \mathbf{r})(e\boldsymbol{\mathcal{E}}(t) \cdot \mathbf{r}) e^{-Zr/a_0 + i\mathbf{q}(t) \cdot \mathbf{r}} {}_1F_1(i\nu, 1, i(|\mathbf{p}||\mathbf{r}| - \mathbf{p} \cdot \mathbf{r})). \quad (3.53)$$

Both integrals given by Eqs. (3.52) and (3.53) can be expressed in terms of the Nordsieck integral defined as (see, Appendix B.2)

$$f(\nu, \lambda, \mathbf{q}, \mathbf{p}) = \int d^3r \frac{e^{-\lambda r}}{r} e^{i\mathbf{q} \cdot \mathbf{r}} {}_1F_1(i\nu, 1, i(|\mathbf{p}||\mathbf{r}| - \mathbf{p} \cdot \mathbf{r})). \quad (3.54)$$

As elaborated in detail in Appendix B.2, this integral can be performed analytically, leading to

$$f(\nu, \lambda, \mathbf{q}, \mathbf{p}) = 4\pi\zeta(1 + \tilde{\zeta})^{-i\nu}, \quad (3.55)$$

where

$$\zeta = \frac{1}{\lambda^2 + \mathbf{q}^2}, \quad \tilde{\zeta} = -2\zeta(\mathbf{p} \cdot \mathbf{q} + i\lambda|\mathbf{p}|). \quad (3.56)$$

Thus, going back to Eqs. (3.52) and (3.53), we conclude that

$$\mathcal{B}(t) = i \frac{\partial}{\partial \lambda} (\boldsymbol{\varepsilon}_K \cdot \nabla_{\mathbf{q}}) f(\nu, \lambda, \mathbf{q}, \mathbf{p}), \quad (3.57)$$

and

$$\mathcal{D}(t) = \frac{\partial}{\partial \lambda} (\boldsymbol{\varepsilon}_K \cdot \nabla_{\mathbf{q}}) (e\boldsymbol{\mathcal{E}}(t) \cdot \nabla_{\mathbf{q}}) (\mathbf{n} \cdot \nabla_{\mathbf{q}}) f(\nu, \lambda, \mathbf{q}, \mathbf{p}), \quad (3.58)$$

where $\mathbf{q} = \mathbf{q}(t)$ is given by Eq. (3.49) and $\lambda = Z/a_0$. Specifically, $\mathcal{B}(t)$ can be calculated with the help of Eq. (B.97) and $\mathcal{D}(t)$ using Eq. (B.101). For more technical details we refer the reader to Appendix B.3.

The focus of this thesis is on radiative recombination in a finite laser field, i.e., lasting from 0 to T_p . In this case, the first term in Eq. (3.50) is divergent; the problem which we have already encountered in Chapter 2. As we have elaborated there, such divergence can be treated using the Boca-Florescu transformation [67]. In relation to Eq. (3.50) we define, therefore, the regularised integral,

$$I(\epsilon) = \int_{-\infty}^{\infty} dt e^{iQt + iH_{\text{eff}}(t) - \epsilon|t|} \mathcal{B}(t) G_{\mathbf{p}}(t), \quad (3.59)$$

where $\epsilon > 0$. Here, we are interested in the limit when $\epsilon \rightarrow 0^+$. In order to calculate $\mathcal{I}(\epsilon)$, we split the integral into two intervals and each of them is calculated by parts as follows

$$\begin{aligned}
I(\epsilon) &= \int_{-\infty}^0 dt e^{i(Q-i\epsilon)t} e^{iH_{\text{eff}}(t)} \mathcal{B}(t) G_{\mathbf{p}}(t) + \int_0^{\infty} dt e^{i(Q+i\epsilon)t} e^{iH_{\text{eff}}(t)} \mathcal{B}(t) G_{\mathbf{p}}(t) \\
&= e^{iH_{\text{eff}}(t)} \mathcal{B}(t) G_{\mathbf{p}}(t) \frac{e^{i(Q-i\epsilon)t}}{i(Q-i\epsilon)} \Big|_{-\infty}^0 + e^{iH_{\text{eff}}(t)} \mathcal{B}(t) G_{\mathbf{p}}(t) \frac{e^{i(Q+i\epsilon)t}}{i(Q+i\epsilon)} \Big|_0^{\infty} \\
&\quad - \frac{1}{i(Q-i\epsilon)} \int_{-\infty}^0 dt [i\dot{H}_{\text{eff}}(t) \mathcal{B}(t) G_{\mathbf{p}}(t) + \dot{\mathcal{B}}(t) G_{\mathbf{p}}(t) + \mathcal{B}(t) \dot{G}_{\mathbf{p}}(t)] e^{i(Q-i\epsilon)t} e^{iH_{\text{eff}}(t)} \\
&\quad - \frac{1}{i(Q+i\epsilon)} \int_0^{\infty} dt [i\dot{H}_{\text{eff}}(t) \mathcal{B}(t) G_{\mathbf{p}}(t) + \dot{\mathcal{B}}(t) G_{\mathbf{p}}(t) + \mathcal{B}(t) \dot{G}_{\mathbf{p}}(t)] e^{i(Q+i\epsilon)t} e^{iH_{\text{eff}}(t)}. \quad (3.60)
\end{aligned}$$

Because $H_{\text{eff}}(0) = 0$ and $\dot{H}_{\text{eff}}(t) = 0$ for $t > T_p$ [see, Eq. (3.48)], we arrive at the formula

$$\begin{aligned}
I(\epsilon) &= \frac{2\epsilon}{Q^2 + \epsilon^2} \mathcal{B}(0) G_{\mathbf{p}}(0) + \frac{i}{(Q+i\epsilon)} \int_0^{T_p} dt [i\dot{H}_{\text{eff}}(t) \mathcal{B}(t) G_{\mathbf{p}}(t) + \dot{\mathcal{B}}(t) G_{\mathbf{p}}(t) \\
&\quad + \mathcal{B}(t) \dot{G}_{\mathbf{p}}(t)] e^{i(Q+i\epsilon)t} e^{iH_{\text{eff}}(t)}. \quad (3.61)
\end{aligned}$$

When taking the limit $\epsilon \rightarrow 0^+$, we use Eq. (2.33). Hence,

$$\begin{aligned}
\lim_{\epsilon \rightarrow 0^+} I(\epsilon) &= 2\pi \mathcal{B}(0) G_{\mathbf{p}}(0) \delta(Q) + \frac{i}{(Q+i\epsilon)} \int_0^{T_p} dt [i\dot{H}_{\text{eff}}(t) \mathcal{B}(t) G_{\mathbf{p}}(t) + \dot{\mathcal{B}}(t) G_{\mathbf{p}}(t) \\
&\quad + \mathcal{B}(t) \dot{G}_{\mathbf{p}}(t)] e^{iQt+iH_{\text{eff}}(t)}. \quad (3.62)
\end{aligned}$$

Here, the prescription how to avoid the singularity at $Q = 0$ has been kept. In the next step, we use the Sokhotski-Plemelji formula [68], $\frac{1}{Q+i\epsilon} = \mathcal{P}(\frac{1}{Q}) - i\pi\delta(Q)$, which gives

$$\begin{aligned}
\lim_{\epsilon \rightarrow 0^+} I(\epsilon) &= 2\pi \mathcal{B}(0) G_{\mathbf{p}}(0) \delta(Q) \\
&\quad + \pi\delta(Q) \int_0^{T_p} dt [i\dot{H}_{\text{eff}}(t) \mathcal{B}(t) G_{\mathbf{p}}(t) + \dot{\mathcal{B}}(t) G_{\mathbf{p}}(t) + \mathcal{B}(t) \dot{G}_{\mathbf{p}}(t)] e^{iH_{\text{eff}}(t)} \\
&\quad + i\mathcal{P}(\frac{1}{Q}) \int_0^{T_p} dt [i\dot{H}_{\text{eff}}(t) \mathcal{B}(t) G_{\mathbf{p}}(t) + \dot{\mathcal{B}}(t) G_{\mathbf{p}}(t) + \mathcal{B}(t) \dot{G}_{\mathbf{p}}(t)] e^{iQt+iH_{\text{eff}}(t)}. \quad (3.63)
\end{aligned}$$

The first integral can be performed exactly using the fact that

$$\frac{d}{dt} [e^{iH_{\text{eff}}(t)} \mathcal{B}(t) G_{\mathbf{p}}(t)] = [i\dot{H}_{\text{eff}}(t) \mathcal{B}(t) G_{\mathbf{p}}(t) + \dot{\mathcal{B}}(t) G_{\mathbf{p}}(t) + \mathcal{B}(t) \dot{G}_{\mathbf{p}}(t)] e^{iH_{\text{eff}}(t)}. \quad (3.64)$$

As a result, we obtain

$$\begin{aligned}
\lim_{\epsilon \rightarrow 0^+} I(\epsilon) &= 2\pi \mathcal{B}(0) G_{\mathbf{p}}(0) \delta(Q) + \pi\delta(Q) [\mathcal{B}(T_p) G_{\mathbf{p}}(T_p) e^{iH_{\text{eff}}(T_p)} - \mathcal{B}(0) G_{\mathbf{p}}(0) e^{iH_{\text{eff}}(0)}] \\
&\quad + i\mathcal{P}(\frac{1}{Q}) \int_0^{T_p} dt [i\dot{H}_{\text{eff}}(t) \mathcal{B}(t) G_{\mathbf{p}}(t) + \dot{\mathcal{B}}(t) G_{\mathbf{p}}(t) + \mathcal{B}(t) \dot{G}_{\mathbf{p}}(t)] e^{iQt+iH_{\text{eff}}(t)}. \quad (3.65)
\end{aligned}$$

By taking into account that $H_{\text{eff}}(0) = 0$ as well as $G_{\mathbf{p}}(T_p) = G_{\mathbf{p}}(0)$ and $\mathcal{B}(T_p) = \mathcal{B}(0)$ [see, Eqs. (3.48), (3.46) and (3.52)], we finally arrive at

$$\begin{aligned} \lim_{\epsilon \rightarrow 0^+} I(\epsilon) &= 2\pi\mathcal{B}(0)G_{\mathbf{p}}(0)\delta(Q)e^{iH_{\text{eff}}(T_p)/2} \cos\left(H_{\text{eff}}(T_p)/2\right) \\ &+ i\mathcal{P}\left(\frac{1}{Q}\right) \int_0^{T_p} dt [i\dot{H}_{\text{eff}}(t)\mathcal{B}(t)G_{\mathbf{p}}(t) + \dot{\mathcal{B}}(t)G_{\mathbf{p}}(t) + \mathcal{B}(t)\dot{G}_{\mathbf{p}}(t)]e^{iQt+iH_{\text{eff}}(t)}. \end{aligned} \quad (3.66)$$

Going back to the probability amplitude of LARR [Eq. (3.50)], we obtain based on Eq. (3.66) that

$$\begin{aligned} \mathcal{A}(\mathbf{p}) &= \mathcal{N} \left[2\pi\mathcal{B}(0)G_{\mathbf{p}}(0)\delta(Q)e^{iH_{\text{eff}}(T_p)/2} \cos\left(H_{\text{eff}}(T_p)/2\right) \right. \\ &+ i\mathcal{P}\left(\frac{1}{Q}\right) \int_0^{T_p} dt [i\dot{H}_{\text{eff}}(t)\mathcal{B}(t)G_{\mathbf{p}}(t) + \dot{\mathcal{B}}(t)G_{\mathbf{p}}(t) + \mathcal{B}(t)\dot{G}_{\mathbf{p}}(t)]e^{iQt+iH_{\text{eff}}(t)} \\ &\left. - \frac{1}{c} \int_0^{T_p} dt e^{iQt+iH_{\text{eff}}(t)} \mathcal{D}(t) \right]. \end{aligned} \quad (3.67)$$

Also, we have used the fact that $\mathcal{D}(t)$ is nonzero only within the time interval $[0, T_p]$.

As it follows from the formula (3.67), the general features of the LARR probability amplitude are similar to those encountered in Chapter 2 for LARA treated within the dipole approximation. Namely, the probability of LARR does account for a laser-field-free process. This is clear from the presence of the Dirac delta function in Eq. (3.67) leading to the energy conservation condition (2.44). It is also clear from Eq. (3.67) that this point spectrum is accompanied by a contribution present only in a laser field. Note, however, that this contribution can be significantly modified by nondipole effects which will be investigated later.

For our further purposes, we rewrite Eq. (3.67) in a more compact form. First of all, we note that the emitted LARR photons can be elliptically polarised, in which case $\boldsymbol{\varepsilon}_{\mathbf{K}}$ can be decomposed in two linear polarisations $\boldsymbol{\varepsilon}_{\mathbf{K}1}$ and $\boldsymbol{\varepsilon}_{\mathbf{K}2}$ following Eq. (2.36). Thus, for each of those components ($j = 1, 2$) we define the functions,

$$\mathcal{B}_j(t) = i\frac{\partial}{\partial\lambda}(\boldsymbol{\varepsilon}_{\mathbf{K}j} \cdot \nabla_{\mathbf{q}})f(\nu, \lambda, \mathbf{q}, \mathbf{p}), \quad (3.68)$$

$$\mathcal{D}_j(t) = \frac{\partial}{\partial\lambda}(\boldsymbol{\varepsilon}_{\mathbf{K}j} \cdot \nabla_{\mathbf{q}})(e\boldsymbol{\mathcal{E}}(t) \cdot \nabla_{\mathbf{q}})(\mathbf{n} \cdot \nabla_{\mathbf{q}})f(\nu, \lambda, \mathbf{q}, \mathbf{p}), \quad (3.69)$$

in accordance with Eqs. (3.57) and (3.53). We also introduce the functions

$$\mathcal{R}_j^{(0)}(\mathbf{p}) = 2\pi\mathcal{B}_j(0)G_{\mathbf{p}}(0)e^{iH_{\text{eff}}(T_p)/2} \cos\left(H_{\text{eff}}(T_p)/2\right), \quad (3.70)$$

$$\mathcal{R}_j^{(1)}(\mathbf{p}) = i \int_0^{T_p} dt [i\dot{H}_{\text{eff}}(t)\mathcal{B}_j(t) + \dot{\mathcal{B}}_j(t)G_{\mathbf{p}}(t) + \mathcal{B}_j(t)\dot{G}_{\mathbf{p}}(t)]e^{iQt+iH_{\text{eff}}(t)}, \quad (3.71)$$

$$\mathcal{R}_j^{(2)}(\mathbf{p}) = -\frac{1}{c} \int_0^{T_p} dt \mathcal{D}_j(t)e^{iQt+iH_{\text{eff}}(t)}, \quad (3.72)$$

which determine contributions to the LARR probability amplitude (3.67). Namely, accounting for ellipticity parameter δ characterizing the emitted radiation according to Eq. (2.36), we have

$$\mathcal{R}_\delta^{(\ell)} = \cos \delta \mathcal{R}_1^{(\ell)} + i \sin \delta \mathcal{R}_2^{(\ell)}, \quad \text{for } \ell = 0, 1, 2. \quad (3.73)$$

This in turn allows us to rewrite Eq. (3.67) such that

$$\mathcal{A}(\mathbf{p}) = \mathcal{N} \mathcal{R}(\mathbf{p}), \quad (3.74)$$

with

$$\mathcal{R}(\mathbf{p}) = \delta(Q) \mathcal{R}_\delta^{(0)}(\mathbf{p}) + i \mathcal{P}\left(\frac{1}{Q}\right) \mathcal{R}_\delta^{(1)}(\mathbf{p}) + \mathcal{R}_\delta^{(2)}(\mathbf{p}). \quad (3.75)$$

Note that in deriving these formula we have assumed a monochromatic electron wave $\psi_{\mathbf{p}}^{(+)}(\mathbf{r}, t)$ [Eq. (3.31)] as the initial state. Next, we will generalize this formulation to account for a coherent superposition of those waves, similar to what has been worked out in Chapter 2.

3.2.3 LARR by an impact of an electron wave packet

In order to smooth out divergences that appear in Eq. (3.75) defining the probability amplitude of LARR [Eq. (3.74)], we consider now a coherent electron wave packet interacting with a positive ion and a laser field. It is defined by Eq. (2.46) except that this time $\psi_{\mathbf{p}}^{(+)}(\mathbf{r}, t)$ is given as the Coulomb-Volkov wave with nondipole corrections, Eq. (3.31). We still assume that the wave packet describes nearly monoenergetic electrons, which allows us to define the LARR probability amplitude (3.74) integrated over the initial electron momentum profile $f_{\mathbf{p}}(\mathbf{q})$ such that

$$\begin{aligned} \langle \mathcal{A}(\mathbf{p}) \rangle &= \int d^3 \mathbf{q} \mathcal{A}(\mathbf{q}) f_{\mathbf{p}}(\mathbf{q}) = \mathcal{N} \langle \mathcal{R}_\delta(\mathbf{p}) \rangle \\ &= \mathcal{N} \left[\langle \delta(Q) \rangle \mathcal{R}_\delta^{(0)}(\mathbf{p}) + i \langle \mathcal{P}\left(\frac{1}{Q}\right) \rangle \mathcal{R}_\delta^{(1)}(\mathbf{p}) + \mathcal{R}_\delta^{(2)}(\mathbf{p}) \right]. \end{aligned} \quad (3.76)$$

Here, $\mathcal{N} \mathcal{R}_\delta^{(\ell)}(\mathbf{p})$ are slowly varying functions of \mathbf{p} ($\ell = 0, 1, 2$). For a Lorentzian shape profile $f_{\mathbf{p}}(\mathbf{q})$, as specified by Eq. (2.63), the averages $\langle \delta(Q) \rangle$ and $\langle \mathcal{P}\left(\frac{1}{Q}\right) \rangle$ are given by Eq. (2.68) and (2.75), respectively. Thus, Eq. (3.76) defines the probability amplitude of LARR integrated over the initial electron momentum distribution (2.63).

3.2.4 Energy distributions of LARR radiation

The total energy $E_{\mathbf{K}}(\mathbf{p})$ (per the initial electron flux) irradiated over the density of final photon states, $\mathcal{V} d^3 \mathbf{K} / (2\pi)^3$, is defined by Eq. (2.53). As shown in Ref. [107], the initial electron flux is given by Eq. (2.54). Hence, substituting in Eq. (2.53) that $d^3 \mathbf{K} = \omega_{\mathbf{K}}^2 d\omega_{\mathbf{K}} d^2 \Omega_{\mathbf{K}} / c^3$, where $d^2 \Omega_{\mathbf{K}}$ is the solid angle of emitted photons, we arrive at

$$E_{\mathbf{K}}(\mathbf{p}) = \frac{m_e \mathcal{V}^2}{|\mathbf{p}|} \frac{|\mathcal{N}|^2}{(2\pi c)^3} \int d^2 \Omega_{\mathbf{K}} \int d\omega_{\mathbf{K}} \omega_{\mathbf{K}}^3 |\langle \mathcal{R}_\delta(\mathbf{p}) \rangle|^2, \quad (3.77)$$

where we have used the relation (3.74). Substituting here Eq. (3.51), we obtain

$$E_{\mathbf{K}}(\mathbf{p}) = \frac{\alpha m_e |\mathbf{p}|^2}{(2\pi c)^2} \frac{v^4 e^{\pi v}}{\sinh(\pi v)} \int d^2\Omega_{\mathbf{K}} \int d\omega_{\mathbf{K}} \omega_{\mathbf{K}}^4 |\langle \mathcal{R}_{\delta}(\mathbf{p}) \rangle|^2, \quad (3.78)$$

where the property $|\Gamma(1 - iv)|^2 = \frac{\pi v}{\sinh(\pi v)}$ has been applied [108]. By comparing the above expression with Eq. (2.56), we conclude that the triply differential energy distribution (per the initial electron flux) of photons emitted in the solid angle $d^2\Omega_{\mathbf{K}}$ with energies within the interval $(\omega_{\mathbf{K}}, \omega_{\mathbf{K}} + d\omega_{\mathbf{K}})$ equals

$$\frac{d^3 E_{\mathbf{K}}(\mathbf{p})}{d\omega_{\mathbf{K}} d^2\Omega_{\mathbf{K}}} = \frac{\alpha m_e |\mathbf{p}|^2}{(2\pi c)^2} \frac{v^4 e^{\pi v}}{\sinh(\pi v)} \omega_{\mathbf{K}}^4 |\langle \mathcal{R}_{\delta}(\mathbf{p}) \rangle|^2, \quad (3.79)$$

where $\langle \mathcal{R}_{\delta}(\mathbf{p}) \rangle$ is implicitly given by Eq. (3.76). While the above derivations are quite general, our numerical analysis is for certain models of a laser field, that will be specified in the next Section.

3.3 Numerical illustrations

In this Section, we shall present numerical analysis of LARR based on the formulation presented above. Various aspects have been investigated, including Coulomb effects. However, despite the fact that the LARR spectrum is enhanced by the presence of the Coulomb potential we have not observed qualitatively new effects. For this reason, we shall focus in this Section on studying nondipole effects as well as studying the effect of using chirped laser pulses on the LARR spectrum. Moreover, we shall demonstrate the appearance of vortices in the spectrum of emitted photons, as elaborated below.

3.3.1 Nondipole effects in LARR

In this Section, we shall study LARR in the presence of an N_{osc} cycle laser pulse that is linearly polarised. It is defined by the electric field vector $\mathcal{E} = \mathcal{E}(t)\varepsilon$, where

$$\mathcal{E}(t) = \begin{cases} \mathcal{E}\mathcal{N} \sin^2\left(\frac{\omega t}{2N_{\text{osc}}}\right) \sin(\omega t) & \text{if } 0 \leq t \leq T_p, \\ 0 & \text{otherwise,} \end{cases} \quad (3.80)$$

and the polarisation vector is along the x -axis, $\varepsilon = e_x$. Here, ω denotes the carrier frequency so the relation $T_p = 2\pi N_{\text{osc}}/\omega$ holds. Moreover, the parameter \mathcal{N} is adjusted such that

$$\max_{0 \leq t \leq T_p} |\mathcal{E}(t)| = \mathcal{E}, \quad (3.81)$$

meaning that \mathcal{E} is the peak amplitude of the electric field (3.80). Note that for a laser pulse propagating in the direction \mathbf{n} , t in these definitions should be replaced by the retarded time, t_R [Eq. (3.2)]. For numerical illustrations, we consider a three-cycle laser pulse ($N_{\text{osc}} = 3$) of frequency $\omega = 30.1 \text{ eV} = 1.14E_0$ ($\lambda = 40 \text{ nm}$), with the peak amplitude equal to $\mathcal{E} = 10\mathcal{E}_0$. In Fig. 3.1, we have depicted the time-dependence of the electric field $\mathcal{E}(t)$ and the vector potential

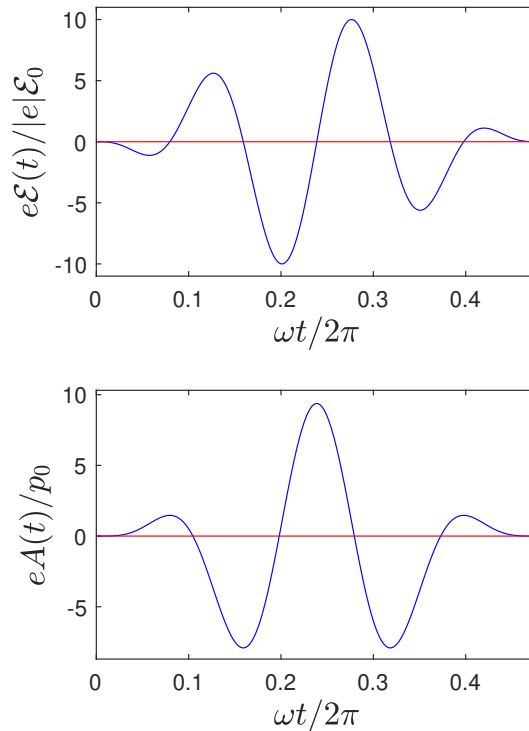


FIGURE 3.1: Shows the electric field $\mathcal{E}(t)$ and the vector potential $A(t)$ corresponding to a laser pulse with a sine-squared envelope [Eq. (3.80)]. The laser field parameters are: $\omega = 30.1$ eV $= 1.14 E_0$ ($\lambda = 40$ nm), $\mathcal{E} = 10\mathcal{E}_0$, and $N_{\text{osc}} = 3$. For a propagating laser pulse, t should be replaced by t_R [Eq. (3.2)].

$A(t) = \int_0^t d\phi \mathcal{E}(\phi)$ corresponding to that pulse. Notably, the condition $\int_{-\infty}^{\infty} dt \mathcal{E}(t) = 0$ ensures that $A(0) = A(T_p) = 0$.

In Fig. 3.2(a), we demonstrate the energy distribution of LARR [Eq. (3.79)], when an electron wave packet collides with a hydrogen-like ion ($Z = 4$) in the presence of a laser field specified above. The electron beam has a well-defined Lorentzian profile (2.63). It is centered at $|\mathbf{p}|$, corresponding to the electron energy $E_p = \frac{p^2}{2m_e} = 10$ keV. Moreover, the longitudinal spread of the Lorentzian distribution is assumed to be $\Delta|\mathbf{p}| = \Delta\sqrt{2m_e E_p} = 10^{-6}\sqrt{2m_e E_p} = 2.74 \times 10^{-5} p_0$. In the following, we consider geometry in which the laser pulse propagates along the z -axis, and is linearly polarised along the x -axis, whereas the electron wave packet propagates in the xz -plane at the polar angle $\theta_p = 0.432\pi$. Moreover, we consider the case when the radiation is emitted in the z -direction, $\mathbf{n}_K = \mathbf{e}_z$, and is linearly polarised along the x -axis, i.e., $\boldsymbol{\epsilon}_K = \mathbf{e}_x$. For this geometry, there is no radiation that would have polarisation transverse to the xz -plane. We observe three distinct plateaus in the energy spectrum presented in Fig. 3.2(a). In addition, we see a laser-field-free peak at the energy around $375E_0 \approx 10.2$ keV. The location of this peak is determined by Eq. (2.44); hence, it originates from a laser-field-free process.

In Fig. 3.2(b), we present a time-frequency analysis of the LARR spectrum that is shown in Fig 3.2(a). This is done by means of a spectrogram, see Appendix A.2. To determine the spectrogram, a given signal is initially truncated using the cutoff function (2.94) within the range $\omega_1 \leq \omega \leq \omega_2$, where $\omega_1 = -5$ a.u. and $\omega_2 = 21.5$ a.u. The truncated signal $\mathcal{A}_T(\omega)$ is defined by Eq. (2.95), where $\zeta_T = 0.1$ is a small parameter. Subsequently, a short-time Fourier transform is applied to the truncated signal [see, Eq. (2.96)] using a window function specified by Eqs. (2.97) and (2.98). Notably, the width of the window function is given by $\zeta_W = 0.03$.

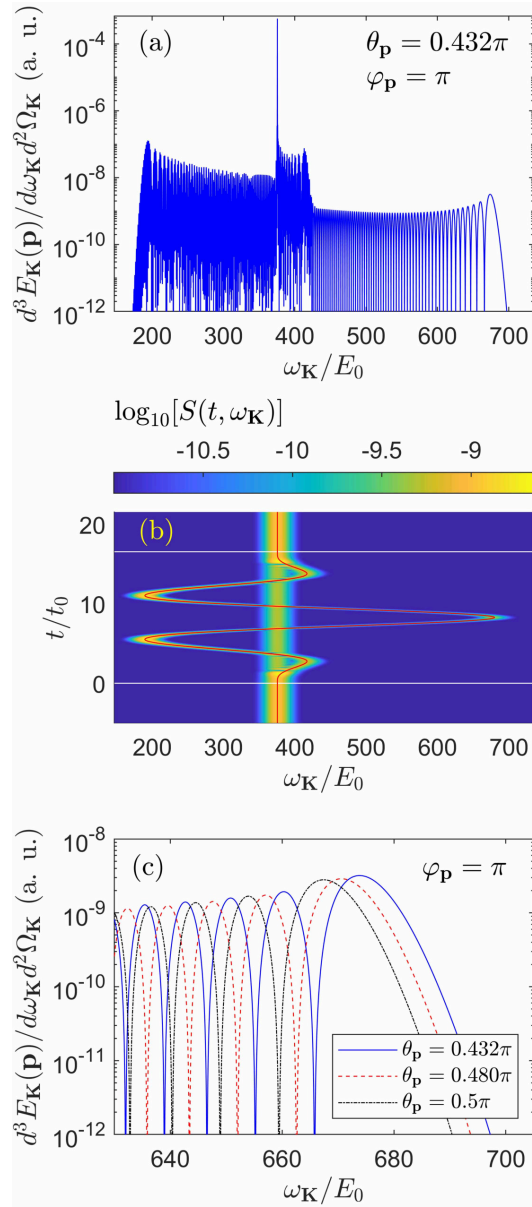


FIGURE 3.2: (a) Energy spectrum of LARR [Eq. (3.79)], when the electron recombines with a hydrogen-like positive ion ($Z = 4$) in the presence of a laser pulse plotted in Fig. 3.1. While the laser pulse propagates in the z -direction and is linearly polarised in the x -direction, the electron wave packet propagates at angles $\theta_{\mathbf{p}} = 0.432\pi$ and $\varphi_{\mathbf{p}} = \pi$. The central momentum of the electron wave packet $|\mathbf{p}|$ corresponds to the energy $E_p = 10$ keV and it has longitudinal spread determined by the parameter $\Delta|\mathbf{p}| = 2.74 \times 10^{-5} p_0$ (for details regarding the electron wave packet, see Section 2.2.2). Together with Coulomb effects, the spectrum comprises of nondipole effects. Note that the emitted radiation propagates along the z -axis, $\mathbf{n}_{\mathbf{K}} = \mathbf{e}_z$, and is polarised along the x -axis, $\boldsymbol{\varepsilon}_{\mathbf{K}} = \mathbf{e}_x$. In this case, there is no radiation with polarisation perpendicular to the xz -plane. (b) Corresponding spectrogram (2.99) (yellow line). The red line represents the temporal behaviour of emitted LARR photons given by $\omega_{\mathbf{K}}(t)$ [Eq. (3.84)]. For spectrograms, we use the Gaussian window (2.97) and the cutoff function (2.94), with the parameters: $\xi_T = 0.1$, $\xi_W = 0.03$, $\omega_1 = -5$ a.u., and $\omega_2 = 21.5$ a.u.. The zigzag yellow line is seen in the spectrogram and it extends for the duration of laser pulse. The straight vertical yellow line in the bottom panel at roughly $375E_0 = 10.2$ keV corresponds to the laser-field-free peak in the spectrum. The white horizontal lines mark the switch on and off the laser pulse. (c) The end portion of the energy spectrum of LARR for different orientations of the electron wave packet, as given in the legend.

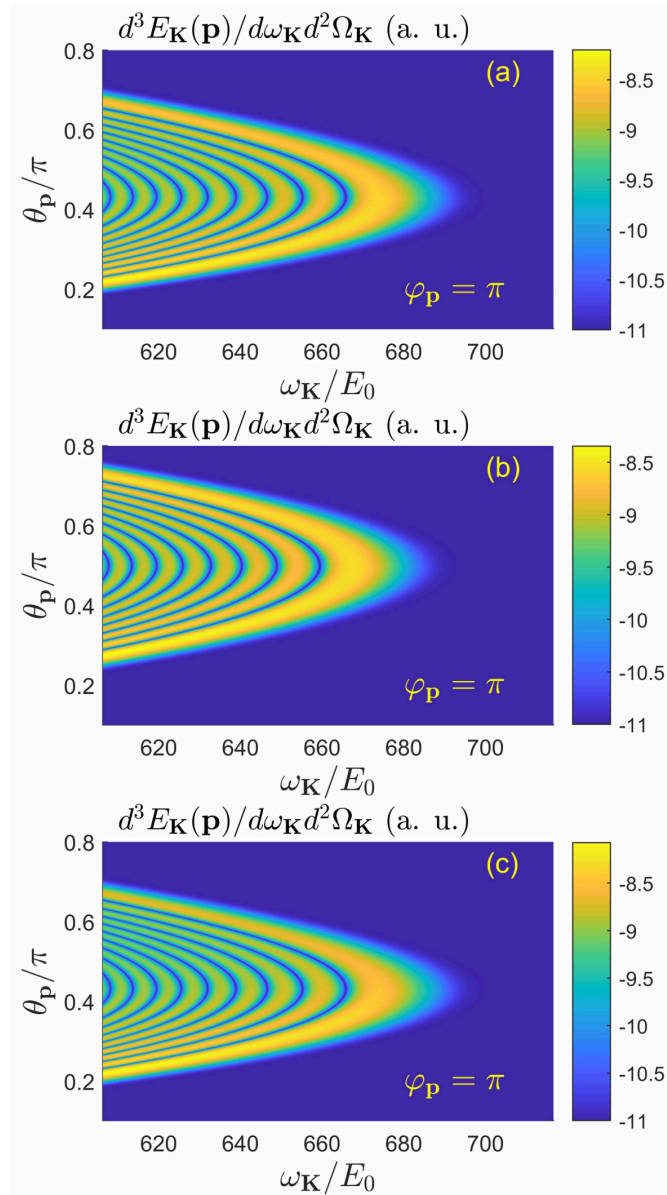


FIGURE 3.3: Energy spectrum of LARR (3.79) in the (θ_p, ω_K) plane for $\varphi_p = \pi$, keeping the laser and the electron wave packet parameters same as in Fig. 3.2, except that now (a) all leading nondipole correction, (b) only retardation correction, (c) only recoil correction are included in our calculations.

Hence, the spectrogram is given by Eq. (2.99). The spectrogram reveals when the given frequency photon is emitted. Since the monochromatic peak at $\omega_K = 375E_0$ corresponds to the laser-field-free process, it appears in the spectrogram as a straight line. Because the recombining electron picks up energy from the laser field, the emitted spectrum is much wider; it spans from roughly $180E_0$ to $700E_0$. It is the zigzag line in the spectrogram that reveals it.

In order to get more insight into the origin of emitted spectrum, we have performed saddle-point analysis of the time-integrals defining the LARR probability amplitude (3.67). The point is that each of those integrals has the following structure,

$$\mathcal{I} = \int_0^{T_p} dt G(t) e^{iS_{\text{eff}}(t)}, \quad (3.82)$$

where $S_{\text{eff}}(t) = Qt + H_{\text{eff}}(t)$ is a rapidly varying function of time. More specifically,

$$S_{\text{eff}}(t) = (E_B + \omega_K - \frac{\mathbf{p}^2}{2m_e})t + \frac{1}{m_e} \left(1 + \frac{\mathbf{n} \cdot \mathbf{p}}{m_e c}\right) \int_0^t d\phi \left[e\mathbf{A}(\phi) \cdot \mathbf{p} - \frac{e^2}{2} \mathbf{A}^2(\phi) \right], \quad (3.83)$$

where we have used Eqs. (2.17) and (3.48). As we have already discussed in Chapter 2, the most essential contribution to the integral representing the LARR probability amplitude comes from saddle points. In our case, they are determined from the condition that $\partial_t S_{\text{eff}}(t) = 0$, leading to

$$\omega_K(t) = \frac{1}{2m_e} [\mathbf{p} - e\mathbf{A}(t)]^2 - E_B - \frac{\mathbf{n} \cdot \mathbf{p}}{m_e^2 c} \left[e\mathbf{A}(t) \cdot \mathbf{p} - \frac{e^2}{2} \mathbf{A}^2(t) \right]. \quad (3.84)$$

This equation defines the temporal energy of the emitted photon when an electron dressed by the laser field recombines with the positive ion. By comparing this formula with Eq. (2.81), that was derived for a short-range atomic potential and disregarding nondipole corrections, we infer that the long-range Coulomb potential should not have a significant qualitative impact on the LARR spectrum. In addition, among leading nondipole corrections that we have derived in Section 3.2.1, it is the recoil correction that appears in Eq. (3.84). Our classical analysis of electron dynamics in the presence of the laser field beyond the dipole approximation also reveals that the most significant contribution to the kinetic energy of an electron comes from the recoil correction [see Appendix B.4]. Thus, we expect that the recoil correction contributes to the LARR spectrum most significantly. Let us note that the behaviour of $\omega_K(t)$ [Eq. (3.84)] is represented by the red curve in Fig. 3.2(b). Most importantly, it agrees very well with the zigzag pattern of spectrogram, that resulted from purely numerical calculations of the LARR energy spectrum [Eq. (3.79)]. Hence, the extend of the LARR energy spectrum and characteristics of its plateau can be interpreted using the saddle point approach. Specifically, the most energetic plateau results from interference of the probability amplitudes at two different times for a particular emitted photon energy, i.e., contribution from two saddle points. This leads to very regular oscillations, as seen from Fig. 3.2(a). The least energetic plateau is formed from four saddle-point contributions whereas the mid-energy plateau from six saddle points. Therefore, the oscillations in those regions are irregular. It appears that the saddle-point interpretation of LARR is well-supported, even when considering the Coulomb interaction and going beyond the dipole approximation. Therefore, it demonstrates the capability of LARR-based metrology, as previously discussed in Chapter 2 in the context of LARA.

In Fig. 3.2(c), we present the end portions of the energy spectrum of LARR at various orientations of the initial electron with respect to the pulse propagation direction, as specified by the electron polar angle θ_p . While the blue solid line corresponds to the same parameters as Fig. 3.2(a), the red dashed line and the black dotted line are for increasingly larger polar angles θ_p , as stated in the legend. As we can see, the plateau cutoff extends towards larger energies with decreasing the angle θ_p . This agrees with Eq. (3.84). Introducing the polar angle θ_p such that $\cos \theta_p = \frac{\mathbf{n} \cdot \mathbf{p}}{|\mathbf{p}|}$, we can rewrite Eq. (3.84) so it reads

$$\omega_K(t) = \frac{\mathbf{p}^2}{2m_e} - E_B + \frac{1}{2m_e} \left(1 + \frac{|\mathbf{p}| \cos \theta_p}{m_e c}\right) \left(e^2 \mathbf{A}^2(t) + 2e|\mathbf{A}(t)| |\mathbf{p}| \sin \theta_p \right). \quad (3.85)$$

It shows that, for as long as we neglect the recoil term, most energetic radiations would be emitted for $\theta_p = \frac{\pi}{2}$. Clearly, this is not the case here. In contrast, for $\theta_p = \frac{\pi}{2}$, we observe the

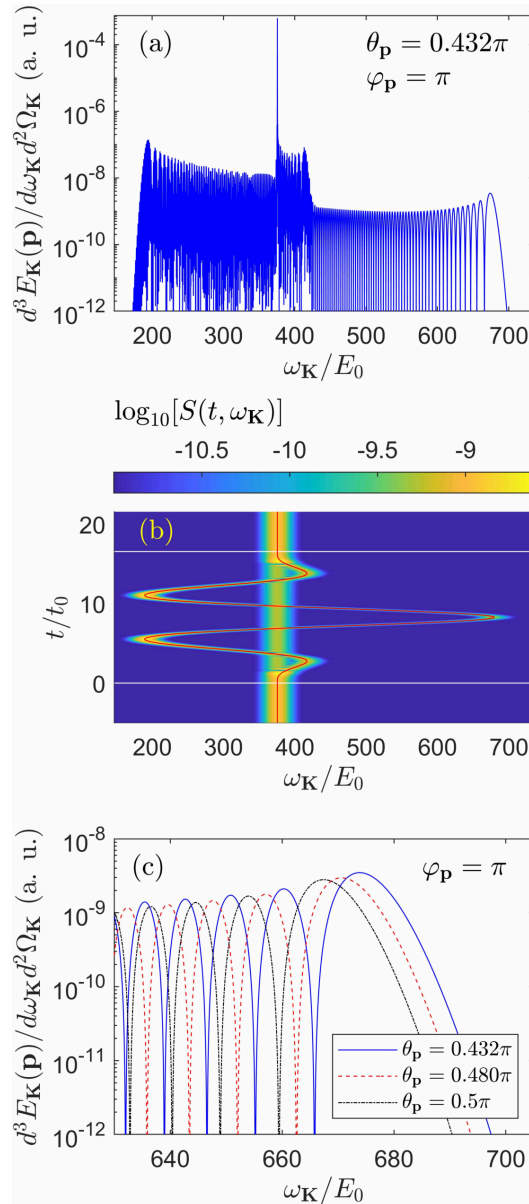


FIGURE 3.4: Same as Fig. 3.2 but for $G_p(t)$ [Eq. (3.46)] equal to 1. Both Figs. 3.2 and 3.4 basically coincide, meaning that the correction coming from the quantised electric field corresponding to the emitted photon has a negligible effect on the energy distribution of LARR.

least energetic radiation. In this case, the electron propagates perpendicularly to the laser pulse and so it does not experience the radiation pressure. That is why the recoil term in Eq. (3.85) vanishes for $\theta_p = \frac{\pi}{2}$. With decreasing θ_p , however, the recoil term increases rapidly enough so it dominates the decreasing term containing $\sin \theta_p$. As a result, the electron propagating at smaller angles will release more energetic radiation. Specifically, for the data plotted in Fig. 3.3(c), a small variation in the polar angle θ_p results in extending the plateau cutoff by roughly 8 a.u. or, equivalently, by roughly 200 eV. Thus, the nondipole effects in LARR are non-negligible and have to be carefully accounted for in light of potential applications.

While in Fig. 3.2(c) we have presented the energy distributions of LARR radiation for chosen values of electron polar angle, in Fig. 3.3 we generalise those results. This time we show the complete polar mappings of the LARR energy distributions close to the cutoff. The mappings

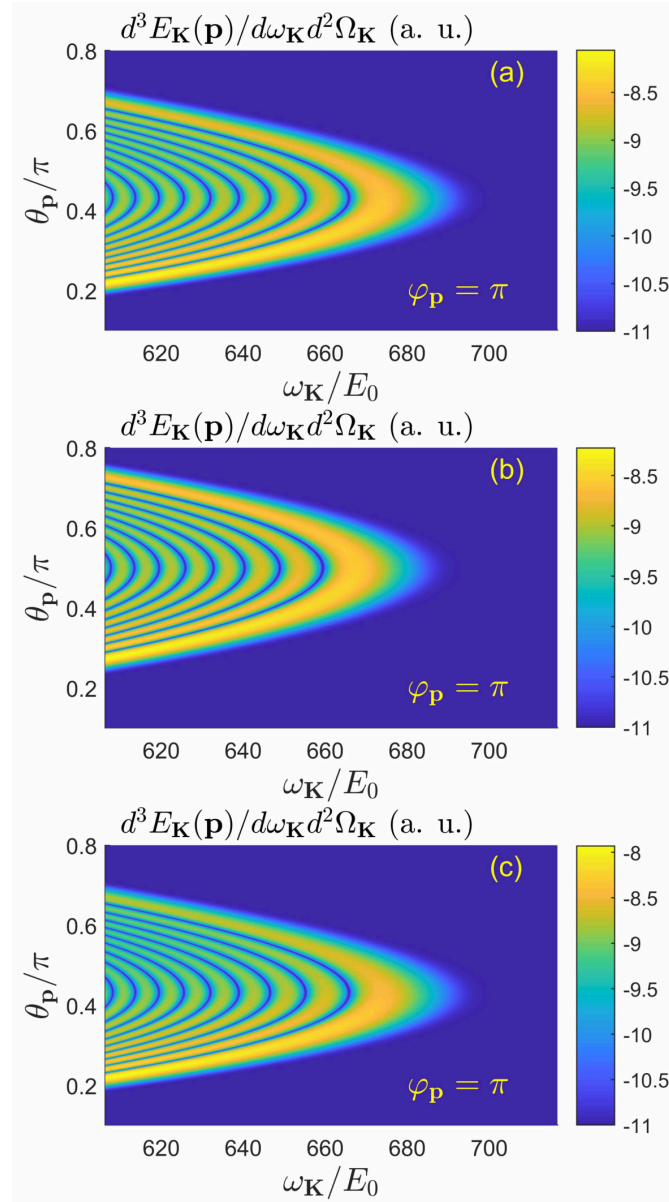


FIGURE 3.5: Same as Fig. 3.3 but for $G_p(t)$ [Eq. (3.46)] equal to 1, i.e., neglecting the $1/c$ contribution to the electron-photon interaction Hamiltonian (3.40).

consist of interference pattern, with strips of small and large probability laying interchangeably. Let us note that the results plotted in panel (a) have been calculated by accounting for all leading nondipole corrections, as introduced in Section 3.2.1. On the other hand, in panels (b) and (c) we present the results with an account for only the retardation or the recoil corrections, respectively. As one can see, panels (a) and (c) show asymmetry around polar angle $\theta_p = \frac{\pi}{2}$, which is not the case in panel (b). This indicates that it is the recoil correction which contributes the most, as it has been already discussed in relation to formulas (3.84) and (3.85). If we disregard the recoil correction, the temporal energy of emitted radiation $\omega_K(t)$ will depend on the electron polar angle as $\sin \theta_p$, being symmetric with respect to $\theta_p = \frac{\pi}{2}$. This explains the behaviour of energy distribution in panel (b). The asymmetry in panel (a) and (c) is therefore caused by radiation pressure that the propagating laser pulse imposes on the electron. This additional momentum transfer from the laser field also explains a shift of the maximum of the

LARR energy distributions towards smaller polar angles.

At this point, we would like to note that in the current formulation of LARR we have used consistently the expansion in $1/c$. This concerns the nondipole corrections arising from the electron-laser-field interaction but also from the electron-photon interaction. To make sure that the observed effects are indeed related to nondipole electron-laser-field interaction, we have performed the same calculations neglecting $1/c$ term in Eq. (3.46) and plotted Figs. 3.4 and 3.5, which are analogs of Figs. 3.2 and 3.3 for $G_p(t) = 1$ [Eq. (3.46)]. We observe marginal difference in the intensity scale when we compare Fig. 3.3 with Fig. 3.5. There is basically no difference between Fig. 3.2 and Fig. 3.4. Therefore, we conclude that the $1/c$ correction to the electron-photon interaction Hamiltonian (3.40) does not play a significant role. This also means that the observed effects are clearly related to nondipole effects originating from the electron interaction with the laser field.

In this Section, we have studied nondipole effects in the laser-assisted radiative recombination. Together with a noticeable asymmetry in the energy-angle distributions of LARR, our studies revealed a way of extending LARR plateau towards higher photon energy. In the next Section, we investigate the possibility of enhancing particular LARR harmonics. This is done by chirping the assisting laser pulse.

3.3.2 LARR in chirped laser pulses

In this Section, we are examining methods to enhance the production of high-energy harmonics in LARR. As previously studied, we can enhance LARR by fine-tuning the laser field parameters such as intensity, number of oscillations, or carrier envelope phase. Our objective is to increase the intensity of high harmonics, by introducing different forms of chirp in the laser field phase. These harmonics are extracted at the edges of the plateau, which is important for applications such as imaging, radiation therapy, spectroscopy, astrophysics, and climate studies [109, 110, 111, 112].

We consider LARR in the presence of a chirped linearly polarised laser pulse, that is described by the vector potential

$$\mathbf{A}(t) = A_0 f_j(t) \boldsymbol{\varepsilon}, \quad j = 1, 2, \quad (3.86)$$

where $\boldsymbol{\varepsilon} = e_x$, whereas the pulse shape is given by either

$$f_1(t) = F(t) \sin[Y(t)], \quad (3.87)$$

or

$$f_2(t) = [f_1(t) + 1]^2 - 1. \quad (3.88)$$

Here,

$$F(t) = \begin{cases} \left[\sin\left(\frac{\omega t}{2N_{\text{osc}}}\right) \right]^{N_{\text{pow}}} & \text{if } 0 \leq t \leq T_p, \\ 0 & \text{otherwise,} \end{cases} \quad (3.89)$$

where N_{osc} stands for the number of cycles in a pulse, $T_p = 2\pi N_{\text{osc}}/\omega$ is a pulse duration, and N_{pow} is a pulse shaping parameter. Moreover, the carrier wave of the pulse, $\sin[Y(t)]$, has

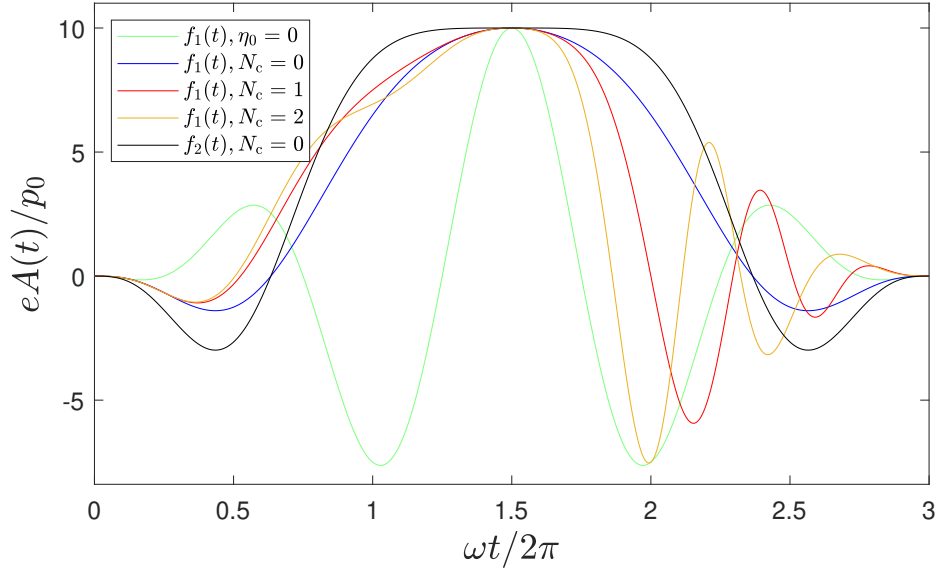


FIGURE 3.6: Comparison between vector potentials of different chirped pulses. As a reference, a pulse without a chirp is plotted in green. It corresponds to the shape function $f_1(t)$ [Eqs. (3.87) and (3.89)] with $\eta_0 = 0$ and $\chi = \frac{\pi}{2}$. The same shape pulses with a linear chirp ($N_c = 0$, blue line), chirp proportional to the amplitude of the field ($N_c = 1$, red line), and chirp proportional to the intensity of the field ($N_c = 2$, yellow line) are presented. In addition, the pulse with a linear chirp for the shape function $f_2(t)$ [Eq. (3.88)] ($N_c = 0$, black line) is shown. For chirped pulses, we keep $\chi = 0$ for $\eta_0 = -\frac{1}{6\pi}$. All examples correspond to $N_{\text{pow}} = 2$, have three cycles ($N_{\text{osc}} = 3$), $\lambda = 40$ nm, and $eA_0 = 10p_0$.

chirped phase defined as

$$Y(t) = \omega t + \chi + \eta_0 \left[F(t) \right]^{N_c} (\omega t)^2, \quad (3.90)$$

where χ is the carrier envelope phase of the pulse, whereas η_0 and N_c define the pulse chirp. As before, one has to remember that for a propagating laser pulse t should be replaced by t_R , Eq. (3.2), in the above definitions.

In Fig. 3.6, we plot the vector potential over time for different chirp types. In general, we use a three-cycle ($N_{\text{osc}} = 3$) laser pulse, with $\lambda = 40$ nm, $eA_0 = 10p_0$, and $N_{\text{pow}} = 2$. For $\chi = -(-1)^{N_{\text{osc}}} \frac{\pi}{2}$, the vector potential with the shape function $f_1(t)$ [Eq. (3.87) and (3.89)] and no chirp ($\eta_0 = 0$) attains a maximum at $t = T_p/2$, as shown in Fig. 3.6. However, when $\eta_0 \neq 0$, it introduces a linear chirp for $N_c = 0$, a chirp that is proportional to the pulse instantaneous amplitude for $N_c = 1$, and to its instantaneous intensity for $N_c = 2$. Additionally, assuming the maxima at $t = T_p/2$ for pulses with a chirp, we obtain $\chi = -(N_{\text{osc}} + 1) \frac{\pi}{2}$ for $\eta_0 = -\frac{1}{2N_{\text{osc}}\pi}$, as shown in Fig. 3.6. Moreover, for such values of χ and η_0 , the shape function $f_2(t)$ [Eq. (3.88)] remains flat in the central region for $N_c = 0$, achieving flatness up to the third order derivative of the function $f_2(t)$ at $t = T_p/2$. Note that when the electron moves in a laser field with a flat top, it absorbs maximum energy from the field over an extended time interval. This will lead to more efficient emission of photons in the high-energy region. Note that, in Ref. [36], the authors demonstrated a similar way to increase the yield of a particular harmonic, i.e., by the flattening of the pulse shape. However, their approach was different from the one presented in this Chapter. In our case, we are considering LARR in the presence of short laser pulses while in Ref. [36], a bichromatic laser field was used. In their approach, the authors manipulated the

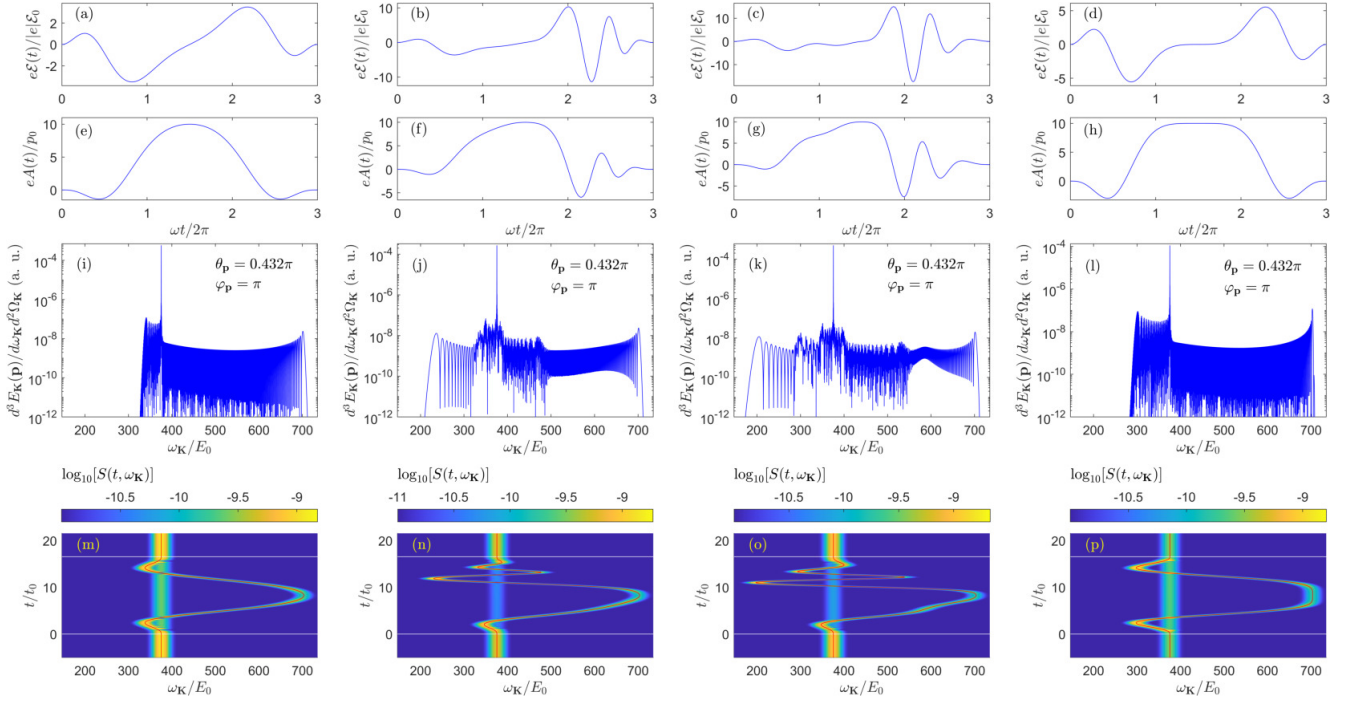


FIGURE 3.7: Energy spectra of LARR (3.79) (third row) and corresponding spectrograms (2.99) (fourth row) when electron recombines with a hydrogen-like ion ($\mathcal{Z} = 4$) in the presence of chirped laser pulses. The laser pulse propagates along the z -axis and is linearly polarised along the x -axis, whereas the electron wave packet propagates in the xz -plane at the polar angle of $\theta_p = 0.432\pi$. For the emitted photon, we assume $n_K = e_z$ and $\varepsilon_K = e_x$. The parameters for the electric field (top row) and the corresponding vector potential (second row) for a different choice of chirped laser pulses for the shape function $f_1(t)$ [Eq. (3.87) and (3.89)] with $N_c = 0$ (first column), $N_c = 1$ (second column), $N_c = 2$ (third column), and by the shape function $f_2(t)$ [Eq. (3.88)] for $N_c = 0$ (fourth column) are the same as in Fig. 3.6. The parameters for spectrogram are kept the same as Fig. 3.2. The red line in the spectrograms follows from the definition of $\omega_K(t)$ which shows the time-dependence of the temporal energy irradiated by a moving electron in a laser field, that is captured by the atom, given by Eq. (3.84). The horizontal white lines mark the beginning and the end of the laser pulses.

phase difference between the bichromatic laser field components to flatten the vector potential. On the other hand, we introduce a chirp in the phase of the vector potential to achieve a similar result. Next, we demonstrate energy distributions and spectrograms for the different pulse choices that we have discussed above.

In Fig. 3.7, we demonstrate the energy spectrum of LARR (3.79) and their corresponding spectrograms (2.99) when the electron beam collides with a hydrogen-like ion ($\mathcal{Z} = 4$) in the presence of various chirped laser pulses, discussed already in Fig. 3.6. To explain the energy spectra, we display $\mathcal{E}(t)$ and the corresponding vector potential $A(t)$ with respect to time for different chirp kinds. When $N_c = 0$, the chirp is linear [see, Fig. 3.7(a) and Fig. 3.7(e)]. When $N_c = 1$, the chirp is proportional to the amplitude of the field [see, Fig. 3.7(b) and Fig. 3.7(f)], and for $N_c = 2$, it is proportional to the intensity of the field [see, Fig. 3.7(c) and Fig. 3.7(g)]. These three cases are considered for the shape function $f_1(t)$ [Eqs. (3.87) and (3.89)]. The remaining column corresponds to the pulse shape $f_2(t)$ [see, Fig. 3.7(d) and Fig. 3.7(h)] with a linear temporal chirp ($N_c = 0$). The electron wave packet has a well-defined Lorentzian profile (2.63). It is centered at $|\mathbf{p}|$, where this central momentum of the electron wave packet \mathbf{p} corresponds to the energy $E_p = 10$ keV. Moreover, the longitudinal spread of the Lorentzian

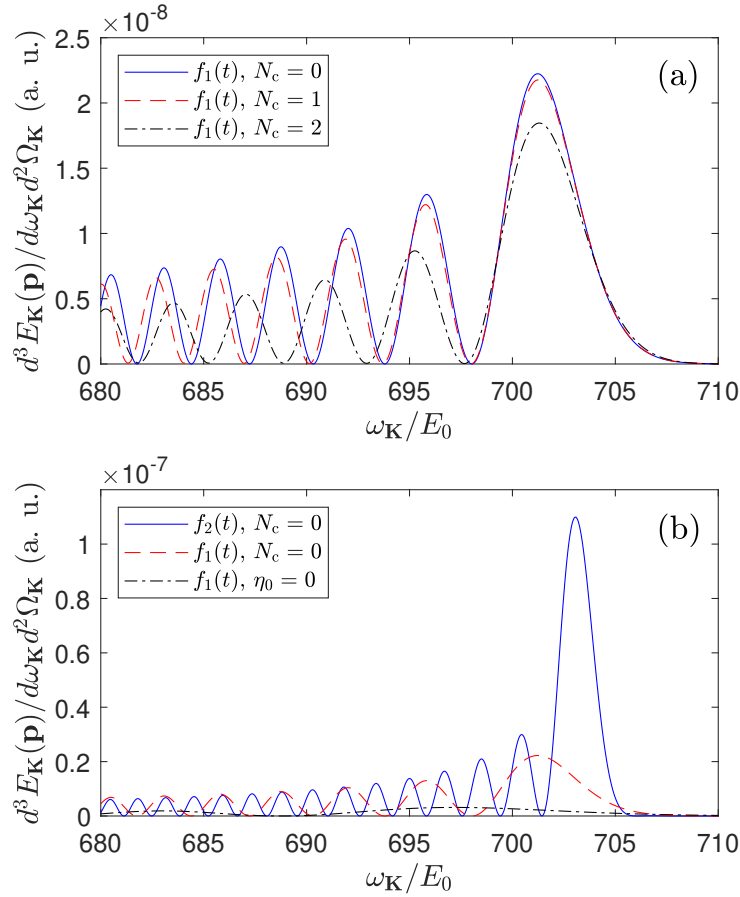


FIGURE 3.8: Comparison between the high-energy end of the spectrum for different laser pulse models, as stated in the legends. The remaining parameters are the same as in Fig. 3.7.

distribution is assumed to be $\Delta|\mathbf{p}| = 2.74 \times 10^{-5} p_0$. We consider geometry such that the laser pulse propagates along the z -axis, it is linearly polarised in the x -direction, whereas the electron wave packet propagates in the xz -plane at the polar angle of $\theta_p = 0.432\pi$. For the emitted photon, we assume $\mathbf{n}_K = \mathbf{e}_z$ and $\boldsymbol{\varepsilon}_K = \mathbf{e}_x$. We note that the end-portions of the LARR energy spectra of the first three columns of Fig. 3.7 are almost of the same magnitude. To have close insight, we plot the comparison of the enlarged portion of spectra near the cutoff of the LARR plateau in Fig. 3.8. We observe that the maximum yield out of the three chirps for shape function $f_1(t)$ [Eq. (3.87) and (3.89)] is gathered when the chirp is linear (solid blue line) and it decreases with the increase in N_c . Nevertheless, the spectrum shown in the last column of Fig. 3.7 is significantly enhanced near the cutoff as compared to the other spectra. To confirm the enhancement, we compare the spectra near the cutoff of the LARR plateau for pulses with linear chirp described by either the shape function $f_2(t)$ (solid blue line), or $f_1(t)$ [Eq. (3.87) and (3.89)] (dash red line), and the pulse with shape function $f_1(t)$ but no chirp ($\eta_0 = 0$). It is clear that the emitted photon intensity is much higher, i.e., almost by an order of magnitude for the shape function $f_2(t)$ [Eq. (3.88)]. This can be explained with the help of Eq. (3.84). We note that, with overall differences, the highest energy photon will be emitted when an electron absorbs maximum energy from the laser field. If the vector potential of the pulse remains constant in time at the peak amplitude of the pulse, then the electron in the strong laser field absorbs energy from the laser field for a longer time. Hence, the emission of photons with higher energies is amplified. This is to be noted that in Ref. [101] we have demonstrated the

results for $\theta_p = \frac{\pi}{2}$, i.e., when there is no electron recoil. The only difference is that the yield of high harmonics increases towards higher energies of emitted photons by roughly 8 a.u. in the current case.

The spectrogram (2.99) in Fig. 3.7 follows the same definition and parameters as in Fig. 3.2, which are also explained in Section. 3.3.1. It is important to observe that all the spectrograms depicted in Fig. 3.7 exhibit a straight yellow line at approximately 375 a.u.= 10.2 keV, representing the laser-field-free radiative recombination. However, the zigzag pattern representing recombination in the presence of the laser field differs in each spectrogram. It is worth mentioning that the signal will vary depending on the type of external laser field used. In our case, we use different kinds of chirps in the laser pulse, which is also reflected in the spectrograms. The red line represents $\omega_K(t)$ [Eq. (3.84)], and it coincides well with the zigzag pattern.

3.3.3 Vortex structures

Vortices have gained attention in scientific research, particularly in the field of strong field ionisation [113,114,115,116,117,118,119,120,121,122,123,124,125,126,127,128,129,130]. However, their study in the context of LARR is yet to be explored. The electron vortices were first discussed theoretically by Dirac [124] in the context of quantum mechanics and later experimentally verified by Vivan [125]. We refer the readers to the textbook by Cieplak *et. al* [107] where the notion of quantum-mechanical vortices is well described. Adapting those definitions and following the ideas presented in Refs. [126,127,128,129,130] for ionisation, we demonstrate below how the vortex structures arises in LARR. A mathematical example of vortices and nodal structures is presented in Appendix B.5. Here, we adapt these notions to describe the structures formed in the probability amplitude of LARR when considered in the parameter space of the emitted photon momentum \mathbf{K} .

Let us consider the situation analyzed in Section 3.3.1. For the parameters chosen there, in Fig. 3.9 we present the angular mappings of the modulus of the probability amplitude, $|\mathcal{A}(\mathbf{p})|$, for emitted LARR photons with energy $\omega_{K,1} = 5275$ eV [panels (a), (b)], $\omega_{K,2} = 10217.5$ eV [panels (c), (d)], and $\omega_{K,3} = 18340$ eV [panels (e), (f)]. The photons are emitted in the direction,

$$\mathbf{n}_K = (\sin \theta_K \cos \varphi_K, \sin \theta_K \sin \varphi_K, \cos \theta_K) \quad (3.91)$$

and they are linearly polarised along either $\boldsymbol{\varepsilon}_{K,1}$ or $\boldsymbol{\varepsilon}_{K,2}$, where

$$\boldsymbol{\varepsilon}_{K,1} = (\cos \theta_K \cos \varphi_K, \cos \theta_K \sin \varphi_K, -\sin \varphi_K), \quad (3.92)$$

$$\boldsymbol{\varepsilon}_{K,2} = (-\sin \varphi_K, \cos \varphi_K, 0). \quad (3.93)$$

Note that all three vectors form an orthogonal triad of unit vectors such that $\boldsymbol{\varepsilon}_{K,1} \times \boldsymbol{\varepsilon}_{K,2} = \mathbf{n}_K$. As one can understand from these definitions, each point in Fig. 3.9 (and in the subsequent figures) corresponds to the photon propagating in a different direction with a different polarisation vector. In each panel, we observe regions with negligible probability of LARR emission. Specifically, there is no photon emission of either energy $\omega_{K,1}$, $\omega_{K,2}$ or $\omega_{K,3}$ with linear polarisation $\boldsymbol{\varepsilon}_{K,2}$ at angles $\varphi_K = 0$ and $\varphi_K = \pi$ (right column). Therefore, one may wonder whether we are dealing here with nodes or vortices. As shown in Fig. 3.10, where we present the phase of the LARR probability amplitude $\arg[\mathcal{A}(\mathbf{p})]$, at $\varphi_K = 0$ and $\varphi_K = \pi$ we must have nodal surfaces. This is because, at those angles, $\arg[\mathcal{A}(\mathbf{p})]$ jumps by π (see, Appendix B.5). In the case shown in the left column of Fig. 3.9, we observe that photons with given energies cannot be emitted in particular directions either. Again, this will correspond to nodal surfaces, although

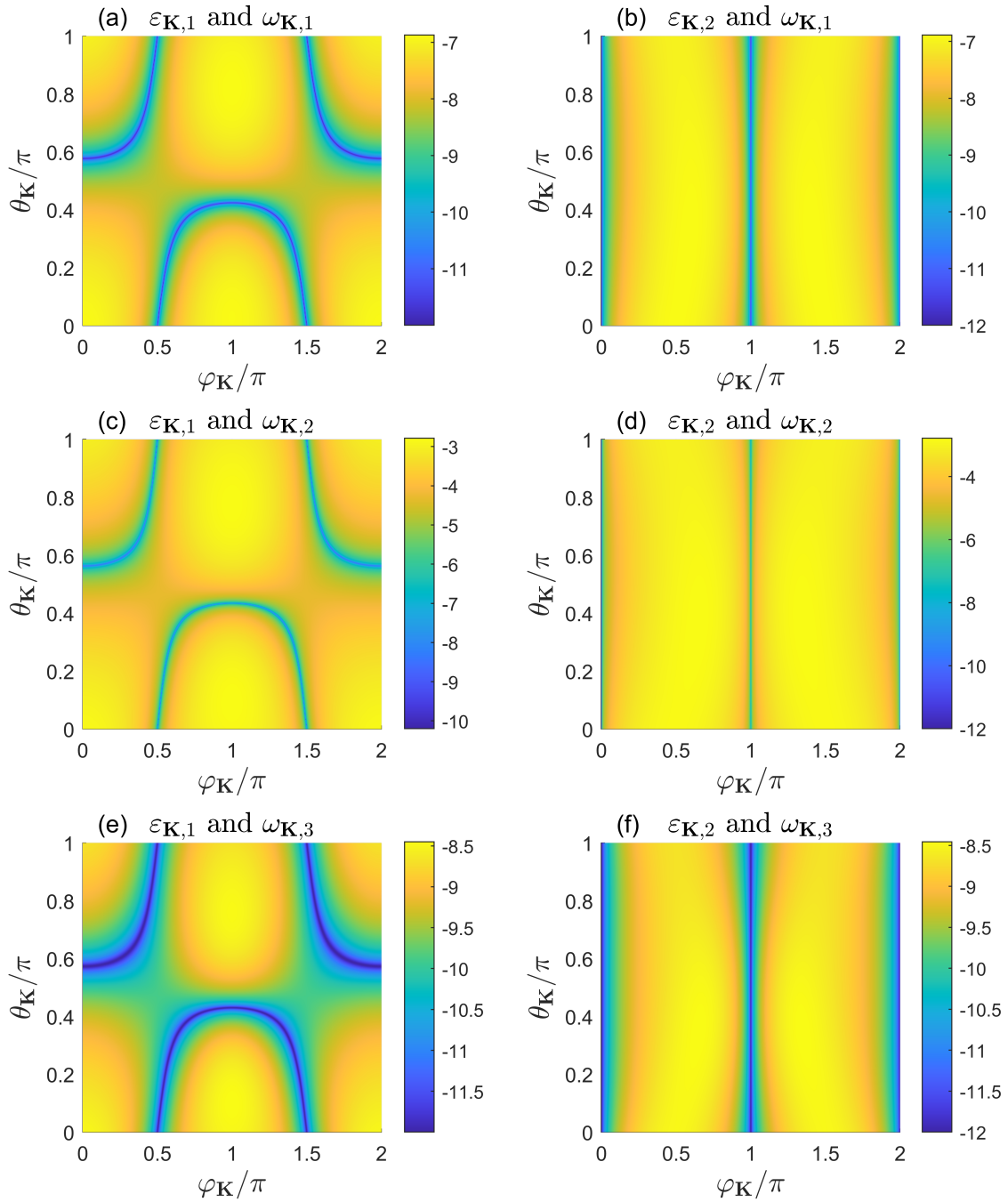


FIGURE 3.9: Angular mappings of the modulus of the LARR probability amplitude, $|\mathcal{A}(\mathbf{p})|$, with respect to the polar and azimuthal photon angles, $\theta_{\mathbf{K}}$ and $\varphi_{\mathbf{K}}$. The same geometry and parameters of the laser pulse and the electron wave packet are considered as in Fig. 3.2(a). The emitted photons are linearly polarised with the polarisation vector $\varepsilon_{\mathbf{K},1}$ [Eq. (3.92), left column] or $\varepsilon_{\mathbf{K},2}$ [Eq. (3.93), right column]. Panels (a) and (b) correspond to the photon energy $\omega_{\mathbf{K},1} = 5275$ eV, panels (c) and (d) are for $\omega_{\mathbf{K},2} = 10217.5$ eV, whereas panels (e) and (f) are for $\omega_{\mathbf{K},3} = 18340$ eV.

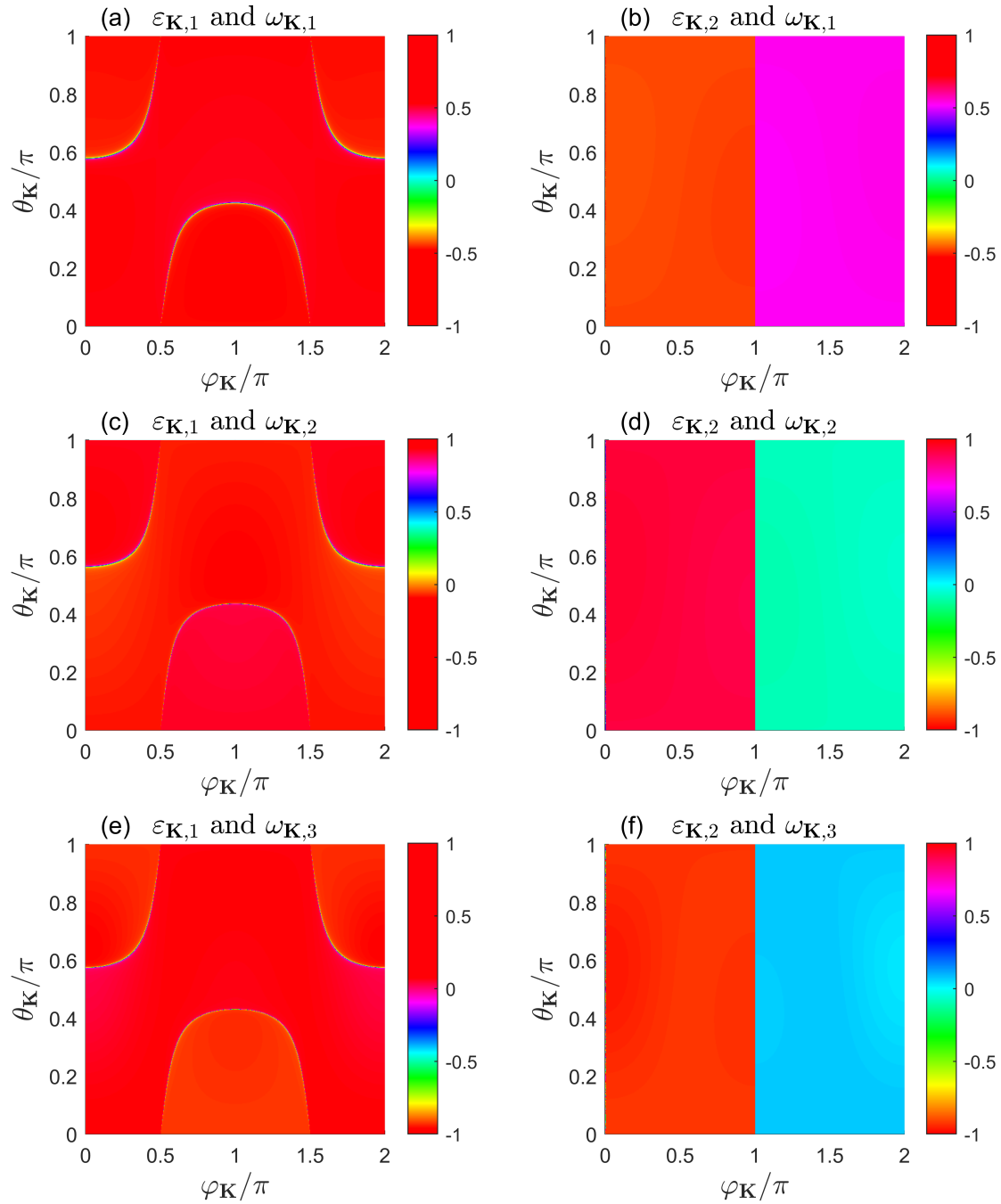


FIGURE 3.10: Color mappings of the LARR probability amplitude phase, $\arg[\mathcal{A}(\mathbf{p})]/\pi$, as a function of the polar and azimuthal photon angles, $\theta_{\mathbf{K}}$ and $\varphi_{\mathbf{K}}$. Each panel has its equivalent panel in Fig. 3.9.

it is difficult to infer this from the left column of Fig. 3.10, due to the color coding. What is important here to note is that, in some directions and regardless of polarisation, photons with energies $\omega_{\mathbf{K},1}$, $\omega_{\mathbf{K},2}$, and $\omega_{\mathbf{K},3}$ cannot be produced at all. This happens when nodal surfaces for both orthogonal linear polarisations intersect each other. The point is that, having known

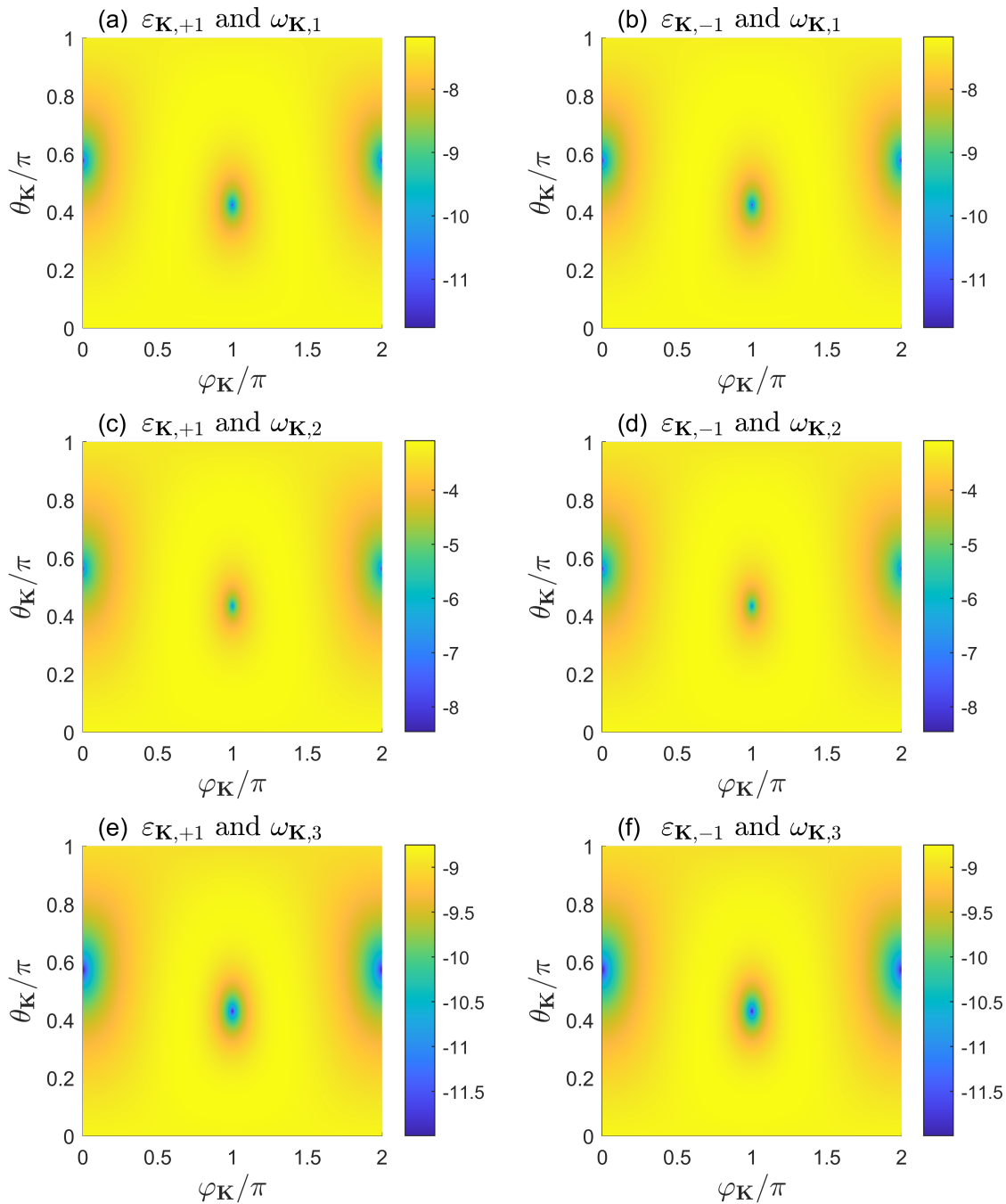


FIGURE 3.11: Same as in Fig. 3.9 except that now the emitted photons are circularly polarised. The left column corresponds to polarisation $\varepsilon_{K,+1}$ [Eq. (3.94)], whereas the right column to polarisation $\varepsilon_{K,-1}$ [Eq. (3.95)].

the LARR probability amplitudes for two linear and orthogonal photon polarisations allows one to calculate the probability amplitude of emitting the photon with an arbitrary, in general, elliptical polarisation. This is illustrated in Figs. 3.11 and 3.12 for circularly polarised photons.

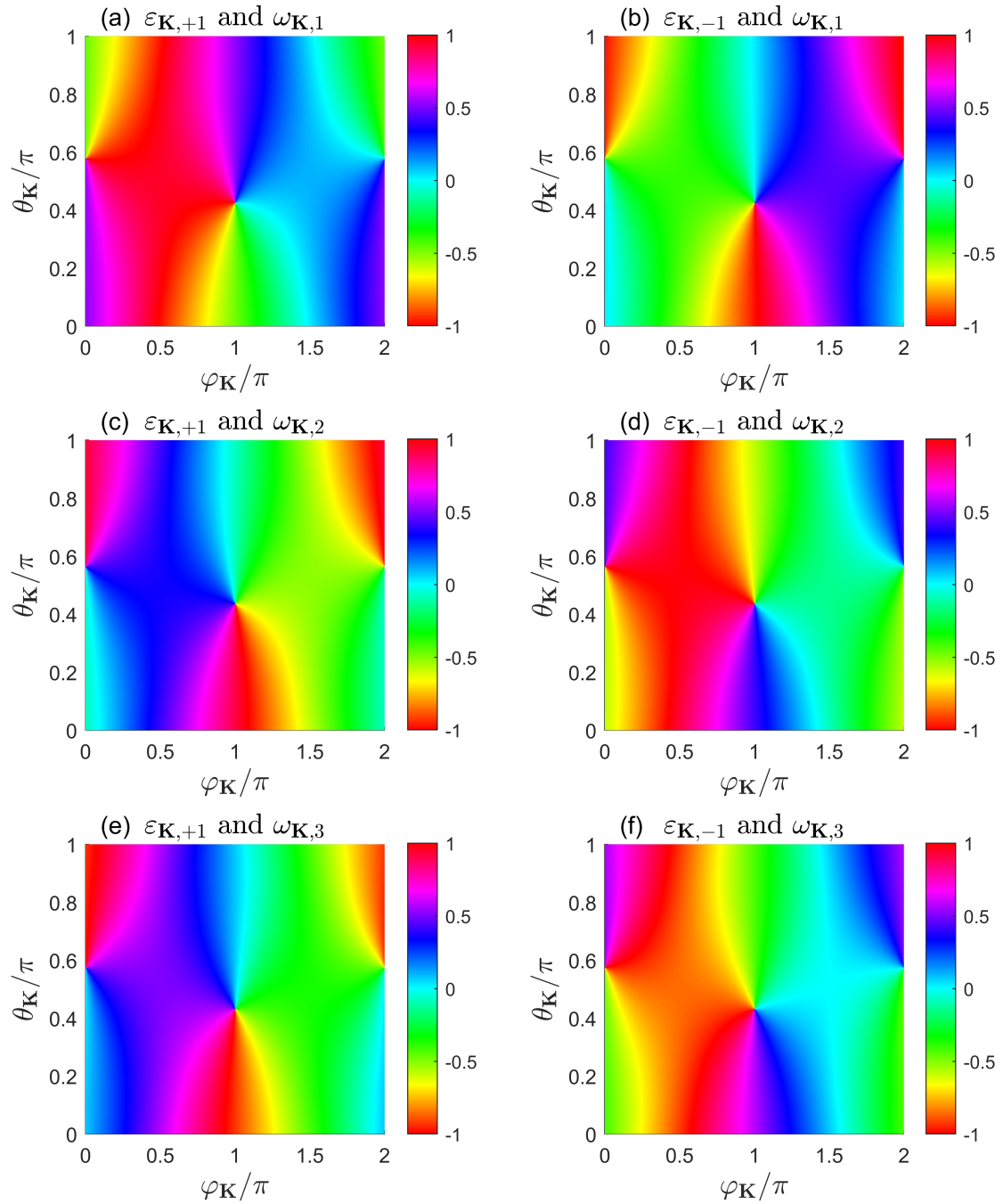


FIGURE 3.12: Color mappings of the LARR probability phase (in units of π) corresponding to Fig. 3.11.

In Figs. 3.11 and 3.12, we present the color mappings for the modulus of the probability amplitude and the probability amplitude phase, respectively, for photons emitted with circular polarisations:

$$\varepsilon_{\mathbf{K},+1} = \frac{1}{\sqrt{2}}(\varepsilon_{\mathbf{K},1} - i\varepsilon_{\mathbf{K},2}) \quad (3.94)$$

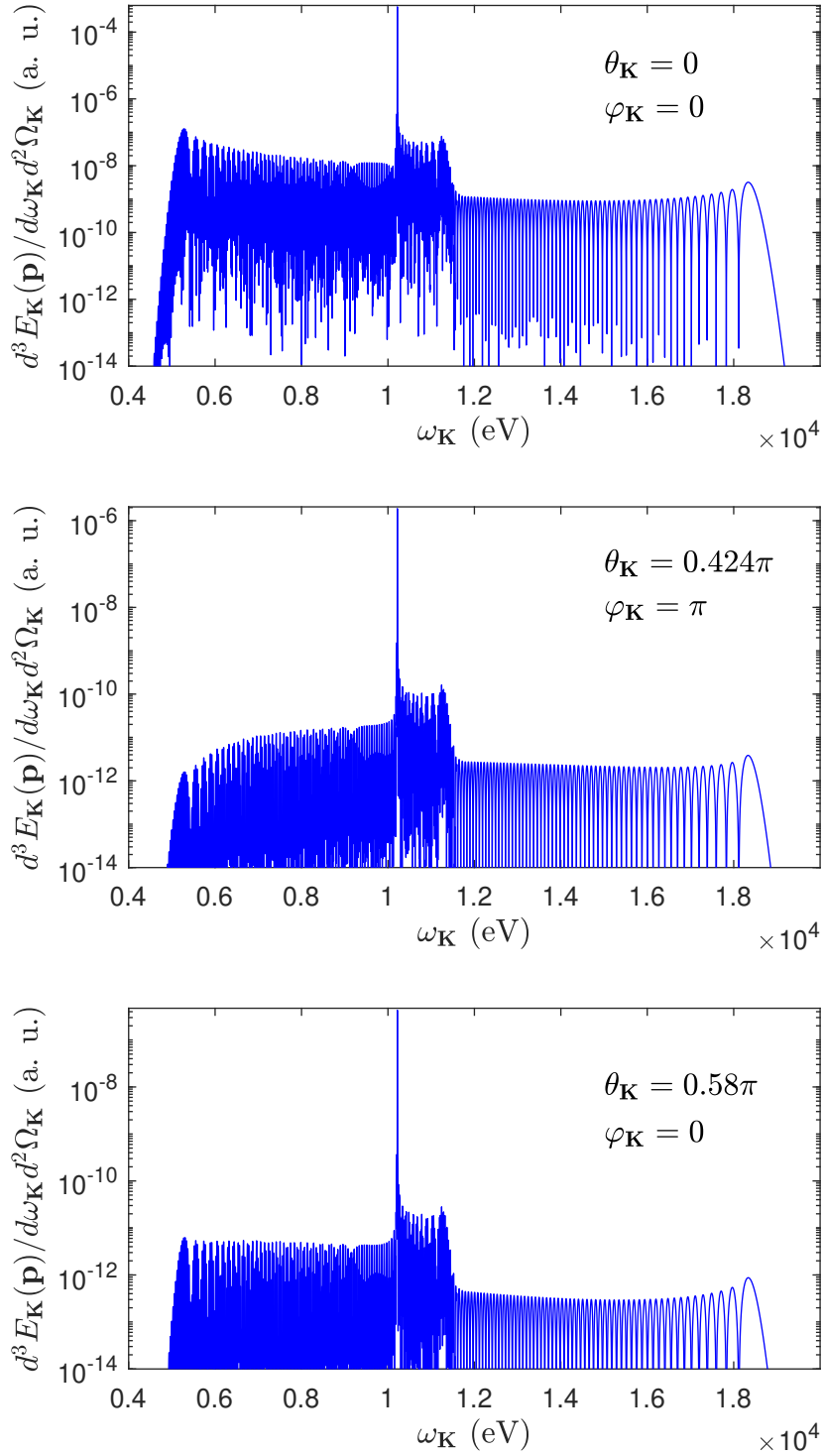


FIGURE 3.13: Energy spectra of linearly polarised radiation emitted in different directions in the xz -plane, as specified in each panel. The parameters characterizing the electron wave packet and the laser pulse are the same as in Fig. 3.2(a). Actually in the top panel here we repeat Fig. 3.2(a). This is contrasted against the other panels, in which the energy spectra of LARR photons are by at least three orders of magnitude smaller than in the top panel. While the presented data are for photons polarised in the xz -plane, in the current geometry there is no emission of radiation polarised perpendicularly to this plane.

in the left column, or

$$\varepsilon_{\mathbf{K},-1} = \frac{1}{\sqrt{2}}(\varepsilon_{\mathbf{K},2} - i\varepsilon_{\mathbf{K},1}) \quad (3.95)$$

in the right column. The remaining parameters are the same as in Figs. 3.9 and 3.10. Specifically, panels (a) and (b) are for the photon energy $\omega_{K,1} = 5275$ eV, panels (c) and (d) are for $\omega_{K,2} = 10217.5$ eV, whereas panels (e) and (f) are for $\omega_{K,3} = 18340$ eV. As one can see in Fig. 3.11, the photon emission is forbidden only in two directions, determined by the angles: $\theta_K = 0.58\pi$, $\varphi_K = 0$ and $\theta_K = 0.424\pi$, $\varphi_K = \pi$. Interestingly, when looking at Fig. 3.12, we observe that at these points the phase of the probability amplitude is not well defined. In fact, in the vicinity of these points, $\arg[\mathcal{A}(p)]$ changes continuously from 0 to 2π , either in the counterclockwise direction (left column) or in the clockwise direction (right column). This corresponds to having vortices with the topological charge of $m = +1$ (left column) and $m = -1$ (right column), as explained in Appendix B.5. We also mention that the position of these vortices seems to be independent of the photon energy. This is confirmed by Fig. 3.13. Finally, we would like to note that for other ellipticities of emitted photons we would observe the isolated vortices at the exact same energies and directions.

While in Fig. 3.9 we presented the angular distributions of linearly polarised photons with fixed energies, in Fig. 3.13 we present the energy distributions of linearly polarised photons emitted in the fixed directions. The remaining parameters are the same in both figures. The directions of photon emission are specified by the angles θ_K and φ_K , which are indicated in each panel of Fig. 3.13. Moreover, each panel is for polarisation $\varepsilon_{K,1}$. Note that for the geometry considered here, the polarisation vectors $\varepsilon_{K,1}$ are in the xz plane, and there is no emission of photons with the polarisation vector perpendicular to this plane, $\varepsilon_{K,2}$. In the current case, we observe that the spectra in the middle and bottom panels are by at least three orders of magnitude smaller than the one in the top panel. In other words, they are practically zero. Importantly, this holds for the entire range of photon energies. Therefore, we confirmed numerically that for linearly polarised photons we deal here with nodal surfaces. Since the photon emission with polarisation $\varepsilon_{K,2}$ does not occur, at the same time Fig. 3.13 represents the spectra for an arbitrary elliptical polarisation (up to the scalar product of the linear and elliptical polarisations squared). Specifically, these spectra refer to the circularly polarised photons, similar to Figs. 3.11 and 3.12. In this case, we conclude that for an elliptically polarised photons (with ellipticity parameter $\delta \neq 0$) we deal with isolated vortex half-lines.

3.4 Summary

In this Chapter, we provided a detailed theoretical explanation of LARR that goes beyond the dipole approximation [101]. Although ionisation beyond the dipole approximation in the presence of a strong laser field is a well-studied phenomenon [81, 82, 83, 84, 86, 87, 88, 89, 90, 91, 92, 93, 94, 95], it has not been studied extensively in the context of LARR prior to our work [101].

In Section 3.3.1, we presented the energy distribution and spectrogram for LARR, which takes into account nondipole effects like retardation and recoil. This leads to an extension of the LARR plateau towards higher photon energies. We found that the recoil effect contributes significantly to this extension, as shown in Eq. (3.84). Additionally, we noticed a shift in the angular distribution of LARR with respect to the electron polar angle $\theta_p = \frac{\pi}{2}$, which is also caused by the recoil effect, as illustrated in Fig. 3.3.

Additionally, we explored a method to improve high harmonics yield in the LARR energy spectrum. This method involves chirping the accompanying laser pulse. With an appropriately chosen chirp, the electron in the laser field absorbs energy from the laser field for an extended time duration. This results in an enhanced yield of emitted photons, especially at both ends of the spectrum (see Fig. 3.7). This method differs from the one presented in Ref. [36], where

the phase difference between bichromatic fields is adjusted to increase the intensity of high harmonics. We conclude this Chapter by demonstrating the appearance of vortex structures in the probability amplitude of LARR.

Chapter 4

Conclusions

This thesis is devoted to radiative recombination in the presence of short laser pulses, that leads to the generation of high-energy photons. It provides a new theoretical approach to describe the process, considering a finite pulse duration. Various aspects of LARR are then analyzed, indicating ways to control the LARR radiation with external laser fields.

Our theoretical formulation of LARR simultaneously refines existing theories of LARR (see, e.g., Refs. [56, 57, 58, 59, 60, 61]) by removing unphysical oscillations in the energy distribution of LARR. These unphysical oscillations, also known as the Gibbs effect, arise by limiting the probability amplitude integral to the duration of the laser pulse. As we argue, this is not justified for radiative recombination when accompanied by a laser pulse. Another aspect that has been shown is that, for finite laser pulses, there is a chance for the electron to emit radiation while recombining with the ion before the pulse arrives or after the pulse is gone. The reason being that the radiative recombination does occur, in principle, in the absence of the field (see, Appendix B in Ref. [79], where the laser-field-free probability amplitude of radiative recombination is derived). Therefore, the probability amplitude of LARR, while assisted by a finite-in-time laser pulse, contains the laser-field-free contribution as well. This seems to be overlooked in the literature prior to our works [79, 101].

A key aspect of this thesis focuses on enhancing the characteristics of the energy distribution of LARR using an external laser field. Notably, as the number of pulses N_{rep} in a laser pulse train increases, we observe a coherent enhancement in the energy distribution of irradiated photons, scaling by a factor of N_{rep}^2 . We have theoretically demonstrated that this enhancement results from the constructive interference of probability amplitudes of recombination accompanied by each pulse in the train. Another way to boost the high harmonic yield of LARR, particularly at the high-energy cutoff, is by optimizing the electron energy absorption from the laser field. We have accomplished this by chirping the laser pulse.

We have also observed an extension of the LARR plateau when accounting for nondipole corrections in our theoretical formulation of LARR. We have discovered that the nondipole corrections arise from three different origins: the gauge transformation correction, the retardation correction, and the recoil correction. The first two nondipole corrections stem from the dependence of the laser field on the retarded time. The final correction arises when we consider the radiation pressure of the laser field, imparted on the electron. As we demonstrate, the primary reason for the extension of the LARR plateau is the recoil correction. These enhancements are of great practical importance. Specifically, longer energy ranges are capable of producing shorter pulses.

As we have shown in the thesis, the recoil effect also introduces asymmetries in the angular distribution of LARR. We can justify the extension of LARR plateau and asymmetry in the angular distribution of LARR using Eq. (3.84). It defines the temporal energy of the emitted

photon when an electron dressed by the laser field recombines with a positive ion. Subsequently, changes in the geometry of the propagation direction of the laser field and the electron wave packet impact the range of the LARR plateau and cause asymmetries in the angular distribution. Moreover, comparing Eq. (3.84) with Eq. (2.81), which was derived for a short-range atomic potential and disregarding nondipole corrections, we infer that long-range Coulomb potential should not have a significant qualitative impact on the LARR spectrum.

Furthermore, we have demonstrated the spectrogram (or time-frequency) analysis for both cases, i.e., when the radiative recombination is accompanied by an isolated pulse or a pulse train. Note that the spectrogram analysis aligns with our comprehensive framework of LARR, as it takes into account contributions from both laser-field-free and laser-field-modified recombination. Furthermore, we have revealed the presence of the Gibbs effect in the spectrogram analysis of previous theories. Our rigorous theory successfully addresses and eliminates this effect. Finally, we have shown that the vector potential describing the laser field is encoded in the spectrogram of LARR radiation. This suggests using spectrograms for a complete temporal reconstruction of the laser field, irrespective of whether it is an isolated pulse or a pulse train. Hence, making it a useful tool for laser-pulse diagnostics. Moreover, the spectrogram analysis of LARR has proven to be universal, as it is also consistent with our theoretical investigation of the process beyond the dipole approximation.

In the end, we have explored angular maps of the LARR probability amplitude in the momentum space of generated photons. We have demonstrated examples of nodal surfaces and isolated vortex half-lines along which the emission of radiation is not possible. This, of course, may have important practical implications.

Finally, while the thesis presents various aspects related to laser-assisted radiative recombination in short laser pulses, we believe that some of our results can be generalized. Specifically, our theoretical method can be adapted to describe other laser-assisted processes accompanied by short laser pulses. Thus, we expect that similar features such as a laser-field-free peak should be also observed there. Another aspect which seems to be universal is the analysis performed in Section 3.2.1, where we have derived the Coulomb-Volkov scattering state with leading nondipole corrections. Also, our analysis of the Nordsieck integral with a detailed explanation of how to calculate the respective contributions to the LARR probability amplitude can serve as an example for other investigations of laser-assisted processes in a Coulomb field. We hope, therefore, that the results collected during the realization of this thesis can become useful not only in the context of LARR but, more generally, in the context of strong-field physics phenomena.

Appendix A

Supplementary materials for Chapter 2

A.1 Alternative derivation of $\langle \delta(Q) \rangle$ and $\langle \mathcal{P}(\frac{1}{Q}) \rangle$

The purpose of this Section is to present an alternative derivation of Eqs. (2.68) and (2.75). They define the electron-wave-packet-averaged distributions that we deal with in our rigorous treatment of laser-assisted radiative recombination. We start with Eq. (2.71) that we repeat below for the convenience of the reader,

$$\langle \frac{1}{Q + i\epsilon} \rangle = \frac{2m_e}{\pi} \int_{-\infty}^{+\infty} dq_{\parallel} \frac{1}{q_0^2 - q_{\parallel}^2 + i\epsilon} \frac{\Delta|\mathbf{p}|}{(q_{\parallel} - |\mathbf{p}|)^2 + (\Delta|\mathbf{p}|)^2}. \quad (\text{A.1})$$

Let us consider $q_{\parallel} = |\mathbf{p}| + \beta$. It implies $dq_{\parallel} = d\beta$ for fixed $|\mathbf{p}|$. Writing Eq. (A.1) in terms of β , we have

$$\langle \frac{1}{Q + i\epsilon} \rangle = \frac{2m_e}{\pi} \int_{-\infty}^{+\infty} d\beta \frac{1}{q_0^2 - (|\mathbf{p}| + \beta)^2 + i\epsilon} \frac{\Delta|\mathbf{p}|}{\beta^2 + (\Delta|\mathbf{p}|)^2}. \quad (\text{A.2})$$

For small β ,

$$\langle \frac{1}{Q + i\epsilon} \rangle \approx \frac{2m_e}{\pi} \int_{-\infty}^{+\infty} d\beta \frac{1}{q_0^2 - \mathbf{p}^2 - 2\beta|\mathbf{p}| + i\epsilon} \frac{\Delta|\mathbf{p}|}{\beta^2 + (\Delta|\mathbf{p}|)^2}. \quad (\text{A.3})$$

We calculate this integral using the Cauchy residue theorem. For this purpose we close the integration contour in the upper half-plane with a semicircle. In this case, the contour encircles two poles, $\beta = \frac{q_0^2 - |\mathbf{p}|^2}{2|\mathbf{p}|} + i\epsilon$ and $\beta = i\Delta|\mathbf{p}|$, which leads to

$$\langle \frac{1}{Q + i\epsilon} \rangle = 2m_e \left[\frac{1}{q_0^2 - \mathbf{p}^2 - 2i|\mathbf{p}|\Delta|\mathbf{p}|} - i \frac{4|\mathbf{p}|\Delta|\mathbf{p}|}{(q_0^2 - \mathbf{p}^2)^2 + (2|\mathbf{p}|\Delta|\mathbf{p}|)^2} \right]. \quad (\text{A.4})$$

Decomposing the second term into simple fractions, we obtain that Eq. (A.4) simplifies to

$$\langle \frac{1}{Q + i\epsilon} \rangle = \frac{2m_e}{q_0^2 - \mathbf{p}^2 + 2i|\mathbf{p}|\Delta|\mathbf{p}|}. \quad (\text{A.5})$$

When we close the integration contour with a semicircle in the lower half-plane, there is one pole $\beta = -i\Delta|\mathbf{p}|$. As we have checked, this leads to the same result as Eq. (A.5). This can be

further represented as

$$\left\langle \frac{1}{Q + i\epsilon} \right\rangle = -2i\pi \langle \delta(Q) \rangle + \frac{2m_e}{q_0^2 - \mathbf{p}^2 - 2i|\mathbf{p}|\Delta|\mathbf{p}|}. \quad (\text{A.6})$$

Taking Sokhotski-Plemelj formula [68], we can write that

$$\left\langle \frac{1}{Q + i\epsilon} \right\rangle = \left\langle \mathcal{P} \left(\frac{1}{Q} \right) \right\rangle - i\pi \langle \delta(Q) \rangle. \quad (\text{A.7})$$

Hence, we have

$$\left\langle \mathcal{P} \left(\frac{1}{Q} \right) \right\rangle = 2m_e \frac{q_0^2 - |\mathbf{p}|^2}{(q_0^2 - \mathbf{p}^2)^2 + (2|\mathbf{p}|\Delta|\mathbf{p}|)^2} \quad (\text{A.8})$$

and

$$\langle \delta(Q) \rangle = \frac{4m_e}{\pi} \frac{|\mathbf{p}|\Delta|\mathbf{p}|}{(q_0^2 - \mathbf{p}^2)^2 + (2|\mathbf{p}|\Delta|\mathbf{p}|)^2}. \quad (\text{A.9})$$

Considering that $q_0 \approx |\mathbf{p}|$, we have $q_0^2 - \mathbf{p}^2 = (q_0 - |\mathbf{p}|)(q_0 + |\mathbf{p}|) \approx 2|\mathbf{p}|(q_0 - |\mathbf{p}|)$. Thus,

$$\left\langle \mathcal{P} \left(\frac{1}{Q} \right) \right\rangle \approx \frac{m_e}{q_0} \frac{q_0 - |\mathbf{p}|}{(q_0 - |\mathbf{p}|)^2 + (\Delta|\mathbf{p}|)^2} \quad (\text{A.10})$$

and

$$\langle \delta(Q) \rangle \approx \frac{m_e}{\pi q_0} \frac{\Delta|\mathbf{p}|}{(q_0 - |\mathbf{p}|)^2 + (\Delta|\mathbf{p}|)^2}, \quad (\text{A.11})$$

which are the same as Eqs. (2.68) and (2.75).

A.2 Spectrogram

A.2.1 Definition, properties, and method of calculating the spectrogram

The function that we call the spectrogram of a certain signal is closely related to a Fourier transform. Since the definition of a Fourier transform depends on the domain in which it is used, we should first define what we mean by a Fourier transform. Our analysis will concern quantum processes, so our definition of Fourier transforms should follow the convention used in quantum theories. In quantum theories, other definitions of the Fourier transform are used for position- and time-dependent functions. Namely,

$$\tilde{f}(p) = \int dx f(x) e^{-ipx} \quad (\text{A.12})$$

and

$$\tilde{f}(\omega) = \int dt f(t) e^{i\omega t}, \quad (\text{A.13})$$

whereas the inverse Fourier transforms have the form,

$$f(x) = \int \frac{dp}{2\pi} \tilde{f}(p) e^{ipx}, \quad (\text{A.14})$$

$$f(t) = \int \frac{d\omega}{2\pi} \tilde{f}(\omega) e^{-i\omega t}. \quad (\text{A.15})$$

This choice is related to the fact that for such definitions and in units $\hbar = 1$, p corresponds to the momentum of a particle and ω to its energy. That is, if $f(x)$ is the probability amplitude of finding the particle at position x , normalized so that

$$\int dx |f(x)|^2 = 1, \quad (\text{A.16})$$

then $\tilde{f}(p)$ is the probability amplitude of finding the particle with momentum p , normalized according to

$$\int \frac{dp}{2\pi} |\tilde{f}(p)|^2 = 1. \quad (\text{A.17})$$

Similar formulation for time-frequency variables can be introduced. If, as a result of some quantum process, the energy distribution is given by the function $\tilde{f}(\omega)$, i.e., the probability of observing a quantum transition with an energy in the interval $[\omega, \omega + d\omega]$ is

$$dP(\omega) = \frac{d\omega}{2\pi} |\tilde{f}(\omega)|^2, \quad (\text{A.18})$$

then the probability of observing this transition in time $[t, t + dt]$ becomes

$$dP(t) = dt |f(t)|^2. \quad (\text{A.19})$$

By Parseval's theorem, the total probabilities in both cases are the same, i.e.,

$$\int dt |f(t)|^2 = \int \frac{d\omega}{2\pi} |\tilde{f}(\omega)|^2. \quad (\text{A.20})$$

Let us introduce the Fourier transform operator, $\hat{\mathcal{F}}_s$, with $s = \pm 1$, taking into account both options,

$$(\hat{\mathcal{F}}_s f)(v) = \int du f(u) e^{isuv} = \tilde{f}_s(v), \quad (\text{A.21})$$

where u and v are real numbers and $f(u)$ is a complex function. Of course,

$$(\hat{\mathcal{F}}_s^{-1} \tilde{f})(u) = \int \frac{dv}{2\pi} \tilde{f}_s(v) e^{-isuv} = f(u), \quad (\text{A.22})$$

that is, formally,

$$\hat{\mathcal{F}}_s^{-1} = \frac{\hat{\mathcal{F}}_{-s}}{2\pi}. \quad (\text{A.23})$$

Next, we define the windowed Fourier transform, $\hat{\mathcal{F}}_s[W]$, by

$$\tilde{f}_s[v, w|W] = (\hat{\mathcal{F}}_s[W]f)(v, w) = \int du f(u)W(w-u)e^{isuv}. \quad (\text{A.24})$$

This transform has the following properties:

- If $W(u) = \delta(u)$, then

$$\tilde{f}_s[v, w|\delta] = \int du f(u)\delta(w-u)e^{isuv} = f(w)e^{iswv}. \quad (\text{A.25})$$

- If $W(u) = \frac{1}{2\pi}$, then

$$\tilde{f}_s[v, w|\frac{1}{2\pi}] = \int \frac{du}{2\pi} f(u)e^{isuv} = \tilde{f}_s(v). \quad (\text{A.26})$$

That is, in these special cases:

- $|\tilde{f}_s[v, w|\delta]| = |f(w)|$ recreates module of the input signal,
- $\tilde{f}_s[v, w|\frac{1}{2\pi}] = \tilde{f}_s(v)$ is a Fourier transform of the input signal.

Now, we define the spectrogram:

$$\mathcal{S}_s[v, w|W] = |\tilde{f}_s[v, w|W]|^2, \quad (\text{A.27})$$

with properties

$$\mathcal{S}_s[v, w|\delta] = |f(w)|^2, \quad (\text{A.28})$$

$$\mathcal{S}_s[v, w|\frac{1}{2\pi}] = |\tilde{f}_s(v)|^2. \quad (\text{A.29})$$

In the special case when $f(u)$ is the amplitude $\mathcal{A}(v)$, u and w are replaced by frequency v and ω , respectively, whereas v is replaced by time t ,

$$\tilde{\mathcal{A}}_s[t, \omega|W] = \int dv \mathcal{A}(v)W(\omega-v)e^{isvt} \quad (\text{A.30})$$

and, specifically,

$$\tilde{\mathcal{A}}_s[t, \omega|\frac{1}{2\pi}] = \int \frac{dv}{2\pi} \mathcal{A}(v)e^{isvt} = \tilde{\mathcal{A}}_s(t). \quad (\text{A.31})$$

Hence, we reproduce the time amplitude $\tilde{\mathcal{A}}(t)$ by choosing $s = -1$. Thus, for the time-frequency analysis, we define the spectrogram by selecting $s = -1$,

$$\mathcal{S}[t, \omega|W] = \mathcal{S}_-[t, \omega|W] = |\tilde{\mathcal{A}}[t, \omega|W]|^2, \quad (\text{A.32})$$

$$\tilde{\mathcal{A}}[t, \omega|W] = \int dv \mathcal{A}(v)W(\omega-v)e^{-ivt}, \quad (\text{A.33})$$

which is consistent with Eq. (2.96).

Let us go back to the original integral (A.24), which we denote by the symbol

$$T(v, w) = \int du f(u) W(w - u) e^{isu v}. \quad (\text{A.34})$$

In order to calculate the above integral, we will demand from function $f(u)$ that it has a finite support, i.e., $f(u) = 0$ for $u \notin [u_1, u_2]$. This allows us to write that

$$T(v, w) = \int_{u_1}^{u_2} du f(u) W(w - u) e^{isu v}. \quad (\text{A.35})$$

Numerical computation of this integral for many values of v and w takes a long time, so it is convenient to express it in the form,

$$T(v, w) = e^{iswv} \int_{u_1}^{u_2} du f(u) W(w - u) e^{-is(w-u)v}. \quad (\text{A.36})$$

Defining

$$g_v(z) = W(z) e^{-iszv}, \quad \text{where } z \in \mathbb{R}, \quad (\text{A.37})$$

Eq. (A.36) can be written in the form,

$$T(v, w) = e^{iswv} \int_{u_1}^{u_2} du f(u) g_v(w - u). \quad (\text{A.38})$$

This means that T is proportional to the convolution of functions f and g_v ,

$$T(v, w) = e^{iswv} (f * g_v)(w) \quad (\text{A.39})$$

and

$$|T(v, w)| = |(f * g_v)(w)|. \quad (\text{A.40})$$

Thus, in order to calculate the spectrogram, we set the value of v and compute the convolution of the functions $f(u)$ and $g_v(u)$.

It is known that the convolution of functions is most conveniently calculated using the Fourier transform, or rather the discrete fast Fourier transform. Thus, the problem is reduced to determining the convolution of two functions, f and h ,

$$(f * h)(w) = \int_{u_1}^{u_2} du f(u) h(w - u), \quad (\text{A.41})$$

where $h(u)$ has a finite support. Moreover, $h(u)$ is defined as a periodic function with period $u_2 - u_1$, i.e.,

$$h(u) = h(u + N(u_2 - u_1)), \quad \text{where } N \in \mathbb{Z}. \quad (\text{A.42})$$

In the same way, we treat the function $f(u)$ as a periodic function with period $u_2 - u_1$. To quickly determine the convolution (A.41), we introduce the change of variables,

$$u = u_1 + \frac{\phi}{2\pi}(u_2 - u_1), \quad (\text{A.43})$$

$$w = u_1 + \frac{\eta}{2\pi}(u_2 - u_1). \quad (\text{A.44})$$

Introducing the new functions $F(\phi)$ and $H(\phi)$,

$$F(\phi) = f\left(u_1 + \frac{\phi}{2\pi}(u_2 - u_1)\right) \quad (\text{A.45})$$

and

$$H(\phi) = \frac{u_2 - u_1}{2\pi} h\left(\frac{\phi}{2\pi}(u_2 - u_1)\right), \quad (\text{A.46})$$

we will replace the convolution of functions f and h by the convolution of functions F and H ,

$$(f * h)(w) = \int_0^{2\pi} d\phi F(\phi) H(\eta - \phi). \quad (\text{A.47})$$

Since both functions $F(\phi)$ and $H(\phi)$ are periodic functions with period 2π , we represent each of them as a Fourier series,

$$F(\phi) = \sum_N \tilde{F}_N e^{-iN\phi}, \quad \text{where } N \in \mathbb{Z}, \quad (\text{A.48})$$

$$H(\phi) = \sum_M \tilde{H}_M e^{-iM\phi}, \quad \text{where } M \in \mathbb{Z}. \quad (\text{A.49})$$

It leads to the result

$$(f * h)(w) = \sum_{N,M} \tilde{F}_N \tilde{H}_M e^{-iM\eta} \int_0^{2\pi} d\phi e^{-i(N-M)\phi}. \quad (\text{A.50})$$

Since the integral with respect to ϕ equals to $2\pi\delta_{N,M}$ we reduce Eq. (A.50) to

$$(f * h)(w) = 2\pi \sum_N \tilde{F}_N \tilde{H}_N e^{-iN\eta}. \quad (\text{A.51})$$

The remaining sum is determined using the inverse Fourier transform. In practice, this means that we specify a discrete number of ϕ and η variable points,

$$\phi_j = \frac{2\pi}{2^K} j \quad (\text{A.52})$$

$$\eta_j = \frac{2\pi}{2^K} j, \quad j = 0, 1, 2, \dots, 2^K - 1, \quad (\text{A.53})$$

where K is a given natural number, e.g., $K = 10$. At these points we will determine the values of the functions,

$$F_j = F(\phi_j), \quad H_j = H(\phi_j). \quad (\text{A.54})$$

From the values of F_j and H_j , we determine the Fourier coefficients of F and H using the discrete fast Fourier transform, which leads to the convolution function at the points $w_l = u_1 + \frac{\eta_l}{2\pi}(u_2 - u_1)$,

$$(f * h)(w_l) = 2\pi \sum_{j=0}^{2K-1} \tilde{F}_j \tilde{H}_j e^{-ij\eta_l}. \quad (\text{A.55})$$

The last sum is calculated using the discrete inverse fast Fourier transform.

A.2.2 Numerical examples and their analysis

To better understand the meaning and physical contents of spectrograms, we analyze below the amplitude profiles (functions with complex values) with well-known properties. Specifically, we shall examine these properties in two cases:

- when the amplitude is a function of frequency, $F(\omega)$,
- when the amplitude is a function of time, $f(t)$.

Let us begin our discussion with the first case. We define the unit of frequency as ω_0 ; it can be an atomic unit of frequency such that $\hbar\omega_0 = \alpha^2 m_e c^2$ ($\hbar = 1$). Furthermore, we choose the frequency range such that $\omega_{\min} \leq \omega \leq \omega_{\max}$, where $\omega_{\min} = 0$ and $\omega_{\max} = 100\omega_0$. Within this interval, we define three functions with the following analytical expressions,

$$F_1(\omega) = \exp \left[- \left(\frac{\omega - 30\omega_0}{5\omega_0} \right)^2 + i \frac{7}{\omega_0} \omega \right], \quad (\text{A.56})$$

$$F_2(\omega) = 2 \exp \left[- \left(\frac{\omega - 60\omega_0}{4\omega_0} \right)^2 - i \frac{3}{\omega_0} \omega \right], \quad (\text{A.57})$$

$$F_3(\omega) = \frac{\left[\cos \left(\frac{9}{\omega_0} \omega \right) + \sin \left(\frac{5}{\omega_0} \omega \right) \right]}{\cosh^2 \left(\frac{\omega - 50\omega_0}{10\omega_0} \right)}. \quad (\text{A.58})$$

For each of them, we analyze below what we can say about their Fourier transforms,

$$\tilde{F}_j(t) = \int \frac{d\omega}{2\pi} F_j(\omega) e^{-i\omega t}, \quad \text{where } j = 1, 2, 3. \quad (\text{A.59})$$

In the case of $\tilde{F}_1(t)$, it takes significant values for such times t for which the integrand changes slowly as a function of ω . This occurs when $t \approx \frac{7}{\omega_0}$, indicating that the spectrogram of this function takes significant values around the point $(t, \omega) = (\frac{7}{\omega_0}, 30\omega_0)$. A similar reasoning applied to function $F_2(\omega)$ leads to the conclusion that its spectrogram is significantly different from zero in the vicinity of point $(t, \omega) = (-\frac{3}{\omega_0}, 60\omega_0)$. A more complex discussion arises in the

case of function $F_3(\omega)$. From the properties of the $\cosh(x)$ function, it is evident that this function is centered around $\omega = 50\omega_0$. Moreover, its Fourier transform is centered around times, $\pm \frac{9}{\omega_0}$ and $\pm \frac{5}{\omega_0}$. Therefore, in this case, we have four points $(t, \omega) = (\pm \frac{9}{\omega_0}, 50\omega_0), (\pm \frac{5}{\omega_0}, 50\omega_0)$ around which the spectrogram of this function takes significant values.

Now, we consider function $F(\omega)$, which is the sum of the above functions,

$$F(\omega) = F_1(\omega) + F_2(\omega) + F_3(\omega). \quad (\text{A.60})$$

A similar discussion leads us to the conclusion that the spectrogram of this function has maxima at six points on the (t, ω) plane, that have been discussed above. To verify this, we write the spectrogram for the function $F(\omega)$,

$$S(t, \omega) = \left| \int_{\omega_{\min}}^{\omega_{\max}} d\nu F(\nu) W(\omega - \nu, \sigma) e^{-i\nu t} \right|^2, \quad \omega \in [\omega_{\min}, \omega_{\max}], \quad (\text{A.61})$$

where the parameter σ controls the width of the window function $W(\omega - \nu, \sigma)$ around the value $\omega - \nu$. We have the freedom to choose the analytical form of this function, but it must always satisfy two conditions:

- Its spread in frequency should be smaller than $\omega_{\max} - \omega_{\min}$.
- It should be periodic with the period of $\omega_{\max} - \omega_{\min}$, i.e.,

$$W(\omega - \nu + K(\omega_{\max} - \omega_{\min}), \sigma) = W(\omega - \nu, \sigma), \quad K = 0, \pm 1, \pm 2, \dots, \quad (\text{A.62})$$

to enable expansion into a Fourier series.

In addition, in our further analysis, we will choose the window function in the form of a Gaussian function,

$$W(\omega - \nu, \sigma) = \frac{1}{\sqrt{\pi}\sigma} \exp \left[- \left(\frac{\omega - \nu}{\sigma} \right)^2 \right], \quad (\text{A.63})$$

such that

$$\sigma = \zeta_W(\omega_{\max} - \omega_{\min}), \quad 0 < \zeta_W < 1, \quad (\text{A.64})$$

together with the periodicity condition (A.62).

In Fig. A.1, we present function $F(\omega)$ along with its squared magnitude $|F(\omega)|^2$ in a logarithmic scale. Its spectrograms for $\zeta_W = 0.003, 0.01, 0.03, \text{ and } 0.1$ are depicted in the Fig. A.2. To avoid representing insignificant values in time-frequency analysis, a small number 10^{-5} was added to the spectrogram. This eliminates values of $S(t, \omega)$ smaller than this value from the graph. According to the discussion above, the spectrogram exhibits significant values around the specified points. Of course, the form of the spectrogram significantly depends on the choice of the controlling parameter ζ_W . From the definition of the spectrogram, it follows that for small values of ζ_W , the window function is close to a Dirac delta distribution, effectively reproducing the frequency distribution when the time distribution is blurred. Conversely, when ζ_W is large, the window function is spread in frequency, resulting in a spectrogram that accurately approximates the Fourier transform $\tilde{F}(t)$. Therefore, by analyzing the spectrogram for intermediate values of ζ_W , we can gain insight into the time-frequency properties of function $F(\omega)$. In this analysis, the value $\zeta_W=0.03$ seems to be a good choice.

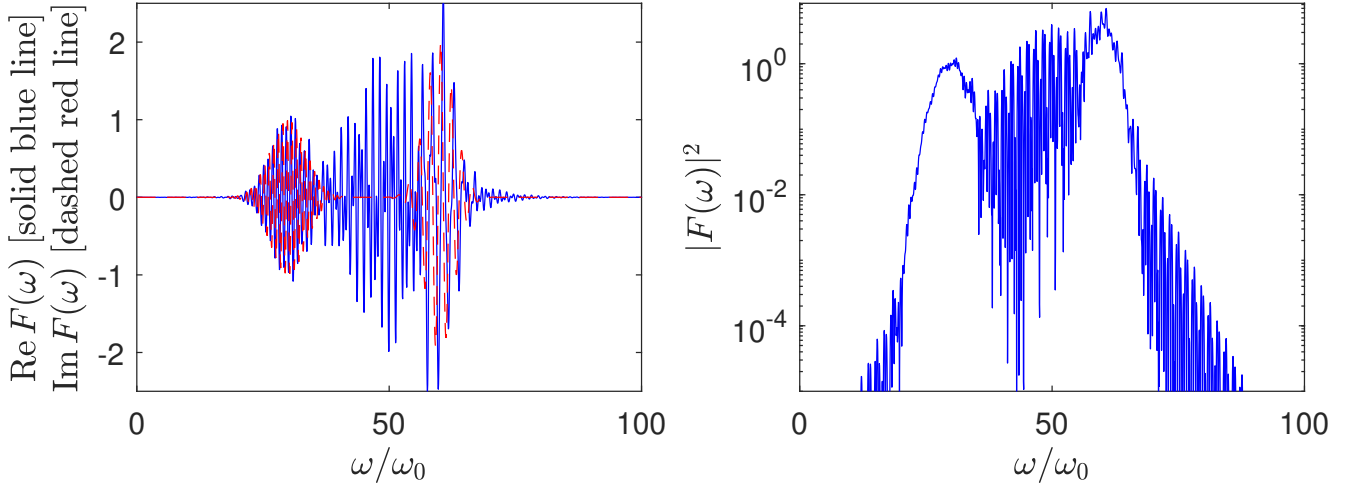


FIGURE A.1: In the left panel, we display the function $F(\omega)$ [Eq. (A.60)] using a linear scale. The blue line corresponds to the real part $\text{Re}[F(\omega)]$, while the dashed red line represents the imaginary part $\text{Im}[F(\omega)]$. In the right panel, we illustrate the squared magnitude of the function, $|F(\omega)|^2$, using a logarithmic scale.

For the sake of completeness, let us illustrate the case of a signal being a function of time, $f(t)$. This case does not necessarily pertain to problems mentioned in this thesis, but it plays a significant role in areas like sonography or seismology. Similar to the frequency case, let us choose unit of time t_0 (which in atomic units would be $t_0 = \frac{1}{\alpha^2 m_e c^2}$) and a time interval $t_{\min} \leq t \leq t_{\max}$, such that $t_{\min} = -30t_0$, $t_{\max} = 60t_0$. As before, we introduce the following analytical functions,

$$f_1(t) = \exp \left[- \left(\frac{t + 5t_0}{5t_0} \right)^2 + i \frac{2}{t_0} t \right], \quad (\text{A.65})$$

$$f_2(t) = \exp \left[- \left(\frac{t - 30t_0}{5t_0} \right)^2 - i \frac{3}{t_0} t \right], \quad (\text{A.66})$$

$$f_3(t) = \frac{\cos \left(\frac{8}{t_0} t \right)}{\cosh^2 \left(\frac{t - 30t_0}{3t_0} \right)}. \quad (\text{A.67})$$

The signal

$$f(t) = f_1(t) + f_2(t) + f_3(t), \quad (\text{A.68})$$

is illustrated in Fig. A.3. Similar analysis to that performed for the frequency case leads us to the conclusion that the spectrogram $\tilde{S}(\omega, t)$, now defined as

$$\tilde{S}(\omega, t) = \left| \int_{t_{\min}}^{t_{\max}} d\tau f(\tau) W(t - \tau, \sigma) e^{i\omega\tau} \right|^2, \quad t \in [t_{\min}, t_{\max}], \quad (\text{A.69})$$

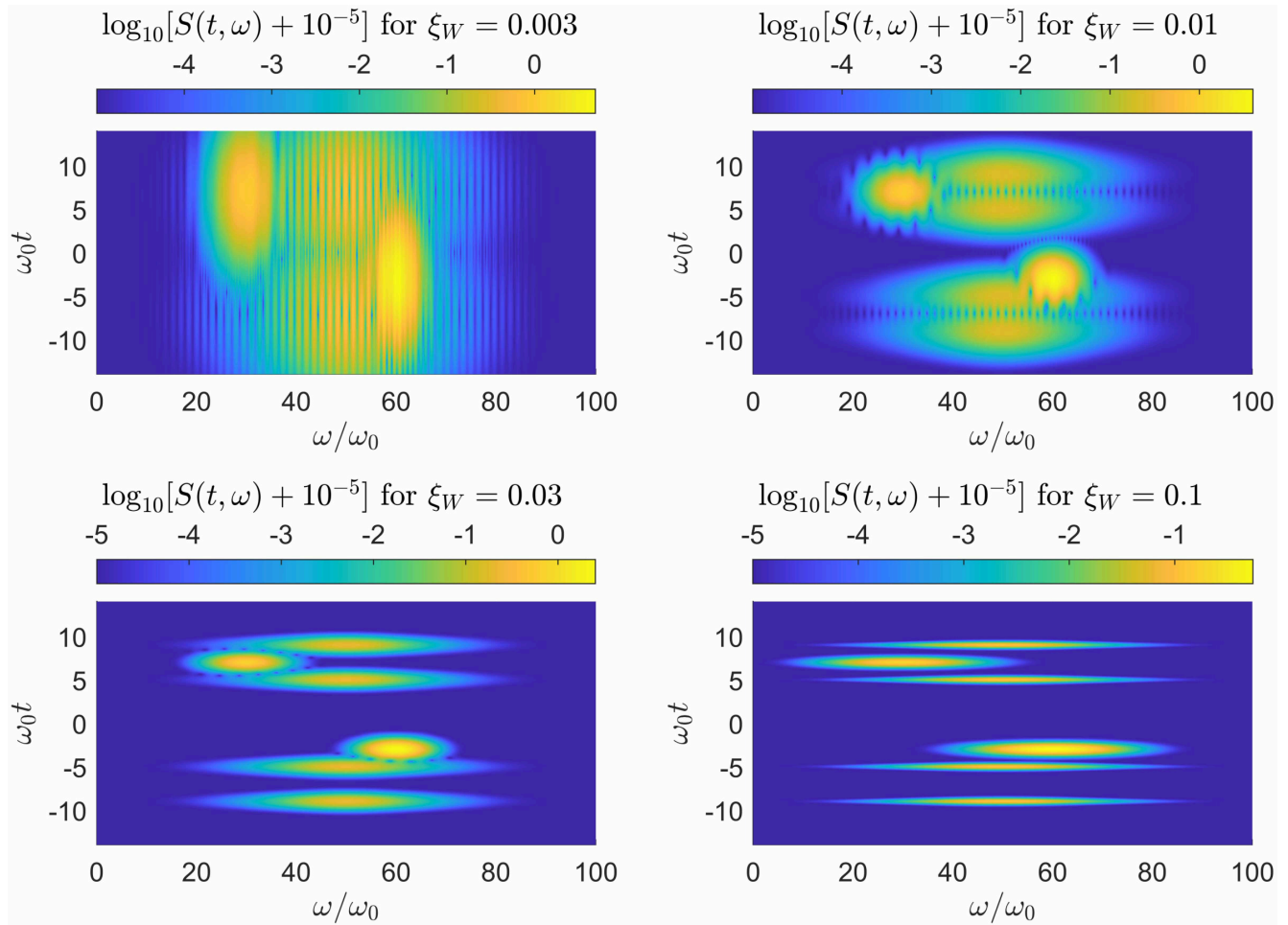


FIGURE A.2: Spectrograms of the function $F(\omega)$ [(A.60)] exhibit distinctive features across all panels, corresponding to parameters $\xi_W = 0.003, 0.01, 0.03,$ and 0.1 . These spectrograms are generated using the Gaussian window $W(\omega - \nu, \sigma)$ as defined in Eq. (A.63). The frequency range extends from $\omega_{\min} = 0$ to $\omega_{\max} = 100\omega_0$, where ω_0 is the unit of frequency. Notably, the width parameter σ (A.64) depends on ξ_W , playing a pivotal role in shaping the distinctive characteristics of the spectrogram.

is centered around points $(\omega, t) = (-\frac{2}{t_0}, -5t_0), (\frac{3}{t_0}, 30t_0),$ and $(\pm\frac{8}{t_0}, 30t_0)$. Similarly, the window function has been chosen as a Gaussian function,

$$W(t - \tau, \sigma) = \frac{1}{\sqrt{\pi}\sigma} \exp \left[- \left(\frac{t - \tau}{\sigma} \right)^2 \right], \quad (\text{A.70})$$

such that

$$\sigma = \xi_W(t_{\max} - t_{\min}), \quad 0 < \xi_W < 1. \quad (\text{A.71})$$

In Fig. A.4, we demonstrate the spectrogram of the function $f(t)$ calculated using the Gaussian window $W(t - \tau, \sigma)$. The left and right panels of Fig. A.4 correspond to two different values of $\xi_W = 0.03$ and 0.1 , showcasing how the window function width influences the characteristics of spectrogram. Overall, this analysis of the time domain complements the earlier discussion of the frequency domain, providing a comprehensive understanding of how the signal evolves both in terms of frequency and time.

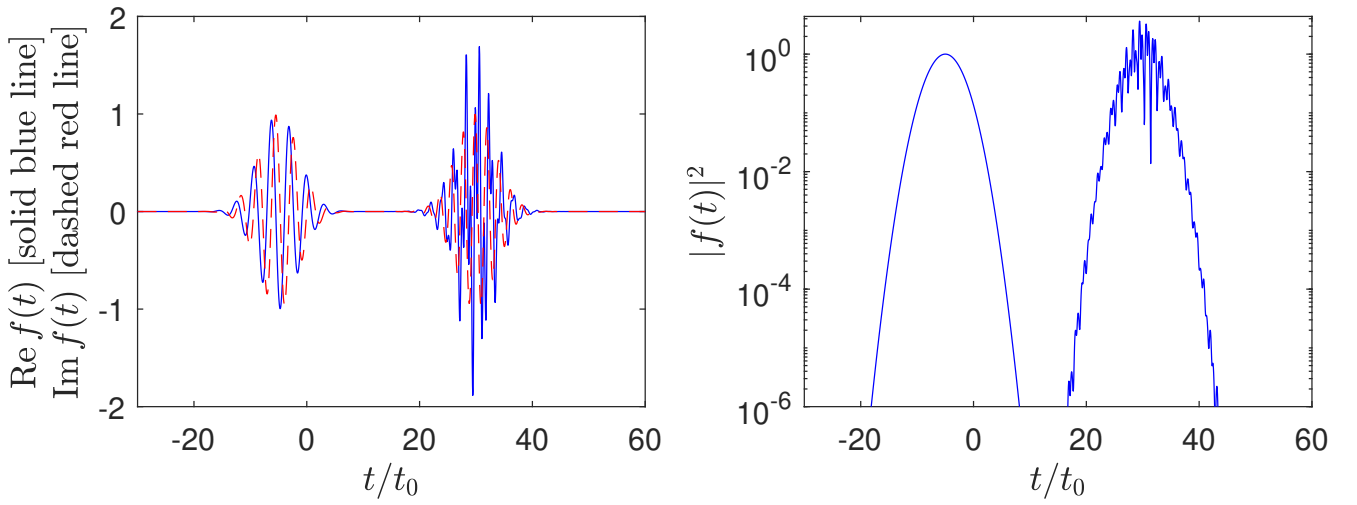


FIGURE A.3: In the left panel, we display the function $f(t)$ (A.68) using a linear scale. The blue line corresponds to the real part $\text{Re}[f(t)]$, while the dashed red line represents the imaginary part $\text{Im}[f(t)]$. In the right panel, we illustrate the squared magnitude of the function, $|f(t)|^2$, using a logarithmic scale.

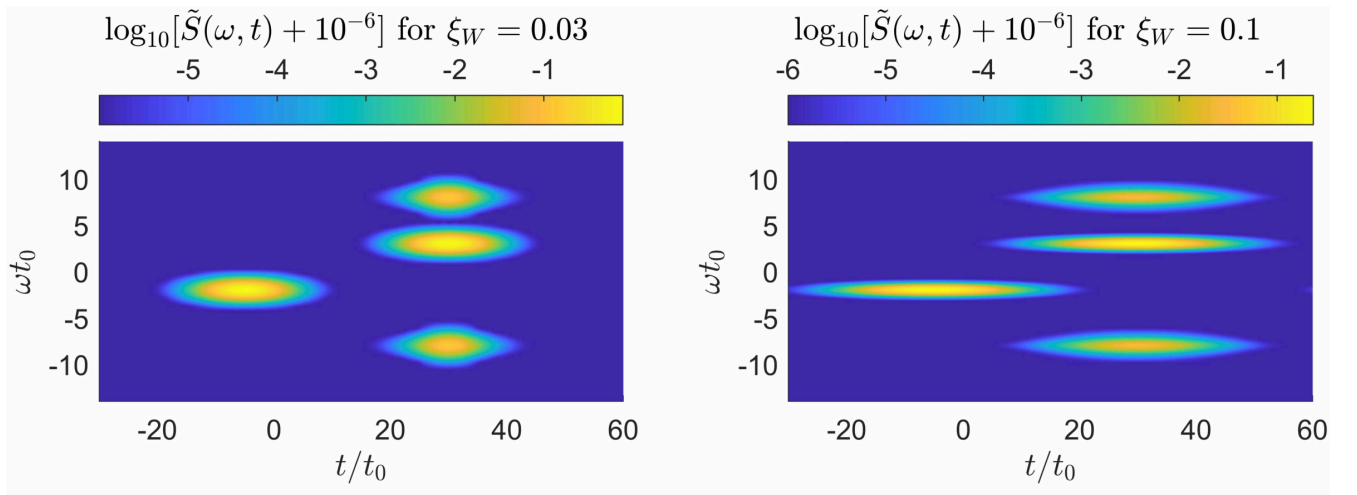


FIGURE A.4: The spectrograms of the function $f(t)$ are computed using the Gaussian window $W(t - \tau, \sigma)$ defined in Eq. (A.70). The left and right panels correspond to the parameters $\xi_W = 0.03$ and $\xi_W = 0.1$, respectively. The temporal range spans from $t_{\min} = 0$ to $t_{\max} = 100t_0$, where t_0 represents the unit of time. The parameter σ controls the width of the window [Eq. (A.71)], influencing the spectrogram's characteristics. To avoid showing small values in time-frequency analysis, a small number 10^{-6} is added to the spectrogram.

Appendix B

Supplementary materials for Chapter 3

B.1 Gauge transformation

Consider the Schrödinger equation that describes the dynamics of the quantum state $|\phi(t)\rangle$ under the action of the Hamiltonian $\hat{\mathcal{H}}(t)$,

$$i\frac{\partial}{\partial t}|\phi(t)\rangle = \hat{\mathcal{H}}(t)|\phi(t)\rangle, \quad (\text{B.1})$$

and a unitary transformation $\hat{U}(t)$ such that

$$|\psi(t)\rangle = \hat{U}(t)|\phi(t)\rangle, \quad \hat{U}^\dagger\hat{U} = \hat{\mathbb{1}}. \quad (\text{B.2})$$

One can show that the transformed state $|\psi(t)\rangle$ satisfies the Schrödinger equation,

$$i\frac{\partial}{\partial t}|\psi(t)\rangle = \hat{H}(t)|\psi(t)\rangle, \quad (\text{B.3})$$

provided that the Hamiltonian is changed to

$$\hat{H}(t) = \left[i\frac{\partial}{\partial t}\hat{U}(t) \right] \hat{U}^\dagger(t) + \hat{U}(t)\hat{\mathcal{H}}(t)\hat{U}^\dagger(t). \quad (\text{B.4})$$

As it was already demonstrated in [131], along with a unitary transformation of the quantum state (B.2) one has to consistently transform the Hamiltonian (B.4).

B.2 Nordsieck integral

In this Appendix, we evaluate the so-called Nordsieck integral defined as [105]

$$I_{\sigma,\eta}(\lambda, \mathbf{q}, \mathbf{p}) = \int d^3r \frac{e^{-\lambda r}}{r} e^{i\mathbf{q}\cdot\mathbf{r}} {}_1F_1(a, 1, i(\sigma p r + \eta \mathbf{p} \cdot \mathbf{r})), \quad (\text{B.5})$$

where $\eta, \sigma = \pm 1, a = iv$ and where we assume that $0 < \text{Re } a < 1$. Here, ${}_1F_1(a, b, x)$ is the confluent hypergeometric function [77], which has the following integral representation,

$${}_1F_1(a, 1, z) = \frac{1}{\Gamma(a)\Gamma(1-a)} \int_0^1 e^{zu} (1-u)^{-a} u^{a-1} du. \quad (\text{B.6})$$

Here, the integral over u is convergent provided that $0 < \text{Re } a < 1$. Evaluating this integral for such a , afterwards we shall continue this integral analytically to account for our case. Substituting Eq. (B.6) into Eq. (B.5) leads to

$$I_{\sigma,\eta}(\lambda, \mathbf{q}, \mathbf{p}) = \frac{1}{\Gamma(a)\Gamma(1-a)} \int_0^1 du (1-u)^{-a} u^{a-1} \mathcal{J}_{\sigma,\eta}(\lambda, \mathbf{q}, \mathbf{p}, u), \quad (\text{B.7})$$

where

$$\mathcal{J}_{\sigma,\eta}(\lambda, \mathbf{q}, \mathbf{p}, u) = \int d^3r \frac{e^{-\lambda r}}{r} e^{i\mathbf{q}\cdot\mathbf{r}} e^{iu(\sigma\mathbf{p}r + \eta\mathbf{p}\cdot\mathbf{r})} = \int d^3r \frac{1}{r} e^{-(\lambda - i\sigma\mathbf{p}u)r} e^{i(\mathbf{q} + \eta\mathbf{p}u)\cdot\mathbf{r}}. \quad (\text{B.8})$$

Evaluating the above integral using spherical coordinates, gives

$$\mathcal{J}_{\sigma,\eta}(\lambda, \mathbf{q}, \mathbf{p}, u) = \frac{4\pi}{\lambda^2 + \mathbf{q}^2} \frac{1}{1 + \xi u'} \quad (\text{B.9})$$

where

$$\xi = -2 \frac{i\sigma\mathbf{p}\lambda - \eta\mathbf{p}\cdot\mathbf{q}}{\lambda^2 + \mathbf{q}^2}. \quad (\text{B.10})$$

Now, putting the value of $\mathcal{J}_{\sigma,\eta}(\lambda, \mathbf{q}, \mathbf{p}, u)$ in Eq. (B.7), we obtain

$$\mathcal{I}_{\sigma,\eta}(\lambda, \mathbf{q}, \mathbf{p}) = \frac{4\pi}{\lambda^2 + \mathbf{q}^2} \mathcal{K}_{\sigma,\eta}(\lambda, \mathbf{q}, \mathbf{p}), \quad (\text{B.11})$$

where

$$\mathcal{K}_{\sigma,\eta}(\lambda, \mathbf{q}, \mathbf{p}) = \frac{1}{\Gamma(a)\Gamma(1-a)} \int_0^1 du (1-u)^{-a} u^{a-1} \frac{1}{1 + \xi u}. \quad (\text{B.12})$$

Using the Euler Beta function [78], the value of above integral is

$$\mathcal{K}_{\sigma,\eta}(\lambda, \mathbf{q}, \mathbf{p}) = (1 + \xi)^{-a}. \quad (\text{B.13})$$

Substituting the value of $\mathcal{K}_{\sigma,\eta}(\lambda, \mathbf{q}, \mathbf{p})$ in Eq. (B.12), we obtain

$$I_{\sigma,\eta}(\lambda, \mathbf{q}, \mathbf{p}) = \frac{4\pi}{\lambda^2 + \mathbf{q}^2} (1 + \xi)^{-a}. \quad (\text{B.14})$$

The phase of $(1 + \xi)^{-a}$ has to be chosen such that for small ξ ,

$$(1 + \xi)^{-a} \approx 1 - a\xi. \quad (\text{B.15})$$

From the practical point of view,

$$(1 + \xi)^{-a} = \exp[-a \ln(1 + \xi)]. \quad (\text{B.16})$$

Also, for small ξ we have $\ln(1 + \xi) \approx \xi$. Hence,

$$\arg[\ln(1 + \xi)] = \arg \xi. \quad (\text{B.17})$$

Since $\text{Im } \zeta < 0$, the phase of ζ has to be such that $-\pi < \arg \zeta < 0$, and the same for $1 + \zeta$: $-\pi < 1 + \arg \zeta < 0$. Consider $\nu = Z\alpha m_e c / |\mathbf{p}| > 0$. In this case,

$$(1 + \zeta)^{-i\nu} = |1 + \zeta| e^{\nu\phi_\zeta} = [(1 + \text{Re } \zeta)^2 + (\text{Im } \zeta)^2]^{-i\nu/2} (1 + \nu\phi_\zeta) = 1 - i\nu(\text{Re } \zeta + i\phi_\zeta) \quad (\text{B.18})$$

and $\nu\phi_\zeta < 0$, where $\phi_\zeta = \arg \zeta$. Moreover, for $|\zeta| \ll 1$, $\phi_\zeta \approx 0$. It allows one to conclude that

$$\text{Im}(1 + \zeta) = |1 + \zeta| \sin \phi_\zeta \approx \phi_\zeta = \text{Im } \zeta. \quad (\text{B.19})$$

Using the value $\phi_\zeta = \text{Im } \zeta$ in Eq. (B.18), we get

$$(1 + \zeta)^{-i\nu} = 1 - i\nu\zeta. \quad (\text{B.20})$$

Moreover,

$$|(1 + \zeta)^{-i\nu}| = |e^{-i\nu \ln |1+\zeta|} e^{\nu\phi_\zeta}| = e^{\nu\phi_\zeta} < 1. \quad (\text{B.21})$$

Using the value of the Nordsieck integral (B.14), we can evaluate expressions which appear in the probability amplitude of LARR in Section 3.2.2. The way that this is done in our numerical code is presented in the next Appendix.

B.3 Details of calculations using the Nordsieck integral

Introducing the following functions,

$$\zeta = \zeta(\lambda, \mathbf{q}) = \frac{1}{\lambda^2 + \mathbf{q}^2}, \quad (\text{B.22})$$

$$\tilde{\zeta} = \tilde{\zeta}(\lambda, \mathbf{q}, \mathbf{p}) = 2\zeta (\sigma_2 \mathbf{p} \cdot \mathbf{q} - i\lambda p \sigma_1), \quad (\text{B.23})$$

$$f = f(\lambda, \mathbf{q}, \mathbf{p}) = \zeta(1 + \tilde{\zeta})^{-i\nu}, \quad (\text{B.24})$$

we can express the value of the Nordsieck integral (B.14) such that

$$I_{\sigma_1 \sigma_2}(\lambda, \mathbf{q}, \mathbf{p}) = 4\pi\zeta(1 + \tilde{\zeta})^{-i\nu} = 4\pi f. \quad (\text{B.25})$$

In our calculations in Section 3.2.2, we use derivatives of $I_{\sigma_1 \sigma_2}(\lambda, \mathbf{q}, \mathbf{p})$. For this reason, we define

$$\zeta_\lambda = \frac{\partial \zeta}{\partial \lambda} = -\frac{2\lambda}{(\lambda^2 + \mathbf{q}^2)^2} = -2\lambda\zeta^2, \quad (\text{B.26})$$

$$\zeta_{\mathbf{v}} = (\mathbf{v} \cdot \nabla_{\mathbf{q}})\zeta = -\frac{2(\mathbf{v} \cdot \mathbf{q})}{(\lambda^2 + \mathbf{q}^2)^2} = -2\zeta^2(\mathbf{v} \cdot \mathbf{q}), \quad (\text{B.27})$$

$$\zeta_{\mathbf{u}} = (\mathbf{u} \cdot \nabla_{\mathbf{q}})\zeta = -\frac{2(\mathbf{u} \cdot \mathbf{q})}{(\lambda^2 + \mathbf{q}^2)^2} = -2\zeta^2(\mathbf{u} \cdot \mathbf{q}), \quad (\text{B.28})$$

$$\zeta_{\mathbf{w}} = (\mathbf{w} \cdot \nabla_{\mathbf{q}})\zeta = -\frac{2(\mathbf{w} \cdot \mathbf{q})}{(\lambda^2 + \mathbf{q}^2)^2} = -2\zeta^2(\mathbf{w} \cdot \mathbf{q}), \quad (\text{B.29})$$

$$\zeta_{\lambda,u} = \frac{\partial}{\partial \lambda} (\mathbf{u} \cdot \nabla_{\mathbf{q}}) \zeta = \frac{8\lambda(\mathbf{u} \cdot \mathbf{q})}{(\lambda^2 + \mathbf{q}^2)^3} = 8\zeta^3 \lambda(\mathbf{u} \cdot \mathbf{q}), \quad (\text{B.30})$$

$$\zeta_{\lambda,v} = \frac{\partial}{\partial \lambda} (\mathbf{v} \cdot \nabla_{\mathbf{q}}) \zeta = \frac{8\lambda(\mathbf{v} \cdot \mathbf{q})}{(\lambda^2 + \mathbf{q}^2)^3} = 8\zeta^3 \lambda(\mathbf{v} \cdot \mathbf{q}), \quad (\text{B.31})$$

$$\zeta_{\lambda,w} = \frac{\partial}{\partial \lambda} (\mathbf{w} \cdot \nabla_{\mathbf{q}}) \zeta = \frac{8\lambda(\mathbf{w} \cdot \mathbf{q})}{(\lambda^2 + \mathbf{q}^2)^3} = 8\zeta^3 \lambda(\mathbf{w} \cdot \mathbf{q}), \quad (\text{B.32})$$

$$\begin{aligned} \zeta_{u,v} &= (\mathbf{u} \cdot \nabla_{\mathbf{q}})(\mathbf{v} \cdot \nabla_{\mathbf{q}}) \zeta = -\mathbf{u} \cdot \left\{ \frac{2\mathbf{v} \cdot \mathbf{1}}{(\lambda^2 + \mathbf{q}^2)^2} - \frac{8\mathbf{q}(\mathbf{v} \cdot \mathbf{q})}{(\lambda^2 + \mathbf{q}^2)^3} \right\} \\ &= -2\zeta^2(\mathbf{v} \cdot \mathbf{u}) - 4\zeta\zeta_v(\mathbf{u} \cdot \mathbf{q}), \end{aligned} \quad (\text{B.33})$$

$$\begin{aligned} \zeta_{w,v} &= (\mathbf{w} \cdot \nabla_{\mathbf{q}})(\mathbf{v} \cdot \nabla_{\mathbf{q}}) \zeta = -\mathbf{w} \cdot \left\{ \frac{2\mathbf{v} \cdot \mathbf{1}}{(\lambda^2 + \mathbf{q}^2)^2} - \frac{8\mathbf{q}(\mathbf{v} \cdot \mathbf{q})}{(\lambda^2 + \mathbf{q}^2)^3} \right\} \\ &= -2\zeta^2(\mathbf{v} \cdot \mathbf{w}) - 4\zeta\zeta_v(\mathbf{w} \cdot \mathbf{q}), \end{aligned} \quad (\text{B.34})$$

$$\begin{aligned} \zeta_{u,w} &= (\mathbf{u} \cdot \nabla_{\mathbf{q}})(\mathbf{w} \cdot \nabla_{\mathbf{q}}) \zeta = -\mathbf{u} \cdot \left\{ \frac{2\mathbf{w} \cdot \mathbf{1}}{(\lambda^2 + \mathbf{q}^2)^2} - \frac{8\mathbf{q}(\mathbf{w} \cdot \mathbf{q})}{(\lambda^2 + \mathbf{q}^2)^3} \right\} \\ &= -2\zeta^2(\mathbf{w} \cdot \mathbf{u}) - 4\zeta\zeta_w(\mathbf{u} \cdot \mathbf{q}), \end{aligned} \quad (\text{B.35})$$

$$\begin{aligned} \zeta_{w,u,v} &= (\mathbf{w} \cdot \nabla_{\mathbf{q}})(\mathbf{u} \cdot \nabla_{\mathbf{q}})(\mathbf{v} \cdot \nabla_{\mathbf{q}}) \zeta \\ &= -4\zeta\zeta_w(\mathbf{v} \cdot \mathbf{u}) - 4\zeta_v\zeta_w(\mathbf{u} \cdot \mathbf{q}) - 4\zeta\zeta_{w,v}(\mathbf{u} \cdot \mathbf{q}) - 4\zeta\zeta_v(\mathbf{u} \cdot \mathbf{w}), \end{aligned} \quad (\text{B.36})$$

$$\begin{aligned} \zeta_{\lambda,u,v} &= \frac{\partial}{\partial \lambda} (\mathbf{u} \cdot \nabla_{\mathbf{q}})(\mathbf{v} \cdot \nabla_{\mathbf{q}}) \zeta = \left(\frac{8\lambda(\mathbf{v} \cdot \mathbf{u})}{(\lambda^2 + \mathbf{q}^2)^3} - \frac{48\lambda(\mathbf{u} \cdot \mathbf{q})(\mathbf{v} \cdot \mathbf{q})}{(\lambda^2 + \mathbf{q}^2)^4} \right) \\ &= -4\zeta\zeta_\lambda(\mathbf{v} \cdot \mathbf{u}) - 4(\zeta_\lambda\zeta_u + \zeta\zeta_{\lambda,u})(\mathbf{v} \cdot \mathbf{q}), \end{aligned} \quad (\text{B.37})$$

$$\begin{aligned} \zeta_{\lambda,w,v} &= \frac{\partial}{\partial \lambda} (\mathbf{w} \cdot \nabla_{\mathbf{q}})(\mathbf{v} \cdot \nabla_{\mathbf{q}}) \zeta = \left(\frac{8\lambda(\mathbf{v} \cdot \mathbf{w})}{(\lambda^2 + \mathbf{q}^2)^3} - \frac{48\lambda(\mathbf{w} \cdot \mathbf{q})(\mathbf{v} \cdot \mathbf{q})}{(\lambda^2 + \mathbf{q}^2)^4} \right) \\ &= -4\zeta\zeta_\lambda(\mathbf{v} \cdot \mathbf{w}) - 4(\zeta_\lambda\zeta_w + \zeta\zeta_{\lambda,w})(\mathbf{v} \cdot \mathbf{q}), \end{aligned} \quad (\text{B.38})$$

$$\begin{aligned} \zeta_{\lambda,u,v,w} &= -4\zeta_w\zeta_\lambda(\mathbf{v} \cdot \mathbf{u}) - 4\zeta\zeta_{\lambda,w}(\mathbf{v} \cdot \mathbf{u}) - 4\zeta_{\lambda,v}\zeta_w(\mathbf{u} \cdot \mathbf{q}) - 4\zeta_v\zeta_{\lambda,w}(\mathbf{u} \cdot \mathbf{q}) \\ &\quad - 4\zeta_\lambda\zeta_{w,v}(\mathbf{u} \cdot \mathbf{q}) - 4\zeta\zeta_{\lambda,w,v}(\mathbf{u} \cdot \mathbf{q}) - 4\zeta_\lambda\zeta_v(\mathbf{u} \cdot \mathbf{w}) - 4\zeta\zeta_{\lambda,v}(\mathbf{u} \cdot \mathbf{w}). \end{aligned} \quad (\text{B.39})$$

Note that $\zeta_{u,v} = \zeta_{v,u}$ and $\zeta_{\lambda,u,v} = \zeta_{\lambda,v,u}$. Similarly, $\zeta_{u,v,w} = \zeta_{v,u,w} = \zeta_{u,w,v} = \zeta_{w,v,u}$ and $\zeta_{\lambda,u,v,w} = \zeta_{\lambda,v,u,w}$ and so on. Moreover,

$$\begin{aligned} \zeta_\lambda &= \frac{\partial \zeta}{\partial \lambda} = -\frac{4\lambda(\sigma_2 \mathbf{p} \cdot \mathbf{q} - i\lambda p \sigma_1)}{(\lambda^2 + \mathbf{q}^2)^2} - \frac{2ip\sigma_1}{\lambda^2 + \mathbf{q}^2} \\ &= 2\zeta_\lambda(\sigma_2 \mathbf{p} \cdot \mathbf{q} - i\lambda p \sigma_1) - 2ip\sigma_1\zeta, \end{aligned} \quad (\text{B.40})$$

$$\begin{aligned} \zeta_v &= (\mathbf{v} \cdot \nabla_{\mathbf{q}}) \zeta = \left\{ \frac{2\sigma_2(\mathbf{p} \cdot \mathbf{v})}{\lambda^2 + \mathbf{q}^2} - \frac{4(\mathbf{v} \cdot \mathbf{q})(\sigma_2 \mathbf{p} \cdot \mathbf{q} - i\lambda p \sigma_1)}{(\lambda^2 + \mathbf{q}^2)^2} \right\} \\ &= 2\sigma_2(\mathbf{p} \cdot \mathbf{v})\zeta + 2\zeta_v(\sigma_2 \mathbf{p} \cdot \mathbf{q} - i\lambda p \sigma_1), \end{aligned} \quad (\text{B.41})$$

$$\begin{aligned} \zeta_u &= (\mathbf{u} \cdot \nabla_{\mathbf{q}}) \zeta = \left\{ \frac{2\sigma_2(\mathbf{p} \cdot \mathbf{u})}{\lambda^2 + \mathbf{q}^2} - \frac{4(\mathbf{u} \cdot \mathbf{q})(\sigma_2 \mathbf{p} \cdot \mathbf{q} - i\lambda p \sigma_1)}{(\lambda^2 + \mathbf{q}^2)^2} \right\} \\ &= 2\sigma_2(\mathbf{p} \cdot \mathbf{u})\zeta + 2\zeta_u(\sigma_2 \mathbf{p} \cdot \mathbf{q} - i\lambda p \sigma_1), \end{aligned} \quad (\text{B.42})$$

$$\begin{aligned}\xi_w &= (\mathbf{w} \cdot \nabla_q) \xi = \left\{ \frac{2\sigma_2(\mathbf{p} \cdot \mathbf{w})}{\lambda^2 + q^2} - \frac{4(\mathbf{w} \cdot \mathbf{q})(\sigma_2 \mathbf{p} \cdot \mathbf{q} - i\lambda p \sigma_1)}{(\lambda^2 + q^2)^2} \right\} \\ &= 2\sigma_2(\mathbf{p} \cdot \mathbf{w})\zeta + 2\zeta_w(\sigma_2 \mathbf{p} \cdot \mathbf{q} - i\lambda p \sigma_1),\end{aligned}\quad (\text{B.43})$$

$$\begin{aligned}\xi_{\lambda,u} &= \frac{\partial}{\partial \lambda} (\mathbf{u} \cdot \nabla_q) \xi = \left\{ \frac{16\lambda(\mathbf{u} \cdot \mathbf{q})(\sigma_2 \mathbf{p} \cdot \mathbf{q} - i\lambda p \sigma_1)}{(\lambda^2 + q^2)^3} + \frac{4ip\sigma_1(\mathbf{v} \cdot \mathbf{q})}{(\lambda^2 + q^2)^2} - \frac{4\lambda\sigma_2(\mathbf{p} \cdot \mathbf{u})}{(\lambda^2 + q^2)^2} \right\} \\ &= 2\zeta_{\lambda,v}(\sigma_2 \mathbf{p} \cdot \mathbf{q} - i\lambda p \sigma_1) + 2\zeta_\lambda\sigma_2(\mathbf{p} \cdot \mathbf{u}) - 2ip\sigma_1\zeta_u,\end{aligned}\quad (\text{B.44})$$

$$\begin{aligned}\xi_{\lambda,v} &= \frac{\partial}{\partial \lambda} (\mathbf{v} \cdot \nabla_q) \xi = \left\{ \frac{16\lambda(\mathbf{v} \cdot \mathbf{q})(\sigma_2 \mathbf{p} \cdot \mathbf{q} - i\lambda p \sigma_1)}{(\lambda^2 + q^2)^3} + \frac{4ip\sigma_1(\mathbf{v} \cdot \mathbf{q})}{(\lambda^2 + q^2)^2} - \frac{4\lambda\sigma_2(\mathbf{p} \cdot \mathbf{v})}{(\lambda^2 + q^2)^2} \right\} \\ &= 2\zeta_{\lambda,v}(\sigma_2 \mathbf{p} \cdot \mathbf{q} - i\lambda p \sigma_1) + 2\zeta_\lambda\sigma_2(\mathbf{p} \cdot \mathbf{v}) - 2ip\sigma_1\zeta_v,\end{aligned}\quad (\text{B.45})$$

$$\begin{aligned}\xi_{\lambda,w} &= \frac{\partial}{\partial \lambda} (\mathbf{w} \cdot \nabla_q) \xi = \left\{ \frac{16\lambda(\mathbf{w} \cdot \mathbf{q})(\sigma_2 \mathbf{p} \cdot \mathbf{q} - i\lambda p \sigma_1)}{(\lambda^2 + q^2)^3} + \frac{4ip\sigma_1(\mathbf{w} \cdot \mathbf{q})}{(\lambda^2 + q^2)^2} - \frac{4\lambda\sigma_2(\mathbf{p} \cdot \mathbf{w})}{(\lambda^2 + q^2)^2} \right\} \\ &= 2\zeta_{\lambda,w}(\sigma_2 \mathbf{p} \cdot \mathbf{q} - i\lambda p \sigma_1) + 2\zeta_\lambda\sigma_2(\mathbf{p} \cdot \mathbf{w}) - 2ip\sigma_1\zeta_w,\end{aligned}\quad (\text{B.46})$$

$$\begin{aligned}\xi_{u,v} &= (\mathbf{u} \cdot \nabla_q)(\mathbf{v} \cdot \nabla_q) \xi = \frac{16(\mathbf{u} \cdot \mathbf{q})(\mathbf{v} \cdot \mathbf{q})(\sigma_2 \mathbf{p} \cdot \mathbf{q} - i\lambda p \sigma_1)}{(\lambda^2 + q^2)^3} \\ &\quad - \frac{4(\mathbf{u} \cdot \mathbf{v})(\sigma_2 \mathbf{p} \cdot \mathbf{q} - i\lambda p \sigma_1)}{(\lambda^2 + q^2)^2} - \frac{4\sigma_2(\mathbf{p} \cdot \mathbf{v})(\mathbf{u} \cdot \mathbf{q})}{(\lambda^2 + q^2)^2} - \frac{4\sigma_2(\mathbf{p} \cdot \mathbf{u})(\mathbf{v} \cdot \mathbf{q})}{(\lambda^2 + q^2)^2} \\ &= 2\zeta_{u,v}(\sigma_2 \mathbf{p} \cdot \mathbf{q} - i\lambda p \sigma_1) + 2\sigma_2(\mathbf{p} \cdot \mathbf{v})\zeta_u + 2\sigma_2(\mathbf{p} \cdot \mathbf{u})\zeta_v,\end{aligned}\quad (\text{B.47})$$

$$\xi_{u,w} = 2\zeta_{u,w}(\sigma_2 \mathbf{p} \cdot \mathbf{q} - i\lambda p \sigma_1) + 2\sigma_2(\mathbf{p} \cdot \mathbf{w})\zeta_u + 2\sigma_2(\mathbf{p} \cdot \mathbf{u})\zeta_w, \quad (\text{B.48})$$

$$\xi_{w,v} = 2\zeta_{w,v}(\sigma_2 \mathbf{p} \cdot \mathbf{q} - i\lambda p \sigma_1) + 2\sigma_2(\mathbf{p} \cdot \mathbf{v})\zeta_w + 2\sigma_2(\mathbf{p} \cdot \mathbf{w})\zeta_v, \quad (\text{B.49})$$

$$\xi_{u,v,w} = 2\zeta_{u,v,w}(\sigma_2 \mathbf{p} \cdot \mathbf{q} - i\lambda p \sigma_1) + 2\zeta_{u,v}\sigma_2(\mathbf{p} \cdot \mathbf{w}) + 2\sigma_2(\mathbf{p} \cdot \mathbf{v})\zeta_{w,u} + 2\sigma_2(\mathbf{p} \cdot \mathbf{u})\zeta_{v,w}, \quad (\text{B.50})$$

$$\begin{aligned}\xi_{\lambda,u,v} &= \frac{\partial}{\partial \lambda} (\mathbf{u} \cdot \nabla_q)(\mathbf{v} \cdot \nabla_q) \xi \\ &= \frac{16\lambda(\mathbf{u} \cdot \mathbf{v})(\sigma_2 \mathbf{p} \cdot \mathbf{q} - i\lambda p \sigma_1)}{(\lambda^2 + q^2)^3} - \frac{96\lambda(\mathbf{u} \cdot \mathbf{q})(\mathbf{v} \cdot \mathbf{q})(\sigma_2 \mathbf{p} \cdot \mathbf{q} - i\lambda p \sigma_1)}{(\lambda^2 + q^2)^4} \\ &\quad + \frac{4ip\sigma_1(\mathbf{u} \cdot \mathbf{v})}{(\lambda^2 + q^2)^2} - \frac{16ip\sigma_1(\mathbf{u} \cdot \mathbf{q})(\mathbf{v} \cdot \mathbf{q})}{(\lambda^2 + q^2)^3} + \frac{16\lambda\sigma_2(\mathbf{p} \cdot \mathbf{v})(\mathbf{u} \cdot \mathbf{q})}{(\lambda^2 + q^2)^3} + \frac{16\lambda\sigma_2(\mathbf{p} \cdot \mathbf{u})(\mathbf{v} \cdot \mathbf{q})}{(\lambda^2 + q^2)^3} \\ &= 2\zeta_{\lambda,u,v}(\sigma_2 \mathbf{p} \cdot \mathbf{q} - i\lambda p \sigma_1) - 2ip\sigma_1\zeta_{u,v} + 2\sigma_2(\mathbf{p} \cdot \mathbf{v})\zeta_{\lambda,u} + 2\sigma_2(\mathbf{p} \cdot \mathbf{u})\zeta_{\lambda,v},\end{aligned}\quad (\text{B.51})$$

$$\xi_{\lambda,u,w} = 2\zeta_{\lambda,u,w}(\sigma_2 \mathbf{p} \cdot \mathbf{q} - i\lambda p \sigma_1) - 2ip\sigma_1\zeta_{u,w} + 2\sigma_2(\mathbf{p} \cdot \mathbf{w})\zeta_{\lambda,u} + 2\sigma_2(\mathbf{p} \cdot \mathbf{u})\zeta_{\lambda,w}, \quad (\text{B.52})$$

$$\xi_{\lambda,v,w} = 2\zeta_{\lambda,v,w}(\sigma_2 \mathbf{p} \cdot \mathbf{q} - i\lambda p \sigma_1) - 2ip\sigma_1\zeta_{v,w} + 2\sigma_2(\mathbf{p} \cdot \mathbf{w})\zeta_{\lambda,v} + 2\sigma_2(\mathbf{p} \cdot \mathbf{v})\zeta_{\lambda,w}, \quad (\text{B.53})$$

$$\begin{aligned}\xi_{\lambda,u,v,w} &= 2\zeta_{\lambda,u,v,w}(\sigma_2 \mathbf{p} \cdot \mathbf{q} - i\lambda p \sigma_1) - 2ip\sigma_1\zeta_{u,v,w} + 2\sigma_2(\mathbf{p} \cdot \mathbf{w})\zeta_{\lambda,u,v} + 2\sigma_2(\mathbf{p} \cdot \mathbf{v})\zeta_{\lambda,w,u} \\ &\quad + 2\sigma_2(\mathbf{p} \cdot \mathbf{u})\zeta_{\lambda,v,w}.\end{aligned}\quad (\text{B.54})$$

Hence, we have the derivatives:

$$f_\lambda = \frac{\partial f}{\partial \lambda} = (1 + \xi)^{-iv} \left(\frac{-iv\zeta\xi_\lambda}{1 + \xi} + \zeta_\lambda \right) = f_\lambda^{(1)} \cdot f, \quad (\text{B.55})$$

$$\begin{aligned}
f_v &= (\mathbf{v} \cdot \nabla_{\mathbf{q}})f = -\frac{2(1+\xi)^{-iv}(\mathbf{v} \cdot \mathbf{q})}{(\lambda^2 + \mathbf{q}^2)^2} - \frac{iv(1+\xi)^{-1-iv}\xi_v}{\lambda^2 + \mathbf{q}^2} \\
&= \zeta(1+\xi)^{-iv} \left(\frac{\xi_v}{\zeta} - \frac{iv\xi_v}{1+\xi} \right) = f_v^{(1)} \cdot f,
\end{aligned} \tag{B.56}$$

$$f_u = (\mathbf{u} \cdot \nabla_{\mathbf{q}})f = f_u^{(1)} \cdot f, \tag{B.57}$$

$$\begin{aligned}
f_{\lambda,v} &= \frac{\partial}{\partial \lambda} (\mathbf{v} \cdot \nabla_{\mathbf{q}})f \\
&= -i\zeta\nu(1+\xi)^{-1-iv}\xi_{\lambda,u} + 2i\zeta^2\lambda\nu\xi_{\lambda}(1+\xi)^{-1-iv} + 8\zeta^3\lambda(1+\xi)^{-iv}(\mathbf{v} \cdot \mathbf{q}) + \\
&\quad 2i\zeta^2\nu\xi_{\lambda}(1+\xi)^{-1-iv}(\mathbf{v} \cdot \mathbf{q}) - i\zeta(-1-iv)\nu\xi_{\lambda}(1+\xi)^{-2-iv}\xi_v \\
&= (1+\xi)^{-iv} \left(\frac{\xi_{\lambda,v}}{\zeta} - \frac{iv\xi_{\lambda,v}}{1+\xi} - \frac{iv\xi_{\lambda}\xi_{\lambda}}{\zeta(1+\xi)} - \frac{iv\xi_{\lambda}\xi_v}{\zeta(1+\xi)} - \frac{\nu^2\xi_{\lambda}\xi_v}{(1+\xi)^2} + \frac{iv\xi_{\lambda}\xi_v}{(1+\xi)^2} \right) \\
&= f_{\lambda,v}^{(2)} \cdot f,
\end{aligned} \tag{B.58}$$

$$f_{\lambda,u} = \frac{\partial}{\partial \lambda} (\mathbf{u} \cdot \nabla_{\mathbf{q}})f = f_{\lambda,u}^{(2)} \cdot f, \tag{B.59}$$

$$\begin{aligned}
f_{u,v} &= (\mathbf{u} \cdot \nabla_{\mathbf{q}})(\mathbf{v} \cdot \nabla_{\mathbf{q}})f \\
&\quad - i\zeta\nu(1+\xi)^{-1-iv}\xi_{u,v} + 8\zeta^3(1+\xi)^{-iv}(\mathbf{u} \cdot \mathbf{q})(\mathbf{v} \cdot \mathbf{q}) + 2i\zeta^2\nu(1+\xi)^{-1-iv}(\mathbf{v} \cdot \mathbf{q})\xi_u \\
&\quad + 2i\zeta^2\nu(\mathbf{v} \cdot \mathbf{q})(1+\xi)^{-1-iv}\xi_v - 2\zeta^2(1+\xi)^{-iv}\mathbf{v} \cdot \mathbf{u} - i\zeta(-1-iv)\nu(1+\xi)^{-2-iv}\xi_u\xi_v \\
&= \zeta(1+\xi)^{-iv} \left(\frac{\xi_{u,v}}{\zeta} - \frac{iv\xi_{u,v}}{1+\xi} - \frac{iv\xi_u\xi_v}{\zeta(1+\xi)} - \frac{iv\xi_u\xi_v}{\zeta(1+\xi)} - \frac{\nu^2\xi_u\xi_v}{(1+\xi)^2} + \frac{iv\xi_u\xi_v}{(1+\xi)^2} \right) \\
&= f_{u,v}^{(2)} \cdot f,
\end{aligned} \tag{B.60}$$

$$\begin{aligned}
f_{\lambda,u,v} &= \frac{\partial}{\partial \lambda} (\mathbf{u} \cdot \nabla_{\mathbf{q}})(\mathbf{v} \cdot \nabla_{\mathbf{q}})f \\
&= \left(-\frac{iv\xi_u\xi_{\lambda,v}}{\zeta(1+\xi)} - \frac{iv\xi_v\xi_{\lambda,u}}{\zeta(1+\xi)} - \frac{iv\xi_{\lambda}\xi_{u,v}}{\zeta(1+\xi)} - \frac{iv\xi_v\xi_{\lambda,u}}{\zeta(1+\xi)} - \frac{i\lambda\nu\xi_u\xi_{\lambda,v}}{\zeta(1+\xi)} - \frac{iv\xi_{\lambda}\xi_{u,v}}{\zeta(1+\xi)} + \frac{\xi_{\lambda,u,v}}{\zeta} \right. \\
&\quad - \frac{i(-1-iv)\nu\xi_u\xi_{\lambda,v}}{(1+\xi)^2} - \frac{i(-1-iv)\nu\xi_{\lambda}\xi_{u,v}}{(1+\xi)^2} - \frac{i(-1-iv)\nu\xi_v\xi_{\lambda,u}}{(1+\xi)^2} - \frac{iv\xi_{\lambda,u,v}}{1+\xi} \\
&\quad - \frac{i(-1-iv)\nu\xi_{\lambda}\xi_u\xi_v}{\zeta(1+\xi)^2} - \frac{i(-1-iv)\nu\xi_{\lambda}\xi_u\xi_v}{\zeta(1+\xi)^2} - \frac{i(-1-iv)\nu\xi_{\lambda}\xi_u\xi_v}{\zeta(1+\xi)^2} \\
&\quad \left. - \frac{i(-2-iv)(-1-iv)\nu\xi_{\lambda}\xi_u\xi_v}{(1+\xi)^3} \right) \cdot f,
\end{aligned} \tag{B.61}$$

$$f_{\lambda,u,v} = f_{\lambda,u,v}^{(3)} \cdot f, \tag{B.62}$$

$$f_{u,v,w} = (\mathbf{w} \cdot \nabla_{\mathbf{q}})(\mathbf{u} \cdot \nabla_{\mathbf{q}})(\mathbf{v} \cdot \nabla_{\mathbf{q}})f = (f_{u,v,w}^{(2)} + f_{u,v}^{(2)} \cdot f_w^{(1)}) \cdot f = f_{u,v,w}^{(3)} \cdot f, \tag{B.63}$$

$$f_{\lambda,u,v,w} = \frac{\partial}{\partial \lambda} f_{u,v,w} = f_{\lambda,u,v,w}^{(4)} \cdot f. \tag{B.64}$$

Note that $f_{u,v} = f_{v,u}$ and $f_{\lambda,u,v} = f_{\lambda,v,u}$. Moreover,

$$f_{\lambda}^{(1)} = \left(\frac{\xi_{\lambda}}{\zeta} - \frac{iv\xi_{\lambda}}{1+\xi} \right), \tag{B.65}$$

$$f_u^{(1)} = \left(\frac{\zeta_u}{\zeta} - \frac{i\nu\tilde{\zeta}_u}{1+\tilde{\zeta}} \right), \quad (\text{B.66})$$

$$f_v^{(1)} = \left(\frac{\zeta_v}{\zeta} - \frac{i\nu\tilde{\zeta}_v}{1+\tilde{\zeta}} \right), \quad (\text{B.67})$$

$$f_w^{(1)} = \left(\frac{\zeta_w}{\zeta} - \frac{i\nu\tilde{\zeta}_w}{1+\tilde{\zeta}} \right), \quad (\text{B.68})$$

$$f_{u,v}^{(1)} = \left(\frac{\zeta_{u,v}}{\zeta} - \frac{\zeta_u\zeta_v}{\zeta^2} - \frac{i\nu\tilde{\zeta}_{u,v}}{1+\tilde{\zeta}} + \frac{i\nu\tilde{\zeta}_u\tilde{\zeta}_v}{(1+\tilde{\zeta})^2} \right), \quad (\text{B.69})$$

$$f_{v,w}^{(1)} = \mathbf{w} \cdot \nabla_q f_v^{(1)} = \left(\frac{\zeta_{v,w}}{\zeta} - \frac{\zeta_v\zeta_w}{\zeta^2} - \frac{i\nu\tilde{\zeta}_{v,w}}{1+\tilde{\zeta}} + \frac{i\nu\tilde{\zeta}_v\tilde{\zeta}_w}{(1+\tilde{\zeta})^2} \right), \quad (\text{B.70})$$

$$f_{u,w}^{(1)} = \mathbf{w} \cdot \nabla_q f_u^{(1)} = \left(\frac{\zeta_{u,w}}{\zeta} - \frac{\zeta_u\zeta_w}{\zeta^2} - \frac{i\nu\tilde{\zeta}_{u,w}}{1+\tilde{\zeta}} + \frac{i\nu\tilde{\zeta}_u\tilde{\zeta}_w}{(1+\tilde{\zeta})^2} \right), \quad (\text{B.71})$$

$$\begin{aligned} f_{\lambda,v,u}^{(2)} &= \frac{\zeta_{\lambda,u,v}}{\zeta} - \frac{\zeta_{v,u}\zeta_\lambda}{\zeta^2} - \frac{\zeta_{\lambda,v}\zeta_u}{\zeta^2} - \frac{\zeta_{\lambda,u}\zeta_v}{\zeta^2} + \frac{2\zeta_v\zeta_u\zeta_\lambda}{\zeta^3} - i\nu\frac{\tilde{\zeta}_{\lambda,u,v}}{1+\tilde{\zeta}} + i\nu\frac{\tilde{\zeta}_{v,u}\tilde{\zeta}_\lambda}{(1+\tilde{\zeta})^2} \\ &\quad + i\nu\frac{\tilde{\zeta}_{\lambda,u}\tilde{\zeta}_v}{(1+\tilde{\zeta})^2} + i\nu\frac{\tilde{\zeta}_{\lambda,v}\tilde{\zeta}_u}{(1+\tilde{\zeta})^2} - 2i\nu\frac{\tilde{\zeta}_v\tilde{\zeta}_u\tilde{\zeta}_\lambda}{(1+\tilde{\zeta})^3}, \end{aligned} \quad (\text{B.72})$$

$$\begin{aligned} f_{\lambda,u,w}^{(2)} &= \frac{\zeta_{\lambda,u,w}}{\zeta} - \frac{\zeta_{\lambda}\zeta_{u,w}}{\zeta^2} - \frac{\zeta_{\lambda,u}\zeta_w}{\zeta^2} - \frac{\zeta_u\zeta_{\lambda,w}}{\zeta^2} + 2\frac{\zeta_\lambda\zeta_u\zeta_w}{\zeta^3} - \frac{i\nu\tilde{\zeta}_{\lambda,u,w}}{1+\tilde{\zeta}} + \frac{i\nu\tilde{\zeta}_\lambda\tilde{\zeta}_{u,w}}{(1+\tilde{\zeta})^2} \\ &\quad + \frac{i\nu\tilde{\zeta}_{\lambda,u}\tilde{\zeta}_w}{(1+\tilde{\zeta})^2} + \frac{i\nu\tilde{\zeta}_u\tilde{\zeta}_{\lambda,w}}{(1+\tilde{\zeta})^2} - 2\frac{i\nu\tilde{\zeta}_\lambda\tilde{\zeta}_u\tilde{\zeta}_w}{(1+\tilde{\zeta})^3}, \end{aligned} \quad (\text{B.73})$$

$$\begin{aligned} f_{\lambda,v,w}^{(2)} &= \frac{\zeta_{\lambda,v,w}}{\zeta} - \frac{\zeta_{\lambda}\zeta_{v,w}}{\zeta^2} - \frac{\zeta_{\lambda,v}\zeta_w}{\zeta^2} - \frac{\zeta_v\zeta_{\lambda,w}}{\zeta^2} + 2\frac{\zeta_\lambda\zeta_v\zeta_w}{\zeta^3} - \frac{i\nu\tilde{\zeta}_{\lambda,v,w}}{1+\tilde{\zeta}} + \frac{i\nu\tilde{\zeta}_\lambda\tilde{\zeta}_{v,w}}{(1+\tilde{\zeta})^2} \\ &\quad + \frac{i\nu\tilde{\zeta}_{\lambda,v}\tilde{\zeta}_w}{(1+\tilde{\zeta})^2} + \frac{i\nu\tilde{\zeta}_v\tilde{\zeta}_{\lambda,w}}{(1+\tilde{\zeta})^2} - 2\frac{i\nu\tilde{\zeta}_\lambda\tilde{\zeta}_v\tilde{\zeta}_w}{(1+\tilde{\zeta})^3}, \end{aligned} \quad (\text{B.74})$$

$$f_{\lambda,v}^{(1)} = \frac{\partial}{\partial\lambda} f_v^{(1)} = \frac{\zeta_{\lambda,v}}{\zeta} - \frac{\zeta_\lambda\zeta_v}{\zeta^2} - \frac{i\nu\tilde{\zeta}_{\lambda,v}}{1+\tilde{\zeta}} + \frac{i\nu\tilde{\zeta}_\lambda\tilde{\zeta}_v}{(1+\tilde{\zeta})^2}, \quad (\text{B.75})$$

$$f_{\lambda,u}^{(1)} = \frac{\partial}{\partial\lambda} f_u^{(1)} = \frac{\zeta_{\lambda,u}}{\zeta} - \frac{\zeta_\lambda\zeta_u}{\zeta^2} - \frac{i\nu\tilde{\zeta}_{\lambda,u}}{1+\tilde{\zeta}} + \frac{i\nu\tilde{\zeta}_\lambda\tilde{\zeta}_u}{(1+\tilde{\zeta})^2}, \quad (\text{B.76})$$

$$f_{\lambda,w}^{(1)} = \frac{\partial}{\partial\lambda} f_w^{(1)} = \frac{\zeta_{\lambda,w}}{\zeta} - \frac{\zeta_\lambda\zeta_w}{\zeta^2} - \frac{i\nu\tilde{\zeta}_{\lambda,w}}{1+\tilde{\zeta}} + \frac{i\nu\tilde{\zeta}_\lambda\tilde{\zeta}_w}{(1+\tilde{\zeta})^2}, \quad (\text{B.77})$$

$$f_{\lambda,v}^{(2)} = f_{\lambda,v}^{(1)} + f_\lambda^{(1)} \cdot f_v^{(1)}, \quad (\text{B.78})$$

$$f_{\lambda,u}^{(2)} = f_{\lambda,u}^{(1)} + f_\lambda^{(1)} \cdot f_u^{(1)}, \quad (\text{B.79})$$

$$f_{\lambda,w}^{(2)} = f_{\lambda,w}^{(1)} + f_\lambda^{(1)} \cdot f_w^{(1)}, \quad (\text{B.80})$$

$$\begin{aligned} f_{u,v,w}^{(1)} &= \frac{\zeta_{u,v,w}}{\zeta} - \frac{\zeta_{u,v}\zeta_w}{\zeta^2} - \frac{\zeta_{u,w}\zeta_v}{\zeta^2} - \frac{\zeta_u\zeta_{v,w}}{\zeta^2} + \frac{2\zeta_u\zeta_v\zeta_w}{\zeta^3} - \frac{i\nu\tilde{\zeta}_{u,v,w}}{1+\tilde{\zeta}} + \frac{i\nu\tilde{\zeta}_u\tilde{\zeta}_{v,w}}{(1+\tilde{\zeta})^2} \\ &\quad + \frac{i\nu\tilde{\zeta}_{u,v}\tilde{\zeta}_w}{(1+\tilde{\zeta})^2} + \frac{i\nu\tilde{\zeta}_u\tilde{\zeta}_{v,w}}{(1+\tilde{\zeta})^2} - 2\frac{i\nu\tilde{\zeta}_u\tilde{\zeta}_v\tilde{\zeta}_w}{(1+\tilde{\zeta})^3}. \end{aligned} \quad (\text{B.81})$$

$$\begin{aligned}
f_{\lambda,u,v,w}^{(1)} &= \frac{\zeta_{\lambda,u,v,w}}{\zeta} - \frac{\zeta_{u,v,w}\zeta_{\lambda}}{\zeta^2} - \frac{\zeta_{\lambda,u,v}\zeta_w}{\zeta^2} - \frac{\zeta_{u,v}\zeta_{\lambda,w}}{\zeta^2} + 2\frac{\zeta_{u,v}\zeta_w\zeta_{\lambda}}{\zeta^3} \\
&- \frac{\zeta_{\lambda,u,w}\zeta_v}{\zeta^2} - \frac{\zeta_{u,w}\zeta_{\lambda v}}{\zeta^2} + 2\frac{\zeta_{u,w}\zeta_v\zeta_{\lambda}}{\zeta^3} - \frac{\zeta_{\lambda,u}\zeta_{v,w}}{\zeta^2} - \frac{\zeta_u\zeta_{\lambda,v,w}}{\zeta^2} + 2\frac{\zeta_u\zeta_{v,w}\zeta_{\lambda}}{\zeta^3} \\
&+ \frac{2\zeta_{\lambda,u}\zeta_v\zeta_w}{\zeta^3} + \frac{2\zeta_u\zeta_{\lambda,v}\zeta_w}{\zeta^3} + \frac{2\zeta_u\zeta_v\zeta_{\lambda,w}}{\zeta^3} - \frac{6\zeta_u\zeta_v\zeta_w\zeta_{\lambda}}{\zeta^4} - \frac{i\nu\zeta_{\lambda,u,v,w}}{1+\zeta} \\
&+ \frac{i\nu\zeta_{\lambda}\zeta_{u,v,w}}{(1+\zeta)^2} + \frac{i\nu\zeta_{\lambda,u,v}\zeta_w}{(1+\zeta)^2} + \frac{i\nu\zeta_{u,v}\zeta_{\lambda,w}}{(1+\zeta)^2} - 2\frac{i\nu\zeta_{u,v}\zeta_w\zeta_{\lambda}}{(1+\zeta)^3} + \frac{i\nu\zeta_{\lambda,u,w}\zeta_v}{(1+\zeta)^2} \\
&+ \frac{i\nu\zeta_{u,w}\zeta_{\lambda,v}}{(1+\zeta)^2} - 2\frac{i\nu\zeta_{\lambda}\zeta_{u,w}\zeta_v}{(1+\zeta)^3} + \frac{i\nu\zeta_{\lambda,u}\zeta_{v,w}}{(1+\zeta)^2} + \frac{i\nu\zeta_u\zeta_{\lambda,v,w}}{(1+\zeta)^2} - 2\frac{i\nu\zeta_{\lambda}\zeta_u\zeta_{v,w}}{(1+\zeta)^3} \\
&- 2\frac{i\nu\zeta_{\lambda,u}\zeta_v\zeta_w}{(1+\zeta)^3} - 2\frac{i\nu\zeta_u\zeta_{\lambda,v}\zeta_w}{(1+\zeta)^3} - 2\frac{i\nu\zeta_u\zeta_v\zeta_{\lambda,w}}{(1+\zeta)^3} + 6\frac{i\nu\zeta_{\lambda}\zeta_u\zeta_v\zeta_w}{(1+\zeta)^4}, \tag{B.82}
\end{aligned}$$

$$f_{v,u}^{(2)} = f_{v,u}^{(1)} + f_v^{(1)} \cdot f_u^{(1)}, \tag{B.83}$$

$$f_{\lambda,v,u}^{(2)} = f_{\lambda,v,u}^{(1)} + f_{\lambda,u}^{(1)} \cdot f_v^{(1)} + f_{\lambda,v}^{(1)} \cdot f_u^{(1)}, \tag{B.84}$$

$$f_{\lambda,v,w}^{(2)} = f_{\lambda,v,w}^{(1)} + f_{\lambda,w}^{(1)} \cdot f_v^{(1)} + f_{\lambda,v}^{(1)} \cdot f_w^{(1)}, \tag{B.85}$$

$$f_{\lambda,u,w}^{(2)} = f_{\lambda,u,w}^{(1)} + f_{\lambda,w}^{(1)} \cdot f_u^{(1)} + f_{\lambda,u}^{(1)} \cdot f_w^{(1)}, \tag{B.86}$$

$$f_{u,v,w}^{(2)} = f_{u,v,w}^{(1)} + f_{v,w}^{(1)} \cdot f_u^{(1)} + f_v^{(1)} \cdot f_{u,w}^{(1)}, \tag{B.87}$$

$$f_{u,v}^{(3)} = f_{u,v}^{(2)} + f_{u,v}^{(2)} \cdot f_w^{(1)}, \tag{B.88}$$

$$f_{\lambda,v,u}^{(3)} = f_{\lambda,v,u}^{(2)} + f_{u,v}^{(2)} \cdot f_{\lambda}^{(1)}, \tag{B.89}$$

$$f_{\lambda,u,v,w}^{(2)} = f_{\lambda,u,v,w}^{(1)} + f_{\lambda,v,w}^{(1)} \cdot f_u^{(1)} + f_{v,w}^{(1)} \cdot f_{\lambda,u}^{(1)} + f_{\lambda,v}^{(1)} \cdot f_{u,w}^{(1)} + f_v^{(1)} \cdot f_{\lambda,u,w}^{(1)}, \tag{B.90}$$

$$f_{\lambda,u,v,w}^{(3)} = f_{\lambda,u,v,w}^{(2)} + f_{\lambda,u,v}^{(2)} \cdot f_w^{(1)} + f_{u,v}^{(2)} \cdot f_{\lambda,w}^{(1)} \tag{B.91}$$

$$\begin{aligned}
&= f_{\lambda,u,v,w}^{(1)} + f_{\lambda,u,w}^{(3)} \cdot f_v^{(1)} + f_{\lambda,v,w}^{(3)} \cdot f_u^{(1)} - 2f_{u,w}^{(2)} \cdot f_{\lambda}^{(1)} \cdot f_v^{(1)} - 2f_{v,w}^{(2)} \cdot f_{\lambda}^{(1)} \cdot f_u^{(1)} \\
&- 2f_{\lambda,w}^{(2)} \cdot f_v^{(1)} \cdot f_u^{(1)} - 2f_{\lambda,u}^{(2)} \cdot f_v^{(1)} \cdot f_w^{(1)} - 2f_{\lambda,w}^{(2)} \cdot f_v^{(1)} \cdot f_u^{(1)} - 2f_{\lambda,v}^{(2)} \cdot f_u^{(1)} \cdot f_w^{(1)} \\
&+ 6f_{\lambda}^{(1)} \cdot f_w^{(1)} \cdot f_u^{(1)} \cdot f_v^{(1)} + f_{u,w}^{(2)} \cdot f_{\lambda,v}^{(2)} + f_{v,w}^{(2)} \cdot f_{\lambda,u}^{(2)} + f_{\lambda,u,v}^{(2)} \cdot f_w^{(1)} \\
&+ f_{u,v}^{(2)} \cdot f_{\lambda,w}^{(2)} - 2f_{v,u}^{(2)} \cdot f_{\lambda}^{(1)} \cdot f_w^{(1)}, \tag{B.92}
\end{aligned}$$

$$f_{\lambda,u,v,w}^{(4)} = f_{\lambda,u,v,w}^{(3)} + f_{u,v,w}^{(3)} \cdot f_{\lambda}^{(1)}. \tag{B.93}$$

Finally,

$$\frac{\partial}{\partial \lambda} I_{\sigma_1, \sigma_2}(v, \lambda, \mathbf{q}, \mathbf{p}) = 4\pi f_{\lambda}, \tag{B.94}$$

$$(\mathbf{v} \cdot \nabla_{\mathbf{q}}) I_{\sigma_1, \sigma_2}(v, \lambda, \mathbf{q}, \mathbf{p}) = 4\pi f_v, \tag{B.95}$$

$$(\mathbf{u} \cdot \nabla_{\mathbf{q}}) I_{\sigma_1, \sigma_2}(v, \lambda, \mathbf{q}, \mathbf{p}) = 4\pi f_u, \tag{B.96}$$

$$\frac{\partial}{\partial \lambda} (\mathbf{u} \cdot \nabla_{\mathbf{q}}) I_{\sigma_1, \sigma_2}(v, \lambda, \mathbf{q}, \mathbf{p}) = 4\pi f_{\lambda,u}, \tag{B.97}$$

$$\frac{\partial}{\partial \lambda} (\mathbf{v} \cdot \nabla_{\mathbf{q}}) I_{\sigma_1, \sigma_2}(v, \lambda, \mathbf{q}, \mathbf{p}) = 4\pi f_{\lambda,v}, \tag{B.98}$$

$$(\mathbf{u} \cdot \nabla_q)(\mathbf{v} \cdot \nabla_q) I_{\sigma_1, \sigma_2}(\nu, \lambda, \mathbf{q}, \mathbf{p}) = 4\pi f_{u,v}, \quad (\text{B.99})$$

$$\frac{\partial}{\partial \lambda} (\mathbf{u} \cdot \nabla_q)(\mathbf{v} \cdot \nabla_q) I_{\sigma_1, \sigma_2}(\nu, \lambda, \mathbf{q}, \mathbf{p}) = 4\pi f_{\lambda, u, v}, \quad (\text{B.100})$$

$$\frac{\partial}{\partial \lambda} (\mathbf{w} \cdot \nabla_q)(\mathbf{u} \cdot \nabla_q)(\mathbf{v} \cdot \nabla_q) I_{\sigma_1, \sigma_2}(\nu, \lambda, \mathbf{q}, \mathbf{p}) = 4\pi f_{\lambda, u, v, w}, \quad (\text{B.101})$$

which allows us to calculate the probability amplitude of LARR, as specified in Section 3.2.2.

B.4 Classical consideration

Consider an electron of momentum \mathbf{p} moving in a laser field, that propagates in the direction \mathbf{n} . The Newton-Lorentz equation describing the electron dynamics takes the form,

$$\dot{\boldsymbol{\pi}}_{\text{cl}} = e\boldsymbol{\mathcal{E}}(\mathbf{r}, t) + \frac{e}{m_e} \boldsymbol{\pi}_{\text{cl}} \times \boldsymbol{\mathcal{B}}(\mathbf{r}, t), \quad (\text{B.102})$$

where $\boldsymbol{\pi}_{\text{cl}}$ is the electron kinetic momentum. Here, $\boldsymbol{\mathcal{E}}(\mathbf{r}, t) = \boldsymbol{\mathcal{E}}(t - \frac{\mathbf{n} \cdot \mathbf{r}}{c})$ and $\boldsymbol{\mathcal{B}}(\mathbf{r}, t) = \boldsymbol{\mathcal{B}}(t - \frac{\mathbf{n} \cdot \mathbf{r}}{c})$ are the electric and magnetic components of the laser field such that $\mathbf{n} \cdot \boldsymbol{\mathcal{E}}(\mathbf{r}, t) = 0$ and $\mathbf{n} \cdot \boldsymbol{\mathcal{B}}(\mathbf{r}, t) = 0$. Using Maxwell relation $\boldsymbol{\mathcal{B}}(\mathbf{r}, t) = \frac{1}{c} \mathbf{n} \times \boldsymbol{\mathcal{E}}(\mathbf{r}, t)$ and applying the vector triple product formula in the second term of Eq. (B.102), we get

$$\dot{\boldsymbol{\pi}}_{\text{cl}} = e\boldsymbol{\mathcal{E}}(\mathbf{r}, t) + \frac{e}{m_e c} \mathbf{n} [\boldsymbol{\pi}_{\text{cl}} \cdot \boldsymbol{\mathcal{E}}(\mathbf{r}, t)] - \frac{e}{m_e c} \boldsymbol{\mathcal{E}}(\mathbf{r}, t) (\mathbf{n} \cdot \boldsymbol{\pi}_{\text{cl}}). \quad (\text{B.103})$$

Expanding Eq. (B.103) in the leading order in $1/c$, we arrive at

$$\dot{\boldsymbol{\pi}}_{\text{cl}} = e\boldsymbol{\mathcal{E}}(t) - \frac{\mathbf{n} \cdot \mathbf{r}}{c} e\dot{\boldsymbol{\mathcal{E}}}(t) + \frac{e}{m_e c} \mathbf{n} (\boldsymbol{\pi}_{\text{cl}} \cdot \boldsymbol{\mathcal{E}}(t)) - \frac{e}{m_e c} \boldsymbol{\mathcal{E}}(t) (\mathbf{n} \cdot \boldsymbol{\pi}_{\text{cl}}), \quad (\text{B.104})$$

where $\boldsymbol{\mathcal{E}}(t)$ is already the spatially homogeneous electric field. Henceforth, we look for the solution of Eq. (B.104) in the form

$$\boldsymbol{\pi}_{\text{cl}} = \mathbf{p} - e\mathbf{A}(t) + \delta\boldsymbol{\pi}(t). \quad (\text{B.105})$$

where $\mathbf{A}(t)$ is the vector potential corresponding to the laser field such that $\boldsymbol{\mathcal{E}}(t) = -\dot{\mathbf{A}}(t)$, and $\delta\boldsymbol{\pi}(t)$ consists of the terms of the order of $1/c$. Substituting Eq. (B.105) in Eq. (B.104), we arrive at

$$\delta\dot{\boldsymbol{\pi}}(t) = -\frac{\mathbf{n} \cdot \mathbf{r}}{c} e\dot{\boldsymbol{\mathcal{E}}}(t) + \frac{e}{m_e c} \mathbf{n} \cdot [(\mathbf{p} - e\mathbf{A}(t)) \cdot \boldsymbol{\mathcal{E}}(t)] - \frac{e}{m_e c} \boldsymbol{\mathcal{E}}(t) [\mathbf{n} \cdot (\mathbf{p} - e\mathbf{A}(t))]. \quad (\text{B.106})$$

Using the fact that the field is transverse such that $\mathbf{n} \cdot \mathbf{A}(t) = 0$ and integrating Eq. (B.106) with respect to time, we arrive at the solution,

$$\delta\boldsymbol{\pi}(t) = -\frac{\mathbf{n} \cdot \mathbf{r}}{c} e\boldsymbol{\mathcal{E}}(t) - \frac{e}{m_e c} \mathbf{n} \cdot [\mathbf{p} \cdot \mathbf{A}(t)] + \mathbf{n} \frac{e^2 \mathbf{A}^2(t)}{2m_e c}. \quad (\text{B.107})$$

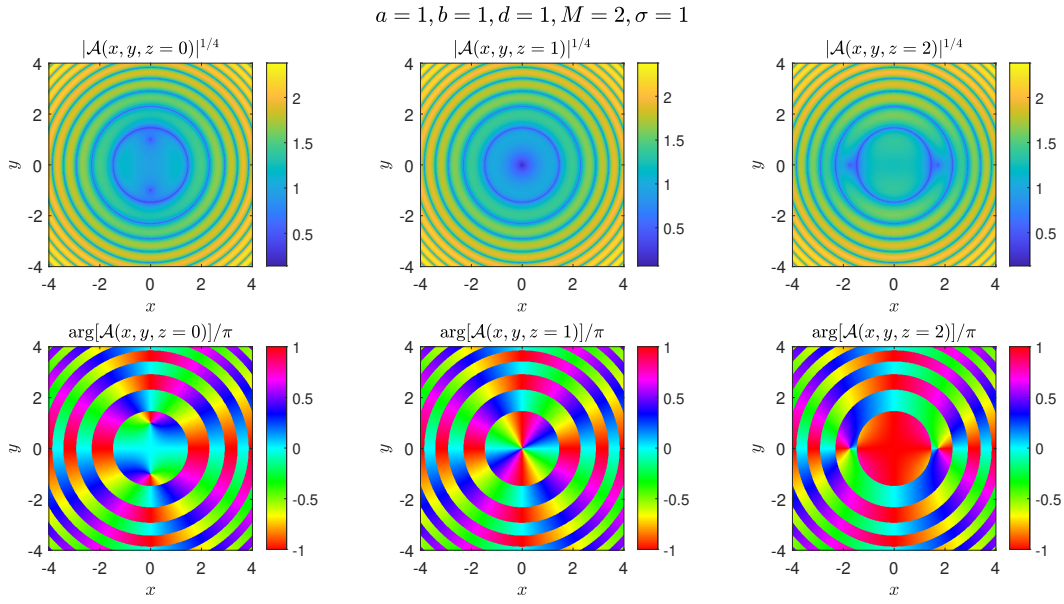


FIGURE B.1: The top row demonstrates the magnitude of the function $\mathcal{A}(\mathbf{r})$ [Eq. (B.109)] in the xy -plane at $z = 0$, $z = 1$, and $z = 2$. In the bottom row, we plot the corresponding phase of $\mathcal{A}(\mathbf{r})$. We use parameters $a = 1$, $b = 1$, $d = 1$, $M = 2$, and $\sigma = 1$. The magnitude of the function is displayed to the power $1/4$ to better visualise the vortices and nodal surfaces.

Now, we use Eqs. (B.105) and (B.107) to derive the expression for the kinetic energy of an electron in the presence of a laser field. In the leading order in $1/c$, we obtain

$$\begin{aligned} \frac{\pi_{\text{cl}}^2}{2m_e} &= \frac{[\mathbf{p} - e\mathbf{A}(t)]^2}{2m_e} - \frac{\mathbf{n} \cdot \mathbf{p}}{m_e^2 c} \left[e\mathbf{A}(t) \cdot \mathbf{p} - \frac{1}{2} e^2 \mathbf{A}^2(t) \right] \\ &+ \frac{\mathbf{n} \cdot \mathbf{r}}{m_e c} [(\mathbf{p} - e\mathbf{A}(t)) \cdot e\boldsymbol{\mathcal{E}}(t)] + \mathcal{O}\left(\frac{1}{c^2}\right). \end{aligned} \quad (\text{B.108})$$

Here, the second term corresponds to the electron recoil, whereas the third term originates from the retardation. This agrees with our results and their interpretation provided in Chapter 3.

B.5 Mathematical model of vortices

To understand the formation of vortex structures and nodal surfaces or lines, we analyse a complex function $\mathcal{A}(\mathbf{r})$ in a three-dimensional space of a parameter $\mathbf{r} = (x, y, z)$,

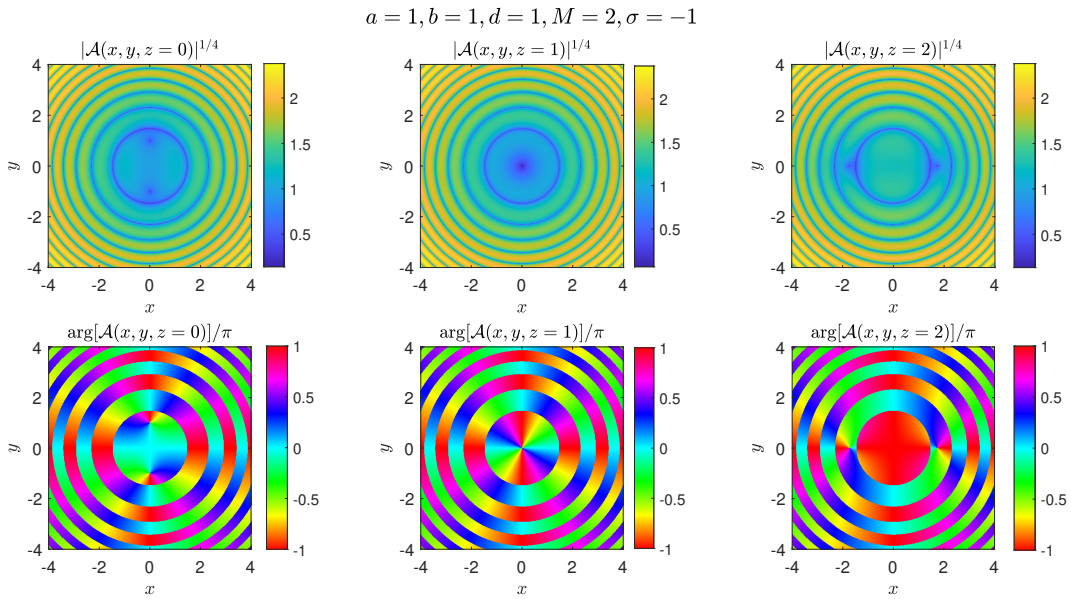
$$\mathcal{A}(\mathbf{r}) = \mathcal{A}(x, y, z) = [(x + i\sigma y)^M + a^2 - z^2] \sin(b(x^2 + y^2 + d^2)), \quad (\text{B.109})$$

where we assume that $M \in \mathbb{N}$, $\sigma \in \mathbb{Z}$, and $a, b, d \in \mathbb{R}$. For this function we have zeroes at

$$\sin(b(x^2 + y^2 + d^2)) = 0 \quad (\text{B.110})$$

and

$$(x + i\sigma y)^M + a^2 - z^2 = 0. \quad (\text{B.111})$$

FIGURE B.2: Same as in Fig. B.1 except for $\sigma = -1$.

The solution of Eq. (B.110) can be derived analytically since

$$b(x^2 + y^2 + d^2) = n\pi, \quad n \in \mathbb{Z}. \quad (\text{B.112})$$

Hence, we will observe zero surfaces in the form of cylinders along the z -axis, with a radius $\sqrt{\frac{n\pi - bd^2}{b}}$, provided that $n\pi \geq bd^2$. The solutions of Eq. (B.111) form lines in the space of $\mathbf{r} = (x, y, z)$. For Eq. (B.111), for different values of z , we will have a different set of zeroes of $\mathcal{A}(\mathbf{r})$ based on parameters a, b, d, M, σ . It follows from this analysis that we should observe regions of zero values of $\mathcal{A}(\mathbf{r})$ forming concentric circles and points in the xy -plane.

For instance, when $a = 1$ and $M = 2$, we have

$$(x + i\sigma y)^2 + 1 - z^2 = 0. \quad (\text{B.113})$$

We demonstrate the magnitude and the phase of the function $\mathcal{A}(\mathbf{r})$ for $\sigma = 1$ (Fig. B.1) and $\sigma = -1$ (Fig. B.2). These cases are shown in xy -planes for $d = 1$ at $z = 0, z = 1$, and $z = 2$. We observe in each case concentric rings with zero values (upper rows) but with the phase of $\mathcal{A}(\mathbf{r})$ jumping across those rings by π (lower rows). This is typical for nodal lines (surfaces). In the case of vortices, the value of the function $\mathcal{A}(\mathbf{r})$ is zero at those points as well, however the amplitude $\arg[\mathcal{A}(\mathbf{r})]$ is singular there. Moreover, it changes continuously around the vortex by multiples of 2π . The multiplication index is called a topological charge (or, a winding number), m . This is very well illustrated, for instance, in Fig. B.1 for $z = 1$. The function $\mathcal{A}(\mathbf{r})$ has clearly a zero at the point $(x, y) = (0, 0)$ but its phase is changing anticlockwise by 4π during one complete turn around that point. This means that $\mathcal{A}(\mathbf{r})$ has a vortex at the point $(0, 0)$ with a topological charge $m = +2$. In contrast, for $\sigma = -1$ (Fig. B.2) the function $\mathcal{A}(\mathbf{r})$ has a vortex at $(0, 0)$ with a topological charge $m = -2$. Even more rich vortex structures are shown in both figures for $z = 0$ and $z = 2$. Each of the corresponding columns shows two vortices with the topological charge $m = +1$ (Fig. B.1) or $m = -1$ (Fig. B.2).

Bibliography

- [1] C. J. Joachain, N. J. Kylstra, and R. M. Potvliege *Atoms in Intense Laser Fields* (Cambridge University Press, New York, 2011, 1st ed.).
- [2] C. D. Lin, A.-T. Le, C. Jin, and H. Wei, *Attosecond and Strong-Field Physics: Principles and Applications* (Cambridge University Press, Cambridge, 2018, 1st ed.).
- [3] <https://www.nobelprize.org/uploads/2023/10/advanced-physicsprize2023-2.pdf>
- [4] M. Lewenstein, Ph. Balcou, M. Yu. Ivanov, A. L’Huillier and P. B. Corkum. Theory of high-harmonic generation by low-frequency laser fields. *Phys. Rev A* **49**, 2117 (1994).
- [5] J. M. Schins, P. Breger, P. Agostini, R. C. Constantinescu, H. G. Muller, G. Grillon, A. Antonetti and A. Mysyrowicz. Observation of Laser-Assisted Auger Decay in Argon. *Phys. Rev. Lett.* **73**, 2180 (1994).
- [6] P. Antoine, A. L’Huillier and M. Lewenstein. Attosecond Pulse Trains Using High-Order Harmonics. *Phys. Rev. Lett.* **77**, 1234 (1996).
- [7] P. Salières, A. L’Huillier, P. Antoine and M. Lewenstein. Study of the spatial and temporal coherence of high order harmonics. *arXiv quantph/9710060* (1997).
- [8] M. Nisoli, S. De Silvestri, O. Svelto, R. Szipöcs, K. Ferencz, Ch. Spielmann, S. Sartania and F. Krausz. Compression of high-energy laser pulses below 5 fs. *Opt. Lett.* **22**, 522 (1997).
- [9] Ch. Spielmann, N. H. Burnett, S. Sartania, R. Koppitsch, M. Schnürer, C. Kan, M. Lenzner, P. Wobrauschek and F. Krausz. Generation of Coherent X-rays in the Water Window Using 5-Femtosecond Laser Pulses. *Science* **278**, 661 (1997).
- [10] M. Ferray, A. L’Huillier, X. F. Li, L. A. Lompre, G. Mainfray and C. Manus. Multiple-harmonic conversion of 1064 nm radiation in rare gases. *J. Phys. B: At. Mol. Opt. Phys.* **21** L31 (1988).
- [11] M. Bellini, C. Lyngå, A. Tozzi, M. B. Gaarde, T. W. Hänsch, A. L’Huillier and C.-G. Wahlström. Temporal Coherence of Ultrashort High-Order Harmonic Pulses. *Phys. Rev. Lett.* **81**, 297 (1998).
- [12] P. M. Paul, E. S. Toma, P. Breger, G. Mullot, F. Augé, Ph. Balcou, H. G. Muller and P. Agostini. Observation of a Train of Attosecond Pulses from High Harmonic Generation. *Science* **292**, 1689 (2001).
- [13] M. Hentschel, R. Kienberger, Ch. Spielmann, G. A. Reider, N. Milosevic, T. Brabec, P. Corkum, U. Heinzmann, M. Drescher and F. Krausz. Attosecond metrology. *Nature* **414**, 509–513 (2001).

- [14] M. Schultze, M. Fiess, N. Karpowics, J. Gagnon, M. Korbman, M. Hofstetter, S. Neppl, A. L. Cavalieri, Y. Komninos, Th. Mercouris, C.A Nicolaides, R. Pazourek, S. Nagele, J. Feist, J. Burgdörfer, A. M. Azzeer, R. Ernstorfer, R. Kienberger, U. Kleineberg, E. Goulielmakis, F. Krausz and V. S. Yakovlev. Delay in Photoemission. *Science* **328**, 1658 (2010).
- [15] M. Isinger, R. J. Squibb, D. Busto, S. Zhong, A. Harth, D. Kroon, S. Nandi, C. L. Arnold, M. Miranda, J. M. Dahlström, E. Lindroth, R. Feifel, M. Gisselbrecht and A. L’Huillier. Photoionization in the time and frequency domain. *Science* **358**, 893 (2017).
- [16] A. Scrinzi, M. Yu. Ivanov, R. Kienberger and D. M. Villeneuve. Attosecond physics. *J. Phys. B: At. Mol. Opt. Phys.* **39**, R1 (2006).
- [17] F. Krausz and M. Ivanov. Attosecond physics. *Rev. Mod. Phys.* **81**, 163 (2009).
- [18] F. Frank, C. Arrell, T. Witting, W. A. Okell, J. McKenna, J. S. Robinson, C. A. Haworth, D. Austin, H. Teng, I. A. Walmsley, J. P. Marangos and J. W. G. Tisch. Invited Review Article: Technology for Attosecond Science. *Rev. Sci. Instrum.* **83**, 071101 (2012).
- [19] R. Borrego Varillas, M. Lucchini, M. Nisoli. Attosecond spectroscopy for the investigation of ultrafast dynamics in atomic, molecular and solid-state physics. *Rep. Prog. Phys.* **85**, 066401 (2022).
- [20] K. C. Kulander, K. J. Schafer and J. L. Krause. in *Super-Intense Laser-Atom Physics* **316**, ed. by B. Piraux, A. L’Huillier, K. Rzażewski (Plenum, New York, 1993), p. 95.
- [21] P. B. Corkum. Plasma perspective on strong field multiphoton ionization. *Phys. Rev. Lett.* **71**, 1994 (1993).
- [22] Gy. Farkas and Cs. Toth. Proposal for attosecond light pulse generation using laser induced multiple-harmonic conversion processes in rare gases. *Phys. Lett. A* **168**, 447 (1992).
- [23] S. E. Harris, J. J. Macklin and T. W. Hänsch. Atomic scale temporal structure inherent to high-order harmonic generation. *Opt. Commun.* **100**, 487 (1993).
- [24] A. Baltuška, Th. Udem, M. Uiberacker, M. Hentschel, E. Goulielmakis, Ch. Gohle, R. Holzwarth, V. S. Yakovlev, A. Scrinzi, T. W. Hänsch and F. Krausz Erratum: Attosecond control of electronic processes by intense light fields. *Nature* **422**, 189 (2003).
- [25] W. Klemperer, X.-C. Luo, R. Rosner and D. N. Schramm. On the possibility of coherently stimulated recombination and cosmological structure generation: recombination instability. *Proc. Natl. Acad. Sci. USA* **92**, 6166 (1995).
- [26] Y. Hahn. Electron-Ion Recombination Processes in Plasmas. In: Janev, R.K. (eds) *Atomic and Molecular Processes in Fusion Edge Plasmas*. Springer, Boston, MA (1995).
- [27] Y. Hahn. Electron-ion recombination processes - an overview. *Rep. Prog. Phys.* **60**, 691 (1997).
- [28] R. Neumann, H. Poth, A. Winnacker and A. Wolf. Laser-enhanced electron-ion capture and antihydrogen formation. *Z. Physik. A* **313**, 253 (1983).

- [29] U. Schramm, J. Berger, M. Grieser, D. Habs, E. Jaeschke, G. Kilgus, D. Schwalm, A. Wolf, R. Neumann and R. Schuch. Observation of laser-induced recombination in merged electron and proton beams. *Phys. Rev. Lett.* **67**, 22 (1991).
- [30] U. Schramm, T. Schüssler, D. Habs, D. Schwalm and A. Wolf. Laser-induced recombination studies with the adiabatically expanded electron beam of the Heidelberg TSR. *Hyperfine Interact.* **99**, 309 (1996).
- [31] I. D. Williams, J. McKenna, J. Wood, M. Suresh, W. A. Bryan, S. L. Stebbings, E. M. L. English, C. R. Calvert, B. Srigengan, E. J. Divall, C. J. Hooker, A. J. Langley and W. R. Newell. Excited Ions in Intense Femtosecond Laser Pulses: Laser-Induced Recombination. *Phys. Rev. Lett.* **99**, 173002 (2007).
- [32] E. S. Shuman, R. R. Jones and T. F. Gallagher. Multiphoton Assisted Recombination. *Phys. Rev. Lett.* **101**, 263001 (2008).
- [33] T. Mohamed, G. Andler, M. Fogle, E. Justiniano, S. Madzunkov and R. Schuch. Effects of polarization on laser-induced electron-ion recombination. *Phys. Rev. A* **83**, 032702 (2011).
- [34] M. Y. Kuchiev and V. N. Ostrovsky. Multiphoton radiative recombination of electron assisted by a laser field. *Phys. Rev. A* **61**, 033414 (2000).
- [35] A. Jaroń, J. Z. Kamiński and F. Ehlotzky. Bohr's correspondence principle and x-ray generation by laser-stimulated electron-ion recombination. *Phys. Rev. A* **63**, 055401 (2001).
- [36] A. Jaroń, J. Z. Kamiński and F. Ehlotzky. Coherent Phase-Control in Laser-Assisted Radiative Recombination. *J. Phys. B* **34**, 1221 (2001).
- [37] D. B. Milošević and F. Ehlotzky. Rescattering effects in soft-x-ray generation by laser-assisted electron-ion recombination. *Phys. Rev. A* **65**, 042504 (2002).
- [38] C. Leone, S. Bivona, R. Burlon and G. Ferrante. Strong-field and plasma aspects of multiphoton radiative recombination. *Phys. Rev. A* **66**, 051403(R) (2002).
- [39] T. Cheng, X. Li, S. Ao, L.-A. Wu and P. Fu. Frequency-domain interpretation of the plateaus in laser-assisted recombination and high-order harmonic generation. *Phys. Rev. A* **68**, 033411 (2003).
- [40] J. Z. Kamiński and F. Ehlotzky. Optimized X-ray Generation by Electron-Ion Recombination in the Presence of Powerful Laser Fields. *Opt. Commun.* **234**, 343 (2004).
- [41] S. Bivona, G. Bonanno, R. Burlon and C. Leone. Polarization and angular distribution of the radiation emitted in laser-assisted recombination. *Phys. Rev. A* **76**, 031402(R) (2007).
- [42] A. N. Zheltukhin, A. V. Flegel, M. V. Frolov, N. L. Manakov and A. F. Starace. Resonant phenomena in laser-assisted radiative attachment or recombination. *J. Phys. B* **45**, 081001 (2012).
- [43] S. Odžak and D. B. Milošević. Bicircular-laser-field-assisted electron-ion radiative recombination. *Phys. Rev. A* **92**, 053416 (2015).
- [44] A. Čerkić, M. Busuladžić and D. B. Milošević. Electron-ion radiative recombination assisted by a bichromatic elliptically polarized laser field. *Phys. Rev. A* **95**, 063401 (2017).

- [45] A. Tutmić, A. Čerkić, M. Busuladžić and D. B. Milošević. Role of the relative phase and intensity ratio in electron-ion recombination assisted by a bicircular laser field. *Eur. Phys. J. D* **73**, 231 (2019).
- [46] L. V. Keldysh. Ionization in the Field of a Strong Electromagnetic Wave. *Sov. Phys. JETP* **20**, 1307 (1965).
- [47] F. H. M. Faisal. Multiple absorption of laser photons by atoms. *J. Phys. B: At., Mol. Opt. Phys.* **6**, L89 (1973).
- [48] H. R. Reiss. Effect of an intense electromagnetic field on a weakly bound system. *Phys. Rev. A* **22**, 1786 (1980).
- [49] A. Jaroń, J. Z. Kamiński and F. Ehlotzky. Stimulated radiative recombination and x-ray generation. *Phys. Rev. A* **61**, 023404 (2000).
- [50] R. A. Müller, D. Seipt, S. Fritzsche and A. Surzhykov. Effect of bound-state dressing in laser-assisted radiative recombination. *Phys. Rev. A* **92**, 053426 (2015).
- [51] A. E. Kučukalić, W. Becker, D. B. Milošević. Application of the Phase-Space Path Integral to Strong-Laser-Field-Assisted Electron-Ion Radiative Recombination: A Gauge-Covariant Formulation. *Symmetry* **12**, 1606 (2020).
- [52] G. Shchedrin and A. Volberg. Analytical model for laser-assisted recombination of hydrogenic atoms. *J. Phys. A: Math. Theor.* **44**, 245301 (2011).
- [53] A. N. Zheltukhin, N. L. Manakov, A. V. Flegel and M. V. Frolov. Effects of the atomic structure and interference oscillations in the electron photorecombination spectrum in a strong laser field. *JETP Letters* **94**, 599 (2011).
- [54] L. D. Landau and E. M. Lifshitz, *Quantum Mechanics: Non-Relativistic Theory* (Nauka, Moscow, 1989, 4th ed.; Pergamon Press, Oxford, 1977, 3rd ed.).
- [55] S. Bivona, R. Burlon, G. Ferrante and C. Leone. Controlling laser assisted radiative recombination with few-cycle laser pulses. *Laser Phys. Lett.* **1**, 118 (2004).
- [56] S. X. Hu and L. A. Collins. Intense laser-induced recombination: The inverse above-threshold ionization process. *Phys. Rev. A* **70**, 013407 (2004).
- [57] J. Z. Kamiński and F. Ehlotzky. Time-frequency analysis of x-ray generation by recombination in short laser pulses. *Phys. Rev. A* **71**, 043402 (2005).
- [58] J. Z. Kamiński and F. Ehlotzky. Generation of Attosecond Pulses in Electron-Ion Recombination Processes. *J. Mod. Opt.* **53**, 7 (2006).
- [59] S. Bivona, R. Burlon, G. Ferrante and C. Leone. Radiative recombination in the presence of a few cycle laser pulse. *Opt. Express* **14**, 3715 (2006).
- [60] S. Bivona, R. Burlon and C. Leone. Controlling laser assisted radiative recombination with few-cycle laser pulses. *Laser Phys. Lett.* **4**, 44 (2007).
- [61] A. Čerkić and D. B. Milošević. Few-cycle-laser-pulse-assisted electron-ion radiative recombination. *Phys. Rev. A* **88**, 023414 (2013).

- [62] A. J. Jerri. *The Gibbs Phenomenon in Fourier Analysis Splines and Wavelet Approximations* (Springer, Dordrecht, 1998).
- [63] J. J. Duistermaat and J. A. C. Kolk. *Distributions - Theory and Applications* (Springer, New York, 2010).
- [64] C. Müller, A. B. Voitkiv and B. Najjari. Relativistic electron-ion recombination in the presence of an intense laser field. *J. Phys. B* **42**, 221001 (2009).
- [65] D. M. Wolkow. Über eine Klasse von Lösungen der Diracschen Gleichung. *Z. Phys.* **94**, 250 (1935).
- [66] G. F. Gribakin and M. Yu. Kuchiev. Multiphoton detachment of electrons from negative ions. *Phys. Rev. A* **55**, 3760 (1997).
- [67] M. Boca and V. Florescu. Nonlinear Compton scattering with a laser pulse. *Phys. Rev. A* **80**, 053403 (2009).
- [68] C. Cohen-Tannoudji, B. Diu and F. Laloë. *Quantum Mechanics, Volume 2* (Wiley-VCH, Germany, 2020).
- [69] G. F. Boudreaux-Bartels. *The Transforms and Applications Handbook: Second Edition* ed. by A. D. Poularikas (CRC Press, Boca Raton, 2000).
- [70] F. Cajiao Vélez, Lei Geng, J. Z. Kamiński, Liang-You Peng and K. Krajewska. Vortex streets and honeycomb structures in photodetachment driven by linearly polarized few-cycle laser pulses. *Phys. Rev. A* **102**, 043102 (2020).
- [71] Lei Geng, F. Cajiao Vélez, J. Z. Kamiński, Liang-You Peng and K. Krajewska. Vortex structures in photodetachment by few-cycle circularly polarized pulses. *Phys. Rev. A* **102**, 043117 (2020).
- [72] K. Krajewska and J. Z. Kamiński. Compton-based coherent comb structures in radiation and matter domains. *Laser Phys. Lett.* **11**, 035301 (2014).
- [73] K. Krajewska, M. Twardy and J. Z. Kamiński. Global phase and frequency comb structures in nonlinear Compton and Thomson scattering. *Phys. Rev. A* **89**, 052123 (2014).
- [74] R. Kanya, Y. Morimoto and K. Yamanouchi. Observation of Laser-Assisted Electron-Atom Scattering in Femtosecond Intense Laser Fields. *Phys. Rev. Lett.* **105**, 123202 (2010).
- [75] Y. Morimoto, R. Kanya and K. Yamanouchi. Laser-assisted electron diffraction for femtosecond molecular imaging. *J. Chem. Phys.* **140**, 064201 (2014).
- [76] R. Kanya and K. Yamanouchi. Femtosecond Laser-Assisted Electron Scattering for Ultrafast Dynamics of Atoms and Molecules. *Atoms* **7**, 85 (2019).
- [77] H. Buchholz. in *The Confluent Hypergeometric Function* **15** (Springer, Berlin Heidelberg, 1969).
- [78] <https://mathworld.wolfram.com/BetaFunction.html>

- [79] D. Kanti, J. Z. Kamiński, L.Y. Peng and K. Krajewska. Laser-assisted electron-atom radiative recombination in short laser pulses. *Phys. Rev. A* **104**, 033112 (2021).
- [80] O. Brinzaescu, J. Eichler, A. Ichihara, T. Shirai. and Th. Stöhlker. Comparison Between the Nonrelativistic Dipole Approximation and the Exact Relativistic Theory for Radiative Recombination. *Phys. Scr.* **1999**, 324 (1998).
- [81] M. Førre, S. Selstø, J. P. Hansen and L. B. Madsen. Exact Nondipole Kramers-Henneberger Form of the Light-Atom Hamiltonian: An Application to Atomic Stabilization and Photoelectron Energy Spectra. *Phys. Rev. Lett.* **95**, 043601 (2005).
- [82] M. Førre, J. P. Hansen, L. Kocbach, S. Selstø and L. B. Madsen. Nondipole Ionization Dynamics of Atoms in Superintense High-Frequency Attosecond Pulses. *Phys. Rev. Lett.* **97**, 043601 (2006).
- [83] M. Førre and A. S. Simonsen. Nondipole ionization dynamics in atoms induced by intense xuv laser fields. *Phys. Rev. A* **90**, 053411 (2014).
- [84] A. S. Simonsen and M. Førre. Magnetic-field-induced enhancement of atomic stabilization in intense high-frequency laser fields. *Phys. Rev. A* **92**, 013405 (2015).
- [85] K. Krajewska and J. Z. Kaminski. Radiation pressure in strong-field-approximation theory: Retardation and recoil corrections. *Phys. Rev. A* **92**, 043419 (2015).
- [86] M. Førre and A. S. Simonsen. Generalized velocity-gauge form of the light-matter interaction Hamiltonian beyond the dipole approximation. *Phys. Rev. A* **93**, 013423 (2016).
- [87] T. K. Lindblom, M. Førre, E. Lindroth and S. Selstø. Semirelativistic Schrödinger Equation for Relativistic Laser-Matter Interactions. *Phys. Rev. Lett.* **121**, 253202 (2018).
- [88] S. Brennecke and M. Lein. High-order above-threshold ionization beyond the electric dipole approximation. *J. Phys. B* **51**, 094005 (2018).
- [89] N. Haram, I. Ivanov, H. Xu, K. T. Kim, A. Atia-tul-Noor, U. Satya Sainadh, R. D. Glover, D. Chetty, I. V. Litvinyuk and R. T. Sang. Relativistic Nondipole Effects in Strong-Field Atomic Ionization at Moderate Intensities. *Phys. Rev. Lett.* **123**, 093201 (2019).
- [90] M. X. Wang et al. Review on non-dipole effects in ionization and harmonic generation of atoms and molecules. *Chinese Phys. B* **29**, 013302 (2020).
- [91] A. Hartung, S. Brennecke, K. Lin, D. Trabert, K. Fehre, J. Rist, M. S. Schöffler, T. Jahnke, L. Ph. H. Schmidt, M. Kunitski, M. Lein, R. Dörner and S. Eckart. Electric Nondipole Effect in Strong-Field Ionization. *Phys. Rev. Lett.* **126**, 053202 (2021).
- [92] M. Førre. Nondipole effects and photoelectron momentum shifts in strong-field ionization by infrared light. *Phys. Rev. A* **106**, 013104 (2022).
- [93] L. B. Madsen. Nondipole effects in tunneling ionization by intense. *Phys. Rev. A* **105**, 043107 (2022).
- [94] M. C. Suster, J. Derlikiewicz, K. Krajewska, F. Cajiao Vélez, and J. Z. Kamiński. Nondipole signatures in ionization and high-order harmonic generation. *Phys. Rev. A* **107**, 053112 (2023).

- [95] M. C. Suster, J. Derlikiewicz, J. Z. Kamiński and K. Krajewska. Photoelectron jets and interference structures in ionization beyond dipole approximation: carrier-envelope phase effects and vortex streets. *Opt. Express* **32**, 6085 (2024).
- [96] H. R. Reiss. Limits on Tunneling Theories of Strong-Field Ionization. *Phys. Rev. Lett.* **101**, 043002 (2008).
- [97] H. R. Reiss. The tunnelling model of laser-induced ionization and its failure at low frequencies. *J. Phys. B* **47**, 204006 (2014).
- [98] C. T. L. Smeenk, L. Arissian, B. Zhou, A. Mysyrowicz, D. M. Villeneuve, A. Staudte, and P. B. Corkum. Partitioning of the Linear Photon Momentum in Multiphoton Ionization. *Phys. Rev. Lett.* **106**, 193002 (2011).
- [99] A. Ludwig, J. Maurer, B. W. Mayer, C. R. Phillips, L. Gallmann, and U. Keller. Breakdown of the Dipole Approximation in Strong-Field Ionization. *Phys. Rev. Lett.* **113**, 243001 (2014).
- [100] S. V. B. Jensen and L. B. Madsen. Nondipole effects in laser-assisted electron scattering. *J. Phys. B: At. Mol. Opt. Phys.* **53**, 195602 (2020).
- [101] D. Kanti, M. M. Majczak, J. Z. Kamiński, Liang-You Peng, K. Krajewska. Laser-assisted radiative recombination beyond the dipole approximation. *Phys. Rev. A* **110**, 043112 (2024).
- [102] E. Neyra, F. Videla, J. Pérez-Hernández, et al. High-order harmonic generation driven by chirped laser pulses induced by linear and non linear phenomena. *Eur. Phys. J. D* **70**, 243 (2016).
- [103] H. Yuan, F. Li and H. Long. Control of high-order harmonic generation with chirped inhomogeneous fields. *J. Opt. Soc. Am. B* **34**, 2390 (2017).
- [104] F. H. M. Faisal. Strong-field S-matrix theory with final-state Coulomb interaction in all orders. *Phys. Rev. A* **94**, 031401 (2016).
- [105] A. Nordsieck. Reduction of an Integral in the Theory of Bremsstrahlung. *Phys. Rev.* **93**, 785 (1954).
- [106] J. J. Sakurai and J. J. Napolitano. *Modern Quantum Mechanics*. (Hardcover, 2nd ed., Pearson, 2010).
- [107] I. Bialynicki-Birula, M. Cieplak and J. Kamiński. *Theory of Quanta* (Oxford University, 1992).
- [108] N. Lebedev and R. A. Silverman. *Special Functions and Their Applications* (Dover Publications, 1972).
- [109] S. Malinovskaya. Chirped pulse control methods for imaging of biological structure and dynamics. *Int. J. Quantum Chem.* **107**, 3151 (2007).
- [110] B. J. Galow, Y. I. Salamin, T. V. Liseykina, Z. Harman, and C. H. Keitel. Dense monoenergetic proton beams from chirped laser-plasma interaction. *Phys. Rev. Lett.* **10718**, 185002 (2011).

- [111] K. Hartig, J. McNutt, P. Ko, T. Jacomb-Hood, R. Schur, and I. Jovanovic. *Chirped-Pulse Femtosecond Laser-Induced Breakdown Spectroscopy for Nuclear Forensics* (Optica Publishing Group, 2012).
- [112] G. Mourou, T. Tajima, and S. V. Bulanov. Optics in the relativistic regime. *Reviews of Modern Physics* **78**, 309 (2006).
- [113] J. M. Ngoko Djiokap, S. X. Hu, L. B. Madsen, N. L. Manakov, A. V. Meremianin, and A. F. Starace. Electron Vortices in Photoionization by Circularly Polarized Attosecond Pulses. *Phys. Rev. Lett.* **115**, 113004 (2015).
- [114] J. M. Ngoko Djiokap, A. V. Meremianin, N. L. Manakov, S. X. Hu, L. B. Madsen, and A. F. Starace. Multistart Spiral Electron Vortices in Ionization by Circularly Polarized UV Pulses. *Phys. Rev. A* **94**, 013408 (2016).
- [115] J. M. Ngoko Djiokap, A. V. Meremianin, N. L. Manakov, S. X. Hu, L. B. Madsen, and A. F. Starace. Kinematical Vortices in Double Photoionization of Helium by Attosecond Pulses. *Phys. Rev. A* **96**, 013405 (2017).
- [116] D. Pengel, S. Kerbstadt, D. Johannmeyer, L. Englert, T. Bayer, and M. Wollenhaupt. Electron Vortices in Femtosecond Multiphoton Ionization. *Phys. Rev. Lett.* **118**, 053003 (2017).
- [117] S. Kerbstadt, K. Eickhoff, T. Bayer, and M. Wollenhaupt. Odd Electron Wave Packets from Cycloidal Ultrashort Laser Fields. *Nat. Commun.* **10**, 658 (2019).
- [118] S. Kerbstadt, K. Eickhoff, T. Bayer, and M. Wollenhaupt. Control of Free Electron Wave Packets by Polarization-Tailored Ultrashort Bichromatic Laser Fields. *Adv. Phys.: X* **4**, 1672583 (2019).
- [119] A. S. Maxwell, G. S. J. Armstrong, M. F. Ciappina, E. Pisanty, Y. Kang, A. C. Brown, M. Lewenstein, and C. Figueira de Morisson Faria. Manipulating Twisted Electrons in Strong-Field Ionization. *Faraday Discuss.* **228**, 394 (2021).
- [120] K. Eickhoff, D. Köhnke, L. Feld, L. Englert, T. Bayer, and M. Wollenhaupt. Tailored Holograms for Superimposed Vortex States. *New J. Phys.* **22**, 123015 (2020).
- [121] K. Eickhoff, C. Rathje, D. Köhnke, S. Kerbstadt, L. Englert, T. Bayer, S. Schäfer, and M. Wollenhaupt. Orbital Angular Momentum Superposition States in Transmission Electron Microscopy and Bichromatic Multiphoton Ionization. *New J. Phys.* **22**, 103045 (2020).
- [122] Y. Kang, E. Pisanty, M. Ciappina, M. Lewenstein, C. Figueira de Morisson Faria, and A. S. Maxwell. Conservation Laws for Electron Vortices in Strong-Field Ionisation. *Eur. Phys. J. D* **75**, 199 (2021).
- [123] T. Bayer and M. Wollenhaupt. Molecular Free Electron Vortices in Photoionization by Polarization-Tailored Ultrashort Laser Pulses. *Front. Chem.* **10**, 899461 (2022).
- [124] P. A. M. Dirac. Quantised Singularities in the Electromagnetic Field. *Proc. R. Soc. A* **133**, 60 (1931).
- [125] W. F. Viven. The detection of single quanta of circulation in liquid helium II. *Proc. R. Soc. London Ser. A* **260**, 218 (1961).

-
- [126] F. Cajiao Vélez, J. Z. Kamiński, and K. Krajewska. Generation of Propagating Electron Vortex States in Photodetachment of H^- . *Phys. Rev. A* **101**, 053430 (2020).
- [127] F. Cajiao Vélez, L. Geng, J. Z. Kamiński, L.-Y. Peng, and K. Krajewska. Vortex Streets and Honeycomb Structures in Photodetachment Driven by Linearly Polarized Few-Cycle Laser Pulses. *Phys. Rev. A* **102**, 043102 (2020).
- [128] L. Geng, F. Cajiao Vélez, J. Z. Kamiński, L.-Y. Peng, and K. Krajewska. Vortex Structures in Photodetachment by Few-Cycle Circularly Polarized Pulses. *Phys. Rev. A* **102**, 043117 (2020).
- [129] F. Cajiao Vélez. Generation of Quantum Vortices in Photodetachment: The Role of the Ground-State Wave Function. *Phys. Rev. A* **104**, 043116 (2021).
- [130] L. Geng, F. Cajiao Vélez, J. Z. Kamiński, L.-Y. Peng, and K. Krajewska. Structured Photoelectron Distributions in Photodetachment Induced by Trains of Laser Pulses: Vortices versus Spirals. *Phys. Rev. A* **104**, 033111 (2021).
- [131] S. Selstø and M. Førre, Alternative descriptions of the light-matter interaction beyond the dipole approximation. *Phys. Rev. A* **76**, 023427 (2007).